

MAGNETIC ORDERING AND SPIN WAVE DYNAMICS IN TRANSITION METAL
ARSENIDES

Draft of December 3, 2020 at 02:20

BY

MANOHAR H. KARIGERASI

DISSERTATION

Submitted in partial fulfillment of the requirements
for the degree of Doctor of Philosophy in Materials Science and Engineering
in the Graduate College of the
University of Illinois at Urbana-Champaign, 2021

Urbana, Illinois

Doctoral Committee:

Associate Professor Daniel P. Shoemaker, Chair
Professor David G. Cahill
Professor Jian-Min Zuo
Research Assistant Professor Gregory MacDougall

Abstract

Metallic antiferromagnets have gained interest in recent times due to the possibility of being useful as a memory device. Arsenic forms a large pool of magnetic metals in combination with other transition metals that have largely been ignored so far. In this report, we discover a new ternary metallic arsenide in the Cu-Mn-As phase space, identify its chemical and magnetic structure, and characterize its electrical and magnetic properties. We also carry out the magnetic structure refinement of Mn_3As_2 from neutron powder diffraction data at different temperatures to understand the magnetic ordering in Mn-As compounds. Using inelastic neutron scattering measurements, we determine exchange interactions in Fe_2As , which has the same structure as CuMnAs, showing a highly 2D magnon character although the phonons are 3D. Finally, we report a magnetic-structural coupled transition across 300 K in tetragonal CuMnAs and determine the correct magnetic structure of the compound.

Acknowledgments

This project would not be possible without many people. Firstly, thanks to my advisor, Prof. Daniel P. Shoemaker.

Table of Contents

List of Tables	v
List of Figures	vi
Chapter 1 Introduction	1
1.1 Magnetic information storage	1
1.2 Antiferromagnets for potential applications as a memory unit	2
1.3 Exploration of Cu-Mn-As phase space	2
1.4 Exchange interactions in Cu ₂ Sb type structures	5
Chapter 2 Theory of electrical switching in metallic antiferromagnets	6
2.1 Hidden spin polarization in centrosymmetric crystals	6
2.2 Finding metallic antiferromagnetic candidates with R2-D2 effect	7
2.3 Components of torque from non-equilibrium CISP	9
2.4 Spin polarization in CuMnAs, Mn ₂ Au and Fe ₂ As	11
2.5 Conclusions	12
2.6 Acknowledgements	15
Chapter 3 Materials synthesis and characterization	16
3.1 Bulk materials synthesis	16
3.1.1 Sensitivity of Fe:As stoichiometry in the synthesis of Fe ₂ As	16
3.2 Synthesis of compounds in the Cu-Mn-As system	18
3.3 Materials characterization	19
3.3.1 X-ray diffraction measurements	19
3.3.2 SEM/EDS measurements	20
3.3.3 Calorimetry measurements	20
3.3.4 SQUID magnetometry measurements	21
3.3.5 Magnetotransport measurements	22
3.4 Neutron scattering	22
3.4.1 Neutron powder diffraction	22
3.4.2 Inelastic neutron scattering	22

Chapter 4 Magnetic structure refinement from neutron diffraction measurements . . .	23
Chapter 5 An in-plane hexagonal antiferromagnet in the Cu-Mn-As system, Cu_{0.82}Mn_{1.18}As	29
5.1 Introduction	29
5.2 Methods	31
5.3 Results and Discussion	32
5.3.1 Structure refinement	32
5.3.2 Magnetic ordering	35
5.3.3 First-principles simulations	40
5.4 Conclusions	43
5.5 Acknowledgments	43
Chapter 6 Two step magnetic ordering in monoclinic Mn₃As₂	44
Chapter 7 Spin canting in tetragonal CuMnAs	54
Chapter 8 Exchange interactions in Fe₂As probed by inelastic neutron scattering . .	56
Chapter 9 Conclusions	65
References	67

List of Tables

2.1	Different cases of spin polarization depending on the symmetry of atomic sites and the unit cell [26].	7
2.2	List of metallic antiferromagnetic candidates filtered out from MPDS and ASM database and their metal atom site symmetries	9
2.3	Summary of the linear response tensor components for the CISP observable and electric field	11
2.4	Linear response tensor in CuMnAs and Mn ₂ Au assuming Mn moment to be 1 μ_B	13
2.5	Linear response tensor in Fe ₂ As when Fe moments have been set to 0 μ_B	14
5.1	Structural parameters obtained from room-temperature Mo- $K\alpha$ X-ray single-crystal refinement (full-matrix least-squares on F^2) with occupancies fixed from synchrotron X-ray and neutron co-refinement.	34
5.2	Atomic parameters obtained from room-temperature X-ray single-crystal refinement of Cu _{0.82} Mn _{1.18} As. Occupancy values for Cu/Mn sites are co-refined to 100 K synchrotron and 400 K neutron powder diffraction data (see Fig. 5.3). Atomic displacement parameters U_{ij} are given in units of Å ²	35
5.3	Energy differences (meV/atom) between different constraints in DFT (see text), and lattice parameters (Å, degree) from all-relaxed calculations of stoichiometric hexagonal CuMnAs and Cu _{0.89} Mn _{1.11} As. All phases have $\gamma = 120^\circ$	41

List of Figures

1.1	The magnetic structures of tetragonal CuMnAs and MnF ₂ are shown in (a) and (b), respectively.	3
1.2	Magnetic structure of orthorhombic CuMnAs	3
1.3	Cu-Mn-As ternary phase diagram highlighting some of the known ternary compounds in blue and known magnetic structures in red. Not all compounds in this system are shown here.	4
2.1	The schematic of the Fermi surface of the local sectors near Mn1 and Mn2 atoms are shown in (a) and (b), respectively. The magnetic structure of tetragonal CuMnAs is shown in (c) which also includes the highlighted local sectors.	7
2.2	Magnetic structure of Fe ₂ As along with the Fe site numbers corresponding to Table 2.5.	12
3.1	The process of making bulk materials using traditional solid state synthesis technique is shown here. The powders mixed inside the glovebox in (a) are transferred to a quartz tube and vacuum sealed in (b). The vacuum sealed ampoule in (c) is placed inside the box furnace in (d) and subjected to a heating profile. (e) shows the final ingot obtained in case of CuMnAs sample.	17
3.2	Impurity percentage as a function of Fe:As starting stoichiometry ratio with 200 mesh size Fe powders for making Fe ₂ As samples.	17
3.3	Synchrotron x-ray diffraction data of Fe ₂ As for different ratios of Fe:As from 10 μm Fe powders is shown in (a) and the corresponding impurity percentage is shown in (b).	18
3.4	The flat-bottom bulk of the quartz ampoules is shown in (a) and (b) shows the final powder-containing vacuum sealed ampoules.	21
4.1	Electronic band structure	24
4.2	Electronic band structure	24
4.3	Electronic band structure	25
4.4	Electronic band structure	25
4.5	Electronic band structure	26
4.6	Electronic band structure	27
4.7	Electronic band structure	27

5.1	(Color online.) Hexagonal Cu _{0.82} Mn _{1.18} As has been marked with a star among the previously-known phases in the Cu–Mn–As system. Compositions near CuMnAs are known to crystallize in both tetragonal and orthorhombic crystal systems.	30
5.2	(Color online.) Unit cell of Cu _{0.82} Mn _{1.18} As (a) is shown with square pyramidal Mn in purple, tetrahedrally coordinated Cu in blue, and As in green. In (b), the refined magnetic structure is shown with moments on the Mn sites.	32
5.3	(Color online.) Refinements of Cu _{0.82} Mn _{1.18} As to (a) synchrotron X-ray powder diffraction at 100 K at APS 11-BM ($\lambda = 0.4128 \text{ \AA}$) and (b) neutron powder diffraction at 400 K on WAND ² ($\lambda = 1.487 \text{ \AA}$).	33
5.4	(Color online.) DSC data (a) show a clear kink in the heat flow at $T_N \approx 270 \text{ K}$, indicating a discontinuous change in heat capacity of the sample. Data on heating are reflected about the x -axis. The same transition appears in magnetic susceptibility measurements (b) of an aligned single crystal, with the field axis along the [001] and [100] directions.	37
5.5	(Color online.) Measured single-crystal neutron diffraction intensity (a) of the (020) peak of Cu _{0.82} Mn _{1.18} As shows a gradual increase upon cooling past T_N down to 4 K. The (020) peak is an allowed nuclear reflection and persists with constant intensity (~ 50) above T_N . The differences between observed and refined structure factors F_{hkl}^2 at $T = 4 \text{ K}$ are shown in (b). The triangular model obtained from neutron refinement are shown as (+) and the DFT-derived model as (x).	38
5.6	(Color online.) (a) Resistivity of Cu _{0.82} Mn _{1.18} As with applied field H along [100] and current I along [001]. The resistivity is relatively flat across the temperature range, with a small kink at $T_N = 270 \text{ K}$. Hall measurements of the sample with H along [100] and current along [001] show a decreasing trend followed by an increase at higher temperatures.	39
5.7	(Color online.) Structure and magnetic configuration from DFT for (a) stoichiometric hexagonal CuMnAs and (b) Cu _{0.89} Mn _{1.11} As. Mn is shown in purple, Cu in blue, and As in green.	40
5.8	(Color online.) Electronic band structure of (a) stoichiometric hexagonal CuMnAs (blue) and (b) Cu _{0.89} Mn _{1.11} As (red). Both densities of states (DOS, in units of states per \AA^3 and per eV per spin), computed using DFT, are shown in (c). The highest-occupied energies are set as $E = 0 \text{ eV}$	42
6.1	Electronic band structure	45
6.2	Electronic band structure	46
6.3	Electronic band structure	47
6.4	Electronic band structure	48
6.5	Electronic band structure	49
6.6	Electronic band structure	50
6.7	Electronic band structure	51
6.8	Electronic band structure	52
6.9	Electronic band structure	53
8.1	Electronic band structure	57
8.2	Electronic band structure	57

8.3	Electronic band structure	58
8.4	Electronic band structure	59
8.5	Electronic band structure	60
8.6	Electronic band structure	60
8.7	Electronic band structure	61
8.8	Electronic band structure	61
8.9	Electronic band structure	62
8.10	Electronic band structure	62
8.11	Electronic band structure	63
8.12	Electronic band structure	63

Chapter 1

Introduction

1.1 Magnetic information storage

2 In information memory storage devices, there is typically a trade-off between the optimum
3 speed or response time and the complexity and size of memory storage [1]. Volatile memory
4 refers to temporary memory storage where the data is lost when the power is removed.
5 Volatile memory such as SRAM (static random access memory) and DRAM (dynamic random
6 access memory) are used as CPU caches and main memory respectively. SRAM has much
7 faster access times and does not require periodic refreshing. However, it requires four to six
8 transistors per bit as compared to one transistor and one capacitor in DRAM devices [2]. Non-
9 volatile memory (NVM) storage devices on the other hand, retain their data for a long period
10 of time until perturbed. Modern computers mostly use flash memory based solid state drives
11 (SSD) and magnetic hard disk drives (HDD) for storing large amounts of data permanently [2].
12 The first HDD was invented in 1956 by IBM and since then, has seen more than eight orders of
13 magnitude improvement in the storage density. However, the trilemma in magnetic recording
14 between poor thermal stability, coercive fields and signal-to-noise ratio has resulted in the
15 HDD reaching a saturation limit in their device performance [3]. Flash memory uses floating
16 gate MOSFETs (metal oxide semiconductor field effect transistors) to store memory and does
17 not contain any moving parts. Although SSD have dominated the NVM marketshare last few
18 years, there is an increasing need for alternative NVM technologies that are fast, low power
19 consuming and have high storage density [2].

20 One such emerging NVM is MRAM (magnetoresistive random access memory). Unlike
21 flash memory which uses electronic charge as a medium of memory storage, MRAM uses the
22 electronic spin degree of freedom to store information. Unlike charge based storage devices,
23 MRAM is stable against perturbations such as ionizing radiation [4]. MRAM devices consist
24 of cells with magnetic tunnel junctions (MTJ) that have two ferromagnet (FM) layers separated
25 by an insulating layer. One of the layer is pinned where the magnetization orientation is fixed
26 and acts as a reference layer. Depending on the orientation of the free layer, the tunneling
27 magnetoresistance (TMR) is high or low and hence, memory can be read out using electrical
28 currents [3]. Early MRAMs were written by induced fields from heavy currents passed on
29 the adjacent layer. With recent developments in spin transfer torque (STT) in ferromagnets,

30 it has become possible to write using electrical currents [5]. This has reduced the power
31 consumption significantly and made commercialization of MRAM devices possible [3,6].

32 **1.2 Antiferromagnets for potential applications as a memory unit**

33 Historically, antiferromagnets (AFM) have been used as inactive components in MTJ, primarily
34 in exchange biasing the pinned FM layer. However in 2010, Gomonay *et al.* [7] proposed
35 electrical switching of AFMs using STT by passing a spin polarized current injected from
36 a fixed FM layer through the AFM layer. The electrical current gets spin polarized in the
37 FM layer and transfers its angular momentum to the AFM moments to switch it from one
38 orientation to another. There are advantages to using AFM over FM in MRAM devices. AFM
39 are not easily affected by external magnetic fields and do not produce stray fields of their
40 own. They have smaller domains which would allow for higher storage densities [4]. Since
41 the precession frequency of AFM moments is determined by the geometric mean of exchange
42 and anisotropy energies, the dynamics in AFM materials occur at THz timescales which is
43 two orders of magnitude higher than in FM [8]. Although the AFM can be switched using
44 electrical currents from parallel to perpendicular orientation with respect to the FM mag-
45 netization direction, the reverse process cannot be obtained using electrical current. High
46 magnetic fields above the spin flop transition of the AFM needs to be applied in order to
47 switch back the AFM to its original state [7].

48 Unlike previously discussed STT MRAM devices, spin orbit torque based electrical switch-
49 ing in broken inversion symmetry FM does not require the presence of a FM polarizer [9].
50 This concept of the presence of relativistic fields is applicable to AFM as well provided the
51 local moments do not sit on centrosymmetric sites. If the two sublattices are related to each
52 other by a center of inversion, then the current induced spin polarized fields are staggered
53 across the two sublattices [4,10,11]. This results in a uniform fieldlike torque experienced by
54 the order parameter. This is possible in bulk materials that are globally centrosymmetric but
55 locally non-centrosymmetric and the two sublattices are related to each other by a center of
56 inversion. It was initially demonstrated in the case of epitaxially grown tetragonal CuMnAs
57 thin films on GaP substrate [4] and since then, it has also been shown in Mn₂Au and CuMnAs
58 sputtered films as well [12,13]. Observation of electrical switching behavior in AFM requires
59 the presence of degenerate Néel vectors like in CuMnAs as shown in Fig. 1.1(a) as opposed to
60 compounds like MnF₂ where the Mn moments point along *c* in Fig. 1.1(b).

61 **1.3 Exploration of Cu-Mn-As phase space**

62 Compounds in Cu-Mn-As phase space have attracted a lot of attention in recent times mainly
63 due to the exotic properties of tetragonal and orthorhombic CuMnAs. As mentioned earlier,

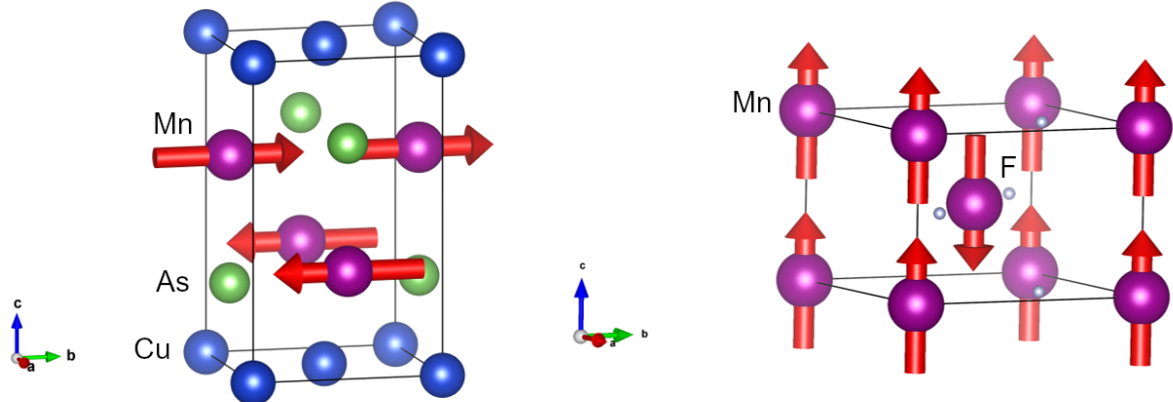


Figure 1.1: The magnetic structures of tetragonal CuMnAs and MnF₂ are shown in (a) and (b), respectively.

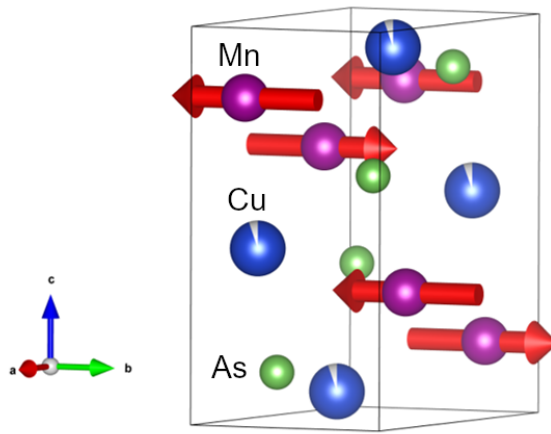


Figure 1.2: Magnetic structure of orthorhombic CuMnAs

tetragonal CuMnAs was the first antiferromagnet where electrical switching was supposedly demonstrated. Orthorhombic CuMnAs, shown in Fig. 1.2, was the first magnetic compound to be proposed as a Dirac semimetal. It is a special compound where the inversion and time reversal symmetry of the magnetic structure is broken but their combined symmetry (*PT* symmetry) is still preserved. Based on the orientation of the AFM order parameter, the compound changes from a conducting to an insulating phase. Hence, there are voltage based switching applications that have been proposed for this compound [14].

Despite the growing importance of the compounds in Cu-Mn-As system, the Cu-Mn-As ternary phase space has not been explored properly. There are four known ternary compounds including both the polymorphs of CuMnAs, orthorhombic CuMn₃As₂ and Cu₂Mn₄As₃ as shown in Fig. 1.3 [15–18]. Bulk orthorhombic CuMnAs can be grown us-

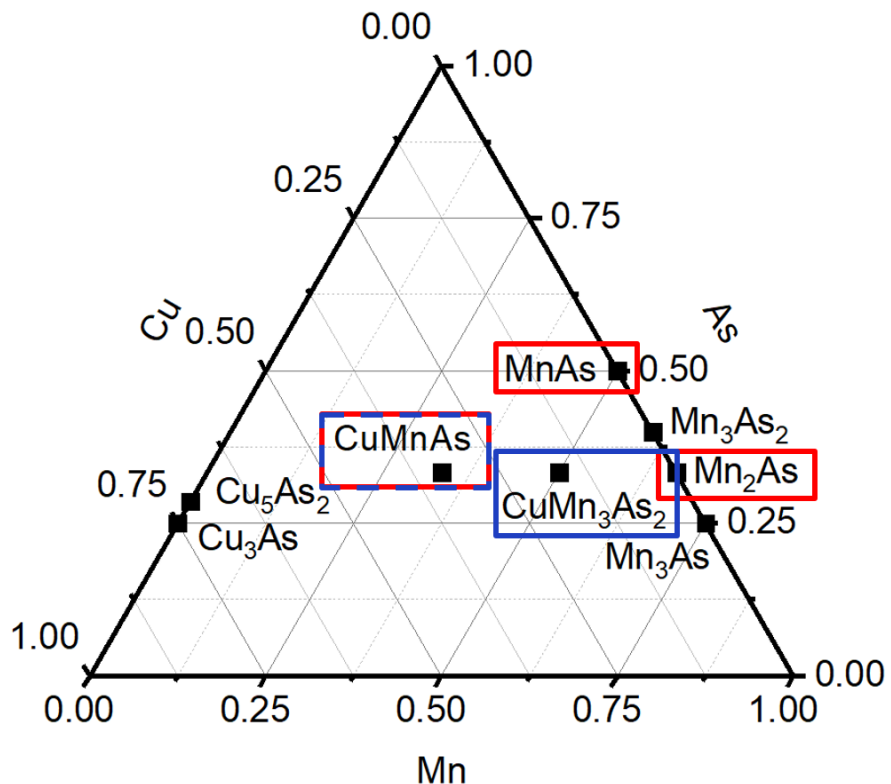


Figure 1.3: Cu-Mn-As ternary phase diagram highlighting some of the known ternary compounds in blue and known magnetic structures in red. Not all compounds in this system are shown here.

75 ing traditional solid state synthesis routes by Cu, Mn and As powders in stoichiometric ratio
76 and heating the powders to 1000°C. In order to synthesize pure bulk tetragonal CuMnAs,
77 we have to go off-stoichiometry and either substitute Mn with Cu or As [18]. Hence, it is
78 important to explore different regions in the Cu-Mn-As system and verify the stability of
79 different ternary compounds. The magnetic structures in the Cu-Mn-As system have also
80 not been identified for most of the compounds. Apart from the four Cu-Mn-As ternary
81 compounds, there are more than ten Mn-As binary compounds present in this system. The
82 magnetic structures are known only for the two previously mentioned CuMnAs compounds,
83 Mn₂As and MnAs as shown in Fig. 1.3 [16,17,19–22]. Since most, if not all, the binary Mn-As
84 compounds are metallic, there is a need to magnetically characterize the compounds and
85 identify their magnetic structures.

86 1.4 Exchange interactions in Cu₂Sb type structures

87 If we want to understand the electrical switching behavior in metallic antiferromagnets, we
88 should be able to quantify the fundamental energies such as magnetocrystalline anisotropy
89 and exchange interactions in materials like CuMnAs. CuMnAs has a Cu₂Sb structure type.
90 Other materials with this structure includes Mn₂As, Cr₂As, Fe₂As, CrMnAs, MnFeAs etc.
91 [23–25]. Although Mn₂As, Cr₂As and Fe₂As have the same structure, the magnetic ground
92 state is different in all three compounds. The strength and sign of direct exchange interactions
93 between two magnetic atoms is a result of the nature of orbital overlap between the two
94 magnetic atoms [24]. Since these materials are metallic, there are two contributions to indirect
95 exchange interactions. One contribution arises from superexchange interactions mediated by
96 As atoms and the other contribution comes from RKKY (Ruderman–Kittel–Kasuya–Yosida)
97 interactions [25]. It is important that we are able to determine what spin interactions are
98 relevant and how does it affect the magnetic ordering in these materials. It is also crucial that
99 we are able to verify the computational methods and the exchange coupling values obtained
100 from these methods so that we can use these methods for other systems as well.

Chapter 2

Theory of electrical switching in metallic antiferromagnets

101 Electrical switching in any magnetic compound is a series of events involving current induced
102 spin polarization (CISP) of charge carriers and different components of CISP exerting differ-
103 ent torque on the magnetic moments of the atoms. The nature of CISP is set by the crystal
104 symmetry. In previous studies of CuMnAs and Mn₂Au, it was stated that the compound
105 should globally centrosymmetric but locally non-centrosymmetric and the two sublattices
106 should be related to each other by a center of inversion [4,10,11]. Is this a necessary condition
107 for observing a staggered spin polarization configuration and can it be applied to general
108 cases? These are some of the questions we will answer in this chapter. Once we have deter-
109 mined the required symmetry criteria, we will filter out metallic antiferromagnetic candidates
110 from large databases of materials such as MPDS (Materials Platform for Data Science) and
111 ASM (ASM International), and analyze the effect of CISP on the torque experienced by the
112 order parameter.

113 2.1 Hidden spin polarization in centrosymmetric crystals

114 It has been known for quite some time that in materials (even non-magnetic) having large
115 spin orbit coupling (SOC) and lacking a center of inversion, magnetic fields are induced.
116 When materials possess structural inversion asymmetry such as in quantum wells and other
117 heterostructures, this effect is called the Rashba effect and it results in a helical type spin
118 texture. When this occurs in materials that lack bulk inversion symmetry, the effect is called
119 the Dresselhaus effect and it results in a unique spin texture [26]. Zhang *et al.* [26] argued that
120 since SOC is a relativistic effect, instead of considering the symmetry of the entire unit cell,
121 one should check for atomic site symmetry to understand SOC induced spin polarization.
122 Based on this argument, there are four cases possible as shown in Table 2.1.

123 R1 and D1 effects refer to conventional Rashba and Dresselhaus spin polarization respec-
124 tively. In materials that are globally centrosymmetric, hidden spin polarization is possible.
125 There is local spin polarization near non-centrosymmetric sites but when summed over the
126 entire unit cell, the net spin polarization is zero. This effect is called the R2 or D2 effect
127 corresponding to Rashba or Dresselhaus effect, respectively in centrosymmetric crystals. The
128 total spin polarization of the unit cell is the vector sum of all the local spin polarizations

Table 2.1: Different cases of spin polarization depending on the symmetry of atomic sites and the unit cell [26].

	All non-polar point groups	At least one polar point groups	All centrosymmetric point groups
Non-Centrosymmetric space group	D1 effect	R1/D1 effect	Not possible
Centrosymmetric space group	D2 effect	R2/D2 effect	No spin polarization

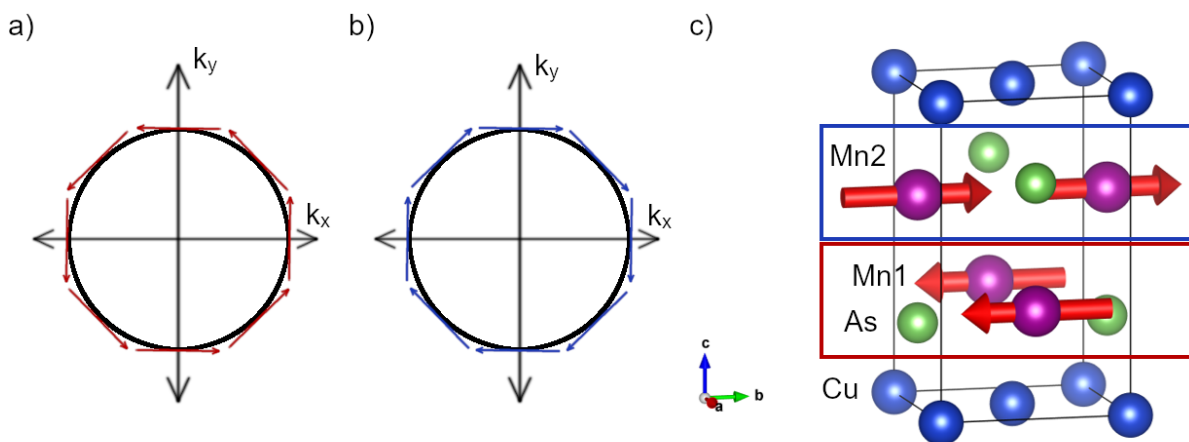


Figure 2.1: The schematic of the Fermi surface of the local sectors near Mn1 and Mn2 atoms are shown in (a) and (b), respectively. The magnetic structure of tetragonal CuMnAs is shown in (c) which also includes the highlighted local sectors.

129 in the unit cell. Non-centrosymmetric point groups can be further divided into polar and
 130 non-polar groups. Local Rashba effect requires the presence of polar point groups on atomic
 131 sites and the local Dresselhaus effect requires the presence of non-polar point groups at the
 132 atom sites. The presence of local spin polarization in centrosymmetric crystals opens the
 133 avenue for studying spin polarization in a larger group of compounds including metallic
 134 antiferromagnets.

135 **2.2 Finding metallic antiferromagnetic candidates with R2-D2
 136 effect**

137 In spin orbit torque based switching of metallic antiferromagnets, the same arguments apply
 138 as before except that we only care about the point group symmetry at the magnetic atom
 139 sites. For example, the magnetic structure of CuMnAs is shown in Fig. 2.1(c). Cu and As

140 atoms have no moments and sit on D_{2d} and C_{4v} sites, respectively. Since only the Mn atoms
141 have moments, we must take the site symmetry of Mn atoms into consideration. Mn atom
142 sites have C_{4v} point group symmetry which is polar. As seen in Fig. 2.1(a,b), the schematic
143 of the Fermi surface corresponding to the Mn layer has a Rashba-like spin texture. When
144 the current is applied, through inverse spin galvanic effect, there is a spin polarization of
145 the conduction electrons near Mn sites. The spin polarization is staggered across the two
146 Mn sublattices and through exchange coupling, a torque is experienced by the Mn moments.
147 From the example of CuMnAs above, we can search for compounds from databases that are
148 antiferromagnets or are likely to be antiferromagnets where the magnetic atoms sit on a polar
149 point group. Such a search can be made for compounds which are not complicated by the
150 presence of many magnetic sites with different point groups. The general case applicable for
151 all magnetic compounds will be considered in the following sections. Following is the general
152 procedure for extracting potential metallic antiferromagnet candidates from databases -

- 153 1. Search for known metallic antiferromagnets from database having tetragonal, trigonal
154 or hexagonal crystal system.
- 155 2. Remove duplicate and non-centrosymmetric compounds.
- 156 3. Identify the Néel temperature and magnetic ordering.
- 157 4. Filter out compounds having Néel temperature > 300 K.
- 158 5. Identify the nature of atomic site symmetry and select compounds.
- 159 6. Study available literature to see if any compounds can be synthesized as single crystals.

160 This procedure assumes that we are starting with a collection of known or possible metallic
161 antiferromagnets. This is true in case of compounds downloaded from MPDS. In case of ASM
162 database, the compounds are metallic but their magnetism is not known beforehand. We will
163 have to make some assumptions based on the chemical nature and stoichiometry of the ions
164 present in the compound in order to select possible antiferromagnets. Tetragonal, trigonal
165 or hexagonal crystal systems are preferred since they allow for the presence of multiple
166 degenerate axes for Néel vector orientation. It is still important to check if the magnetic
167 structure for the compound is known or not and if the Néel vector points along the degerate
168 axes. Carrying out the above mentioned steps for compounds in MPDS and ASM database
169 gives us a list of compounds in Table 2.2 that have been grouped together based on their
170 structure types.

171 The first group of compounds consist of materials in MoSi_2 structure type. Mn_2Au is a
172 well-known compound that has been extensively studied for electrical switching applications
173 [12, 27]. Cr_2Al powders can be prepared using traditional solid state synthesis routes by
174 heating to above 850°C [28]. Early neutron diffraction experiments suggest Cr moments align

Table 2.2: List of metallic antiferromagnetic candidates filtered out from MPDS and ASM database and their metal atom site symmetries

Structure type	List of compounds	Point group	Magnetism
MoSi ₂	Mn ₂ Au, Cr ₂ Al, Ni ₂ Ta	C _{4v}	Mn ₂ Au is a known candidate
HfFe ₆ Ge ₆	ScFe ₆ Ge ₆	C _{2v}	AFM with Néel vector along <i>c</i>
Mg ₃ Cd	Mn ₃ Ga, Mn ₃ Ge, Mn ₃ Sn, Fe ₃ Ga, Co ₃ Mo, Co ₃ W, Ni ₃ In, Ni ₃ Sn, Ni ₃ Zr	C _{2v}	Non-collinear AFM
IrIn ₃	CoGa ₃ , CoIn ₃ , FeGa ₃	C _{2v}	FeGa ₃ and CoGa ₃ are diamagnets
MoNi ₄	MoNi ₄ , WNi ₄	C _{1v}	Unknown
Ni ₂ Al ₃	Ni ₂ Al ₃ , Ni ₂ Ga ₃ , Ni ₂ In ₃	C _{3v}	Unknown

at 65° to the *ab* plane [29]. However, a later article indicates that the determined magnetic structure may not be correct [30]. Regardless of whether the moments align in the *ab* plane or not, Cr₂Al is an interesting candidate to study electrical switching behavior. ScFe₆Ge₆ is AFM at room temperature [31]. However, the Fe moments align along *c* and does not satisfy our criteria [32]. Compounds in the Mg₃Cd structure type contain Kagome lattice of magnetic atoms. Mn₃Sn and Mn₃Ge are known to have a non-collinear spin arrangement. They have become popular recently for showing large anomalous hall and spin hall effect behavior [33–35]. Electrical switching was also demonstrated in Mn₃Sn recently. In the fourth group of compounds, both FeGa₃ and CoGa₃ are known to show diamagnetic properties and hence they can be discarded [36–38]. The magnetism is unknown in the final two groups of compounds in MoNi₄ and Ni₂Al₃ structure types and most of these compounds can be synthesized by the arc melting process [39,40].

2.3 Components of torque from non-equilibrium CISP

The previous section dealt with relatively simple magnetic compounds that had only one magnetic atom site and we were concerned with the point group of the site to determine whether the inverse spin galvanic effect would be observed or not. In the simplest sense, antidamping-like STT is induced by spin hall effect (SHE) and fieldlike SOT is generated from inverse spin galvanic effect. However, incomplete absorption of the spin current from SHE by the FM layer may produce a fieldlike torque, and spin relaxation and damping may induce an antidamping like component to the SOT [11]. Using Kubo linear formalism, we

195 can write CISP $\delta S_a = \chi_a E$ where E is the applied electric field and χ_a is the linear response
 196 tensor for the sublattice a. χ_a can be further divided into three components:

$$\chi_a = \chi_a^I + \chi_a^{II(a)} + \chi_a^{II(b)} \quad (2.1)$$

197 where χ_a^I is the intraband term, and $\chi_a^{II(a)}$ and $\chi_a^{II(b)}$ are the interband terms. χ_a can also
 198 be broken down into even and odd terms:

$$\chi_a = \chi_a^{even} + \chi_a^{odd} \quad (2.2)$$

199 where $\chi_a^{even} = (\chi_a([M]) + \chi_a([-M]))/2$ and $\chi_a^{odd} = (\chi_a([M]) - \chi_a([-M]))/2$. From the
 200 symmetry of the operators and the matrix element, it follows that -

$$\chi_a^{even} = \chi_a^I + \chi_a^{II(b)} \quad (2.3)$$

$$\chi_a^{odd} = \chi_a^{II(a)} \quad (2.4)$$

201 We assume that the system only has a weak disorder and hence, we can neglect $\chi_a^{II(b)}$. χ_a
 202 also depends on the direction of the magnetic moments where \hat{n} is the direction of the Néel
 203 vector.

$$\chi_{a,i,j}(\hat{n}) = \chi_{a,i,j}^{(0)} + \chi_{a,i,j,k}^{(1)} \hat{n}_k + \chi_{a,i,j,k,l}^{(2)} \hat{n}_k \hat{n}_l + \dots \quad (2.5)$$

204 where the sum of the first term and every alternate term after that corresponds to χ_a^{even} and
 205 the sum of the remaining terms correspond to χ_a^{odd} . $\chi_a^{(0)}$ is usually dominant, independent
 206 of magnetization and contributes to field-like torque. $\chi_a^{(1)}$ contributes to anti-damping like
 207 torque and $\chi_a^{(2)}$ can be neglected if $\chi_a^{(0)}$ is not 0 [11]. The zeroth order term which contributes
 208 to a fieldlike torque consists of three components in the form of generalized Rashba and
 209 generalized Dresselhaus terms and a term that is proportional to the electric field as shown
 210 by the following equations:

$$\text{Generalized Rashba } \chi_a^{gR} = \begin{bmatrix} \chi_{11} & -\chi_{21} & 0 \\ \chi_{21} & \chi_{11} & 0 \\ 0 & 0 & 0 \end{bmatrix} \quad (2.6)$$

$$\text{Generalized Dresselhaus } \chi_a^{gD} = \begin{bmatrix} \chi_{11} & \chi_{21} & 0 \\ \chi_{21} & -\chi_{11} & 0 \\ 0 & 0 & 0 \end{bmatrix} \quad (2.7)$$

Table 2.3: Summary of the linear response tensor components for the CISP observable and electric field

	χ_a^I	$\chi_a^{II(a)}$	$\chi_a^{II(b)}$
Component	Intraband	Interband (imaginary)	Interband (real)
Disorder $\Gamma \rightarrow 0$	Diverges	Constant	Zero
Cause	Non-equilibrium Fermi-Dirac distribution	Intrinsic change in carrier wave function	Change in carrier wave function due to disorder/defects
Alternate name	χ_a^{even} or $\chi_a^{(0)}$	χ_a^{odd} or $\chi_a^{(1)}$	
Dependence on magnetization	Independent	Dependent	
Torque	Field-like	Anti-damping-like	

$$\text{Proportional to Electric field } \chi_a^E = \begin{bmatrix} \chi_{11} & 0 & 0 \\ 0 & \chi_{11} & 0 \\ 0 & 0 & \chi_{11} \end{bmatrix} \quad (2.8)$$

211 Similarly, the first order term can also be broken into three different components [11]. The
 212 summary of the linear response tensor components is also provided in the Table 2.3

213 2.4 Spin polarization in CuMnAs, Mn₂Au and Fe₂As

214 Zelezny *et al.* [11] provides a python code *symmetr* for analyzing the linear response tensor
 215 for a number of observables such as current, spin, torque, position, spin current etc. and
 216 electric field. Using this code, we can test the reponse tensor of known compounds such
 217 as CuMnAs and Mn₂Au and also check for unknown compounds such as Fe₂As. Table
 218 shows the linear response tensor in case of CuMnAs or Mn₂Au. Both compounds have
 219 same spin polarization since they are both globally centrosymmetric and Mn atoms sit on
 220 C_{4v} point group sites. Let us first understand χ^{even} for all the different cases presented here.
 221 Magnetism can be turned off to avoid including magnetization-based effects to the reponse
 222 tensor. Regardless of whether we toggle magnetism in Mn atoms or not, χ^{even} is 0 for the
 223 whole unit cell since it is centrosymmetric. When Mn magnetic moment is set to 0, χ^{even} for
 224 each sublattice corresponds to the response in conventional Rashba spin texture. Regardless
 225 of magnetism, the spin polarization in one site is opposite to that of another site as seen in
 226 the projected cases. When magnetism is turned on, $|\chi_{10}| = |\chi_{01}|$ is not valid anymore since
 227 we also have to consider higher terms in χ^{even} . In case of χ^{odd} , it is 0 when magnetization is

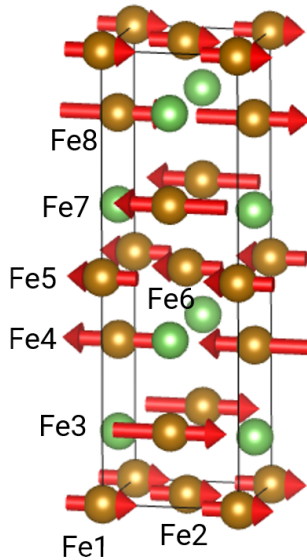


Figure 2.2: Magnetic structure of Fe_2As along with the Fe site numbers corresponding to Table 2.5.

228 turned off as also shown in Table 2.3. When magnetic moments are allowed, there is spin
229 polarization along c direction.

230 Table 2.5 shows linear response tensor components in Fe_2As . Fe_2As is complicated by the
231 presence of two different Fe sites. $\text{Fe}1$, $\text{Fe}2$, $\text{Fe}5$ and $\text{Fe}6$ atoms shown in Fig. 2.2 sit on D_{2d}
232 site whereas $\text{Fe}3$, $\text{Fe}4$, $\text{Fe}7$ and $\text{Fe}8$ atoms sit on C_{4v} sites. The table only shows cases where
233 Fe moments have not been considered. However, the results with finite Fe moments in case of
234 χ^{even} can be easily inferred from this table by removing the equality between the magnitudes
235 of χ_{ij} and χ_{ji} . As expected, χ^{odd} is a zero matrix when magnetism is turned off. χ^{even} is 0
236 when the entire unit cell is considered which is expected since the unit cell is centrosymmetric
237 like in the previous case. The sublattices $\text{Fe}3$ and $\text{Fe}4$ sitting on polar point groups show
238 conventional Rashba spin polarization behavior. When χ^{even} at $\text{Fe}3$ is projected onto $\text{Fe}4$, we
239 can see that the response is exactly opposite to $\text{Fe}4$. In case of sublattices $\text{Fe}1$ and $\text{Fe}2$ sitting
240 on non-polar point groups, χ^{even} corresponds to generalized Dresselhaus polarization when
241 χ_{00} and χ_{11} have been set to 0. As expected, the spin polarization would be opposite on the
242 two sublattices. The nature of χ^{odd} when magnetism is included has not been discussed here.

243 2.5 Conclusions

244 There can be local spin polarization present even in centrosymmetric crystals provided the
245 unit cell contains non-centrosymmetric point groups. In CISP based switching, it is important
246 that the magnetic ions sit on non-centrosymmetric sites. The presence of polar point group

Table 2.4: Linear response tensor in CuMnAs and Mn₂Au assuming Mn moment to be 1 μ_B .

	χ^{even}	χ^{odd}
Magnetic Mn. For the entire unit cell	$\begin{bmatrix} 0 & 0 & 0 \\ 0 & 0 & 0 \\ 0 & 0 & 0 \end{bmatrix}$	$\begin{bmatrix} 0 & 0 & \chi_{02} \\ 0 & 0 & 0 \\ \chi_{20} & 0 & 0 \end{bmatrix}$
Magnetic Mn. For each Mn sublattice	$\begin{bmatrix} 0 & \chi_{01} & 0 \\ \chi_{10} & 0 & 0 \\ 0 & 0 & 0 \end{bmatrix}$	$\begin{bmatrix} 0 & 0 & \chi_{02} \\ 0 & 0 & 0 \\ \chi_{20} & 0 & 0 \end{bmatrix}$
Magnetic Mn. For one Mn sublattice projected onto another	$\begin{bmatrix} 0 & -\chi_{01} & 0 \\ -\chi_{10} & 0 & 0 \\ 0 & 0 & 0 \end{bmatrix}$	$\begin{bmatrix} 0 & 0 & \chi_{02} \\ 0 & 0 & 0 \\ \chi_{20} & 0 & 0 \end{bmatrix}$
Non-magnetic Mn. For the entire unit cell	$\begin{bmatrix} 0 & 0 & 0 \\ 0 & 0 & 0 \\ 0 & 0 & 0 \end{bmatrix}$	$\begin{bmatrix} 0 & 0 & 0 \\ 0 & 0 & 0 \\ 0 & 0 & 0 \end{bmatrix}$
Non-magnetic Mn. For each Mn sublattice	$\begin{bmatrix} 0 & -\chi_{10} & 0 \\ \chi_{10} & 0 & 0 \\ 0 & 0 & 0 \end{bmatrix}$	$\begin{bmatrix} 0 & 0 & 0 \\ 0 & 0 & 0 \\ 0 & 0 & 0 \end{bmatrix}$
Non-magnetic Mn. For one Mn sublattice projected onto another	$\begin{bmatrix} 0 & \chi_{10} & 0 \\ -\chi_{10} & 0 & 0 \\ 0 & 0 & 0 \end{bmatrix}$	$\begin{bmatrix} 0 & 0 & 0 \\ 0 & 0 & 0 \\ 0 & 0 & 0 \end{bmatrix}$

Table 2.5: Linear response tensor in Fe₂As when Fe moments have been set to 0 μ_B .

	χ^{even}	χ^{odd}
For the entire unit cell	$\begin{bmatrix} 0 & 0 & 0 \\ 0 & 0 & 0 \\ 0 & 0 & 0 \end{bmatrix}$	$\begin{bmatrix} 0 & 0 & 0 \\ 0 & 0 & 0 \\ 0 & 0 & 0 \end{bmatrix}$
For Fe1 and Fe2	$\begin{bmatrix} 0 & \chi_{10} & 0 \\ \chi_{10} & 0 & 0 \\ 0 & 0 & 0 \end{bmatrix}$	$\begin{bmatrix} 0 & 0 & 0 \\ 0 & 0 & 0 \\ 0 & 0 & 0 \end{bmatrix}$
For Fe3 and Fe4	$\begin{bmatrix} 0 & -\chi_{10} & 0 \\ \chi_{10} & 0 & 0 \\ 0 & 0 & 0 \end{bmatrix}$	$\begin{bmatrix} 0 & 0 & 0 \\ 0 & 0 & 0 \\ 0 & 0 & 0 \end{bmatrix}$
For Fe1 projected onto Fe2	$\begin{bmatrix} 0 & -\chi_{10} & 0 \\ -\chi_{10} & 0 & 0 \\ 0 & 0 & 0 \end{bmatrix}$	$\begin{bmatrix} 0 & 0 & 0 \\ 0 & 0 & 0 \\ 0 & 0 & 0 \end{bmatrix}$
For Fe3 projected onto Fe4	$\begin{bmatrix} 0 & \chi_{10} & 0 \\ -\chi_{10} & 0 & 0 \\ 0 & 0 & 0 \end{bmatrix}$	$\begin{bmatrix} 0 & 0 & 0 \\ 0 & 0 & 0 \\ 0 & 0 & 0 \end{bmatrix}$
For Fe1 projected onto Fe3	No relation	No relation

247 is required for Rashba spin polarization and non-polar point group for Dresselhaus spin
248 polarization. We need to consider both antidamping-like torque and fieldlike torque when
249 considering spin polarization. In broken inversion symmetry 2D AFM, it is the antidamping-
250 like torque that can provide a mechanism for switching since the fieldlike torque component
251 of CISP is uniform. In Fe₂As, CISP from ISGE in Fe3 and Fe4 sublattices is similar to Mn in
252 CuMnAs. However, there is no relation between the even component of CISP in Fe1 or Fe2
253 and Fe3 or Fe4 sublattices. This allows for two possibilities when the current is along [100].
254 If the torque acts in the same direction for both sets of Fe atoms, then it would provide a
255 possible pathway for switching. However, if the fieldlike torque act in the opposite direction
256 for both sets of Fe moments, then a large current threshold may be required before the
257 moments can be possibly switched.

258 **2.6 Acknowledgements**

259 I would like to acknowledge two REU students, Scott Berens and Carmen Paquette, for
260 compiling the list of metallic antiferromagnets from MPDS and ASM databases respectively.
261 It saved me a lot of time and I was able to analyze the symmetry requirements on a much
262 smaller list of compounds.

Chapter 3

Materials synthesis and characterization

263 3.1 Bulk materials synthesis

264 Bulk polycrystalline and single crystals of all the samples are prepared by traditional solid
265 state synthesis routes. The process of synthesizing these samples is shown in Fig. 3.1. The
266 constituent elements of the compounds are mixed in certain ratio using a mortar and pestle
267 in an Argon atmosphere glovebox shown in Fig. 3.1(a). Quartz tubes, that have been sealed
268 from one side, are filled with the mixed elemental powders and vacuum sealed using a
269 flame torch as shown in Fig. 3.1(b). The sealed quartz tubes in Fig. 3.1(c) are placed inside
270 a box furnace and heated to a high temperature to allow the powders to fuse together as
271 shown in Fig. 3.1(d). Upon cooling, the desired crystal is removed from the quartz tube and
272 characterized.

273 3.1.1 Sensitivity of Fe:As stoichiometry in the synthesis of Fe_2As

274 Fe_2As crystals are prepared by mixing Fe and As powders inside the glovebox and heating
275 it up to 600°C at $1^\circ\text{C}/\text{min}$, holding it for 6 h and then heating it above the melting point to
276 975°C at $1^\circ\text{C}/\text{min}$. The sample is held at 975°C for 1 h before cooling it down to 900°C at
277 $1^\circ\text{C}/\text{min}$ and held for 1 h. Finally, the sample is allowed to furnace-cool down to the room
278 temperature. The source of the Fe powders seems to have significant effect on the optimum
279 Fe:As starting stoichiometry. As powders were obtained by grinding As chunks (Alfa Aesar,
280 2-8mm, 99.9999% (metals basis)) using a mortar and pestle. Fig. ?? shows the impurity
281 percentage as a function of Fe:As stoichiometry for Fe powders (Alfa Aesar, -200 mesh, 99+%\n
282 (metals basis)) with $0.74 \mu\text{m}$ in size. Phase pure Fe_2As is obtained for Fe:As ratio of 1.95:1.
283 Increasing the Fe content results in Fe impurity and decreasing Fe content results in FeAs
284 impurity.

285 While using the 200 mesh size Fe powders yielded pure Fe_2As , the residual resistivity ratio
286 from the transport measurements indicated Fe_2As to be a bad metal. In an attempt to reduce
287 the presence of trace impurities, more pure Fe powders were sourced. Fe powders (Alfa
288 Aesar, $10 \mu\text{m}$, spherical, >99.99% (metals basis)) with $10 \mu\text{m}$ in size were used for preparing
289 batches of 1 g of Fe_2As crystals. In order to reduce processing errors, before vacuum sealing

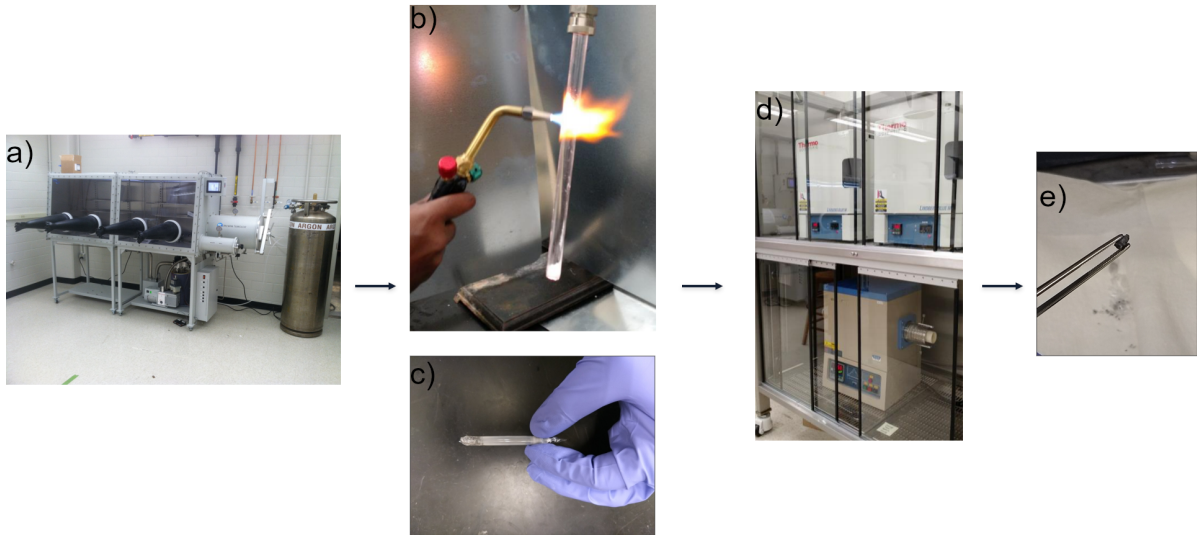


Figure 3.1: The process of making bulk materials using traditional solid state synthesis technique is shown here. The powders mixed inside the glovebox in (a) are transferred to a quartz tube and vacuum sealed in (b). The vacuum sealed ampoule in (c) is placed inside the box furnace in (d) and subjected to a heating profile. (e) shows the final ingot obtained in case of CuMnAs sample.

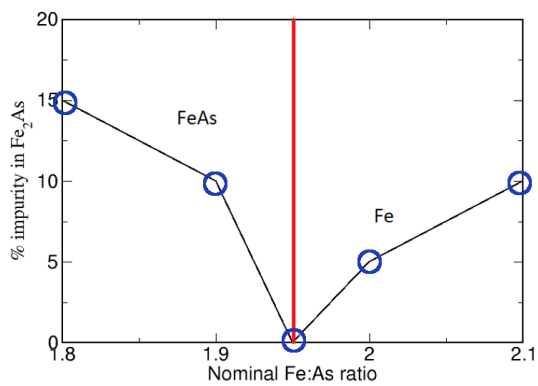


Figure 3.2: Impurity percentage as a function of Fe:As starting stoichiometry ratio with 200 mesh size Fe powders for making Fe₂As samples.

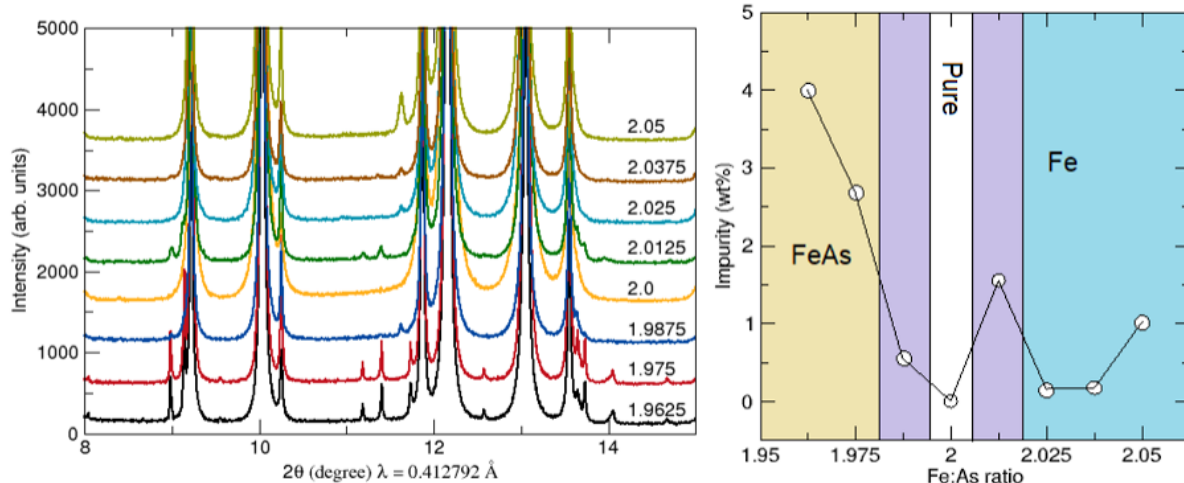


Figure 3.3: Synchrotron x-ray diffraction data of Fe_2As for different ratios of Fe:As from 10 μm Fe powders is shown in (a) and the corresponding impurity percentage is shown in (b).

290 the quartz tube, a magnet was moved from top to bottom of the outer walls of the tube in a
 291 rocking fashion to remove any Fe powders sticking to the inner walls of the tube. Finally, the
 292 synthesized Fe_2As crystals were crushed into powders and sent to the 11-BM beamline at the
 293 Advanced Photon Source in Argonne National Laboratory for synchrotron x-ray diffraction
 294 measurements. The results of the 8 samples with different Fe:As ratio is shown in Fig. 3.3(a).
 295 The results from this data suggest that Fe:As ratio of 2:1 which is also the stoichiometric ratio,
 296 is optimum to produce phase pure samples as shown in Fig. 3.3(b). Similar to earlier results,
 297 increasing the Fe:As ratio above 2 precipitates out Fe impurity and decreasing the Fe:As ratio
 298 results in FeAs impurity. The region colored in purple in Fig. 3.3(b) contained the opposite of
 299 the expected impurity. The purple region on the excess Fe side contained FeAs impurity and
 300 on the lower Fe side contained Fe impurity. I attribute this inconsistency to random errors.

301 3.2 Synthesis of compounds in the Cu-Mn-As system

302 Compounds in the Cu-Mn-As system powders are synthesized by mixing Cu powders (Alfa
 303 Aesar, -100+325 mesh, spherical, 99.9% (metals basis)), Mn powders ground from Mn chips
 304 (99.98% (metals basis)) and As powders ground from chunks (Alfa Aesar, 2-8mm, 99.9999%
 305 (metals basis)) inside the Ar atmosphere and following the same heating procedure as in
 306 the case of Fe_2As . To synthesize binary compounds Mn_2As and Mn_3As_2 , excess Mn has
 307 to be added into the mixture. Mn:As ratio of 2.1:1 and 3.1:2 is required to synthesize pure
 308 phase Mn_2As and Mn_3As_2 , respectively. In case of Mn_2As , when Mn and As powders are
 309 mixed in stoichiometric ratio, Mn_3As_2 impurity is formed due to peritectic reaction [41].

310 The ratio of Cu:Mn:As powders determines the final product. When Cu:Mn:As ratio is
311 0.82:1.18:1, the hexagonal polymorph of CuMnAs is stabilized. From literature, when Cu,
312 Mn and As powders are mixed in equal proportions, orthorhombic CuMnAs is formed.
313 However, in our synthesis procedure, we observe a mixture of tetragonal and orthorhombic
314 CuMnAs. The difference in the final product comes from the use of an Alumina crucible
315 inside the quartz tube. I have synthesized tetragonal CuMnAs by substituting equal amounts
316 of Mn with Cu powders. An almost stoichiometric tetragonal CuMnAs has been reported
317 in literature by substituting small amounts of Mn with As [42]. I also synthesized the near
318 stoichiometric tetragonal CuMnAs by replicating the procedure from literature including
319 the use of Alumina crucible. The heating procedure has a significant impact on the quality
320 of the tetragonal CuMnAs crystals. Tetragonal CuMnAs undergoes a phase transition at
321 around 800°C which makes it difficult to synthesize large crystals using traditional solid state
322 synthesis routes. Out of the three elemental powders, Cu is the element that is being directly
323 used in the powder form. Hence, it is prone to oxidation easily. However, Cu powders can
324 be easily reduced using H₂ gas flow reaction by heating it to 600°C for holding it for 6 hours.

325 3.3 Materials characterization

326 3.3.1 X-ray diffraction measurements

327 Powder x-ray diffraction measurements were carried out primarily at the Bruker D8 Advance
328 powder x-ray diffractometer with Mo source using the capillary stage. Since the materials
329 used here contain As and other transition metal atoms which absorb x-rays significantly, thin
330 capillaries of 0.43 mm in diameter were used. In addition to that, the powders were diluted
331 with appropriate amounts of amorphous silica to account for x-ray absorption. Most powder
332 x-ray diffraction measurements on Cu-Mn-As samples were carried out on the Bruker D8
333 Advance x-ray diffractometer with Cu source using a reflective stage. In these measurements,
334 the samples were not diluted with silica since absorption is not an issue. However, significant
335 sample texturing was observed which had to be taken into account while carrying out
336 Rietveld refinement. Certain samples were also measured at the 11-BM beamline of the
337 Advanced Photon Source in Argonne National Laboratory. The powders were mounted
338 onto 0.7 mm diameter quartz capillaries and vacuum sealed before fitting it inside a Kapton
339 capillary for measurement. The high energy synchrotron beam wavelength that was used at
340 11-BM beamline corresponds to 0.4128 Å. Rietveld refinement of the powder x-ray diffraction
341 data was carried out using TOPAS and GSAS-II [43,44].

342 Hexagonal Cu_{0.82}Mn_{1.18}As crystals were sent to SCS X-ray facility for single crystal x-ray
343 diffraction measurement on a Bruker X8 Apex II diffractometer. Tiny single crystals of the
344 size of around 100 μm were fractured out from a large ingot and used for the measurement.
345 Alignment of large single crystals of Fe₂As and Cu_{0.82}Mn_{1.18}As for the purpose of aligned

346 SQUID magnetometry, magnetotransport and inelastic neutron scattering measurements
347 were carried out using a Laue System with a Multiwire 2D Detector at both MRL x-ray
348 laboratory as well as at Spallation Neutron Source. The Laue diffractometer was only used
349 to align samples from the symmetry of the Laue pattern. Indexing of the patterns were not
350 carried out using the Northstar software due to issues with the software. The out-of-plane
351 alignment in Cu_{0.82}Mn_{1.18}As single crystal was also confirmed using the reflective stage of
352 Bruker D8 Advance diffractometer with Mo source.

353 **3.3.2 SEM/EDS measurements**

354 **3.3.3 Calorimetry measurements**

355 Thermogravimetric analysis (TGA) is a thermal analysis technique where the mass of the
356 sample is tracked over a range of temperatures. It is particularly useful for detecting changes
357 such as sublimation or evaporation of a phase or any kind of absorption/desorption processes.
358 Powders or crystals of around 10 mg can be loaded onto an Alumina cup and heated up to
359 1000°C for TGA. All the samples were measured in the Q50 TGA instrument upto above
360 400°C under N₂ atmosphere to check if the sample loses its integrity at this temperature range
361 or not. No transitions were observed in any of the samples measured and further analysis
362 was carried out using differential scanning calorimetry (DSC). This measurement technique,
363 although not very useful in this case, is necessary to prevent any accidental coating of the
364 inner chamber during DSC measurements.

365 DSC is a calorimetry technique where the difference in the heat required to keep the sample
366 at the same temperature as the reference is recorded as a function of temperature. It is a
367 sensitive measurement technique and is useful for detecting magnetic transitions such as the
368 Néel temperature or any spin canting transition. DSC measurements for all samples were
369 carried out in the DSC2500 instrument. The sample powders, weighing between 4 mg to
370 8 mg, were loaded onto Alumina pans and subjected to heat-cool-heat cycles between -180°C
371 and 400° at 10°C/min.

372 Differential thermal analysis (DTA) is similar to DSC except that the temperature difference
373 between the sample and reference is recorded for identical thermal cycles. DTA measure-
374 ments were carried out on a Shimadzu DTA-50 up to 1200°C in some samples at a heating
375 rate of 20°C/min under N₂ atmosphere. The advantage of using DTA is that it can go up
376 to very high temperatures which is useful for detecting melting point and any other phase
377 transition that is beyond the range of DSC. The presence of As in the samples makes it im-
378 possible to use the standard DTA Alumina cups for measurement. To prevent contamination
379 of the room with As vapors, special quartz ampoules were designed and commissioned from
380 the SCS Glass shop. The ampoules were made by cutting 3 mm and 4 mm OD quartz tubes
381 in 85 mm lengths and creating a flat-bottom bulb of 5 mm diameter at one end of the tube as

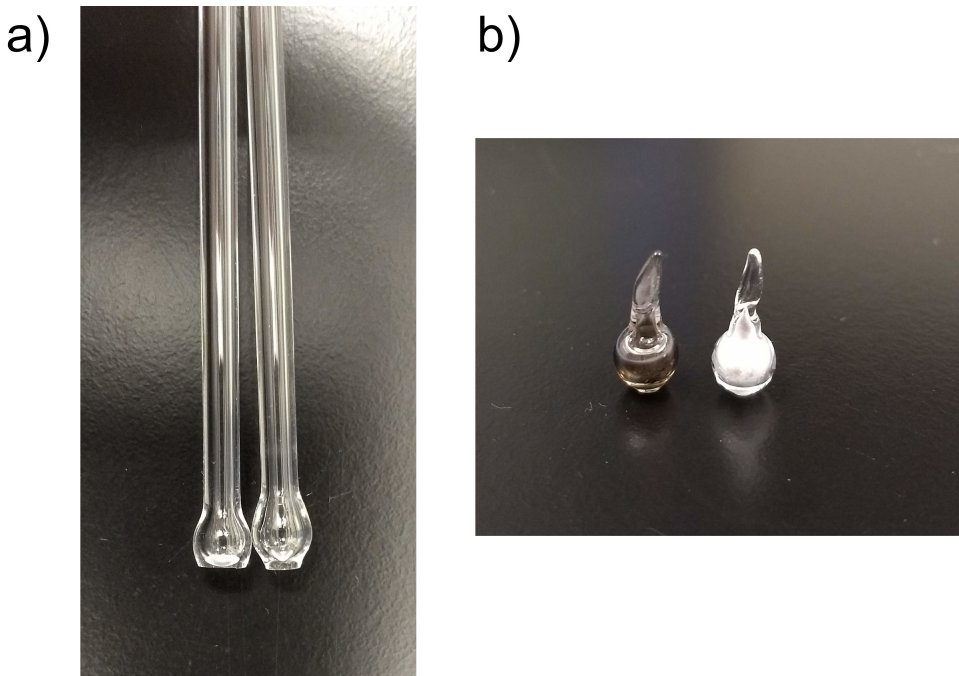


Figure 3.4: The flat-bottom bulk of the quartz ampoules is shown in (a) and (b) shows the final powder-containing vacuum sealed ampoules.

382 shown in Fig. 3.4(a). About 20 mg to 40 mg of sample powders were vacuum sealed in the
383 quartz ampoules and similar amount of Alumina powder was sealed as reference as shown
384 in Fig. 3.4(b). The use of quartz ampoules, however, prevents detection of subtle transitions
385 such as magnetic transitions. Hence, DTA can be used in conjunction with DSC to identify
386 all transition temperatures.

387 **3.3.4 SQUID magnetometry measurements**

388 SQUID measurements for all the samples were carried out in a Quantum Design MPMS3
389 (Magnetic Property Measurement System) in the DC mode. The DC moment was tracked
390 as a function of applied field as well as temperature. In magnetic hysteresis measurements,
391 fields up to 10 kOe were applied across six quadrants to account for the initial magnetization
392 curve. Field cooling measurements refer to the application of magnetic field at 400°C followed
393 by cooling of the sample. Zero field cooling measurements are carried out by first cooling
394 the sample in the absence of a field, followed by the application of an external field and
395 then, heating the sample. The sample moment is measured at certain intervals across the
396 temperature range. The SQUID measurements have been carried out for the powders of
397 Fe₂As, Cu_{0.82}Mn_{1.18}As, tetragonal CuMnAs and Mn₃As₂, and the single crystals of Fe₂As
398 and Cu_{0.82}Mn_{1.18}As. In case of powders, 20 mg to 40 mg of powders were filled into a VSM
399 powder sample holder inside the Ar atmosphere glovebox. This capillary was snapped onto

400 a MPMS3 brass half tube sample holder and wrapped with a small amount of insulating tape
401 to keep it fixed. For single crystal measurements, aligned samples were fixed on the MPMS3
402 Quartz Paddle Sample Holder using GE Varnish and later removed using ethanol.

403 **3.3.5 Magnetotransport measurements**

404 Magnetotransport measurements for hexagonal Cu_{0.82}Mn_{1.18}As were carried out in a Quan-
405 tum Design Physical Property Measurement System Dynacool.

406 **3.4 Neutron scattering**

407 **3.4.1 Neutron powder diffraction**

408 **3.4.2 Inelastic neutron scattering**

Chapter 4

Magnetic structure refinement from neutron diffraction measurements

409 Lorem ipsum dolor sit amet, consectetur adipiscing elit. Etiam lobortis facilisis sem. Nullam
410 nec mi et neque pharetra sollicitudin. Praesent imperdiet mi nec ante. Donec ullamcorper,
411 felis non sodales commodo, lectus velit ultrices augue, a dignissim nibh lectus placerat pede.
412 Vivamus nunc nunc, molestie ut, ultricies vel, semper in, velit. Ut porttitor. Praesent in sapien.
413 Lorem ipsum dolor sit amet, consectetur adipiscing elit. Duis fringilla tristique neque. Sed
414 interdum libero ut metus. Pellentesque placerat. Nam rutrum augue a leo. Morbi sed elit sit
415 amet ante lobortis sollicitudin. Praesent blandit blandit mauris. Praesent lectus tellus, aliquet
416 aliquam, luctus a, egestas a, turpis. Mauris lacinia lorem sit amet ipsum. Nunc quis urna
417 dictum turpis accumsan semper.

418 Lorem ipsum dolor sit amet, consectetur adipiscing elit. Etiam lobortis facilisis sem.
419 Nullam nec mi et neque pharetra sollicitudin. Praesent imperdiet mi nec ante. Donec
420 ullamcorper, felis non sodales commodo, lectus velit ultrices augue, a dignissim nibh lectus
421 placerat pede. Vivamus nunc nunc, molestie ut, ultricies vel, semper in, velit. Ut porttitor.
422 Praesent in sapien. Lorem ipsum dolor sit amet, consectetur adipiscing elit. Duis fringilla
423 tristique neque. Sed interdum libero ut metus. Pellentesque placerat. Nam rutrum augue
424 a leo. Morbi sed elit sit amet ante lobortis sollicitudin. Praesent blandit blandit mauris.
425 Praesent lectus tellus, aliquet aliquam, luctus a, egestas a, turpis. Mauris lacinia lorem sit
426 amet ipsum. Nunc quis urna dictum turpis accumsan semper.

427 Lorem ipsum dolor sit amet, consectetur adipiscing elit. Etiam lobortis facilisis sem.
428 Nullam nec mi et neque pharetra sollicitudin. Praesent imperdiet mi nec ante. Donec
429 ullamcorper, felis non sodales commodo, lectus velit ultrices augue, a dignissim nibh lectus
430 placerat pede. Vivamus nunc nunc, molestie ut, ultricies vel, semper in, velit. Ut porttitor.
431 Praesent in sapien. Lorem ipsum dolor sit amet, consectetur adipiscing elit. Duis fringilla
432 tristique neque. Sed interdum libero ut metus. Pellentesque placerat. Nam rutrum augue
433 a leo. Morbi sed elit sit amet ante lobortis sollicitudin. Praesent blandit blandit mauris.
434 Praesent lectus tellus, aliquet aliquam, luctus a, egestas a, turpis. Mauris lacinia lorem sit
435 amet ipsum. Nunc quis urna dictum turpis accumsan semper.

436 Lorem ipsum dolor sit amet, consectetur adipiscing elit. Etiam lobortis facilisis sem.
437 Nullam nec mi et neque pharetra sollicitudin. Praesent imperdiet mi nec ante. Donec
438 ullamcorper, felis non sodales commodo, lectus velit ultrices augue, a dignissim nibh lectus

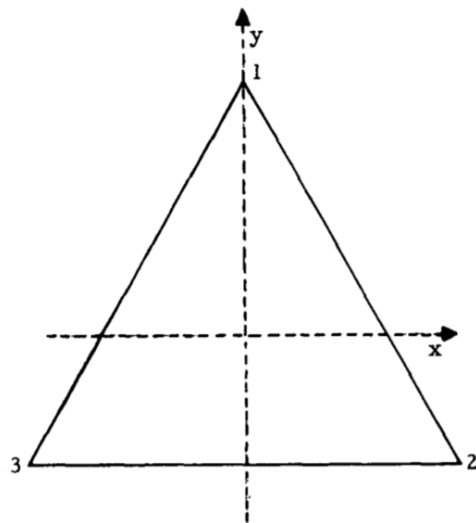


Figure 4.1: Electronic band structure

	E	C_3	C_3^2	σ_1	σ_2	σ_3
E	E	C_3	C_3^2	σ_1	σ_2	σ_3
C_3	C_3	C_3^2	E	σ_3	σ_1	σ_2
C_3^2	C_3^2	E	C_3	σ_2	σ_3	σ_1
σ_1	σ_1	σ_2	σ_3	E	C_3	C_3^2
σ_2	σ_2	σ_3	σ_1	C_3^2	E	C_3
σ_3	σ_3	σ_1	σ_2	C_3	C_3^2	E

Figure 4.2: Electronic band structure

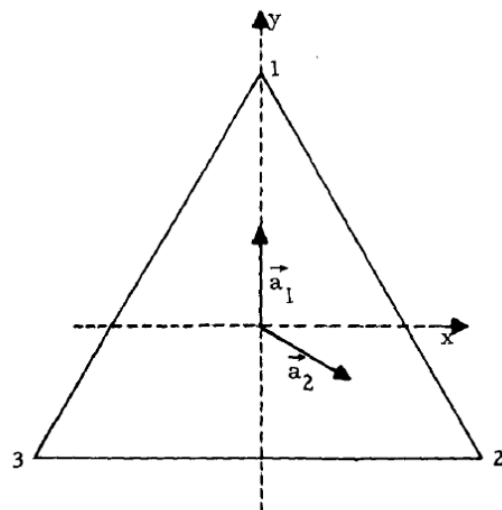


Figure 4.3: Electronic band structure

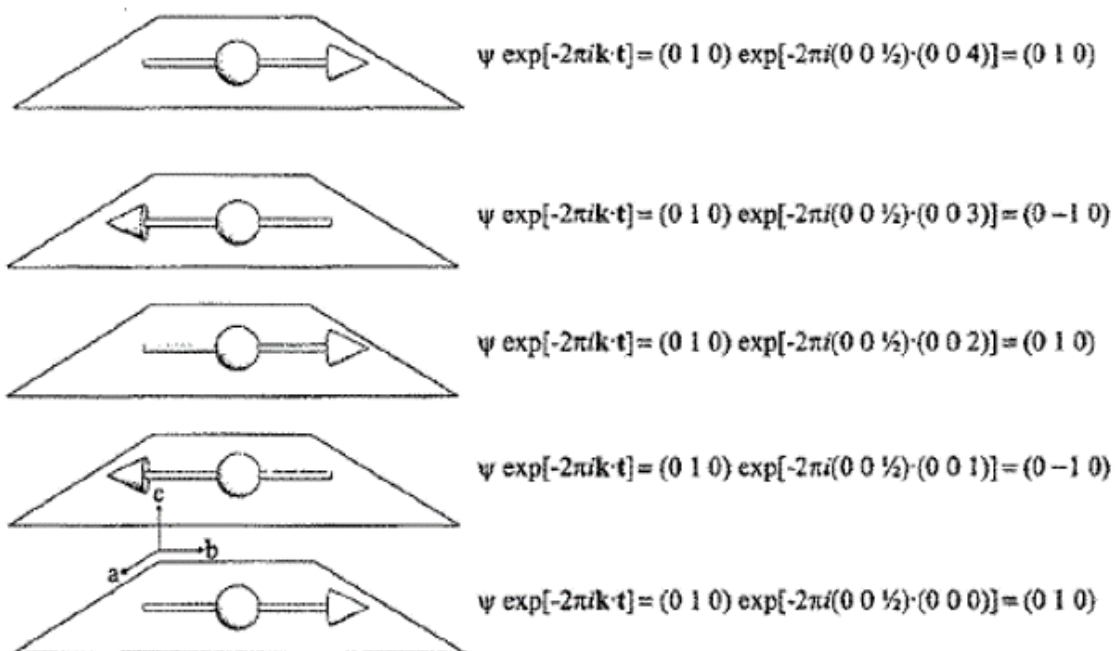


Figure 4.4: Electronic band structure

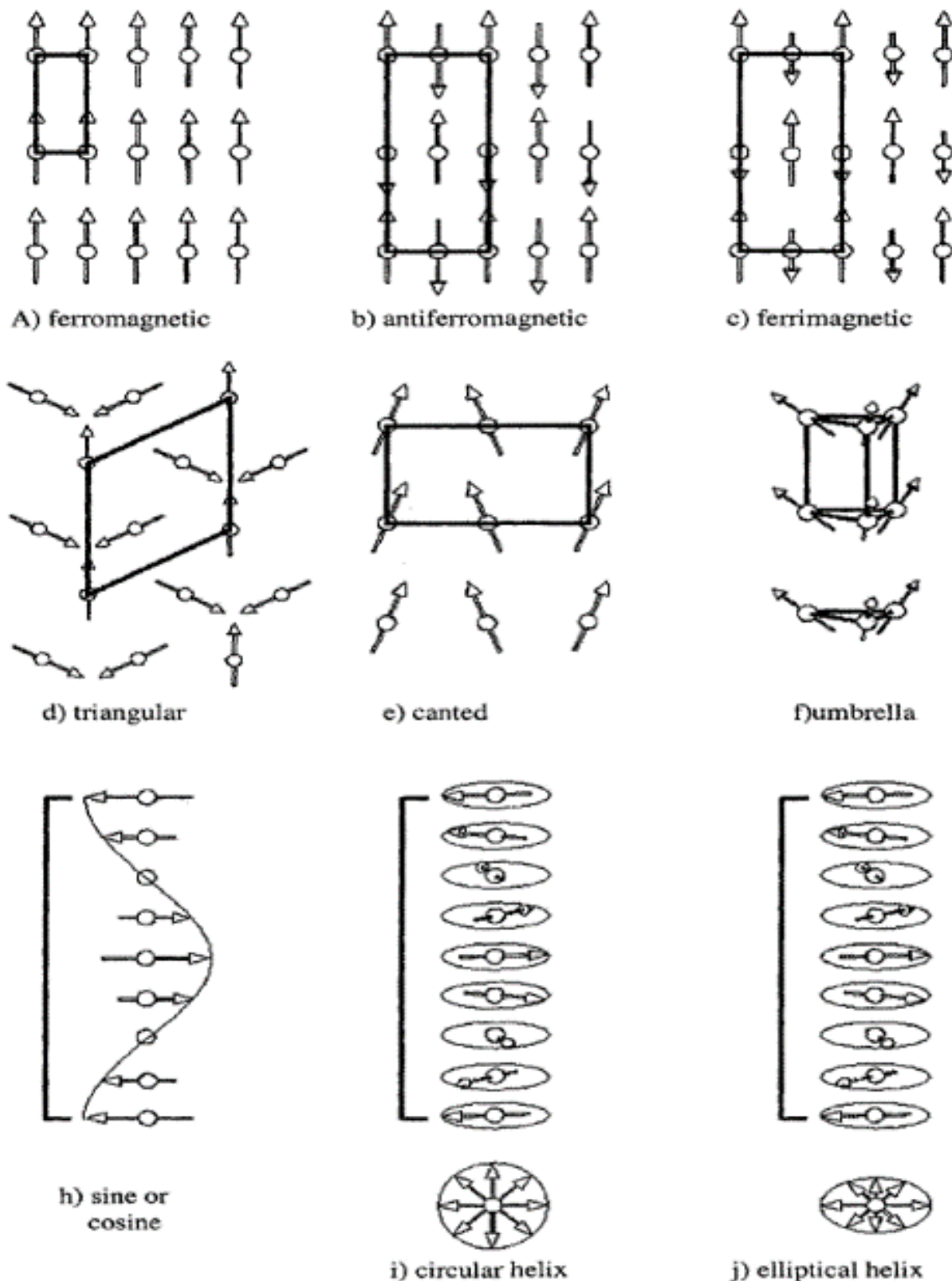


Figure 4.5: Electronic band structure

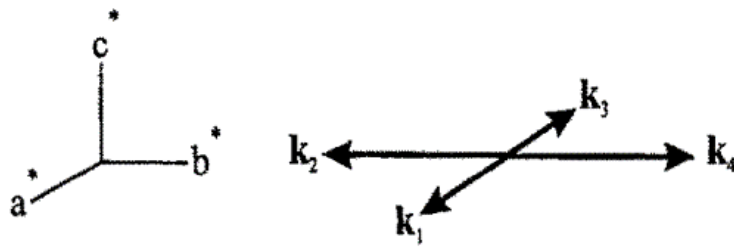


Figure 4.6: Electronic band structure

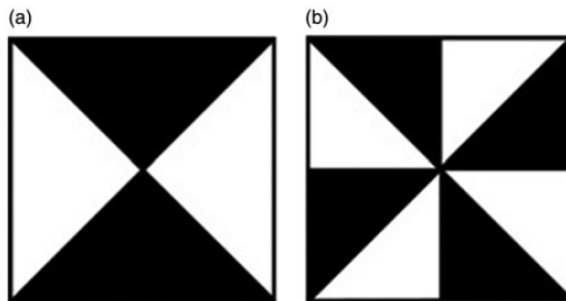


Figure 4.7: Electronic band structure

439 placerat pede. Vivamus nunc nunc, molestie ut, ultricies vel, semper in, velit. Ut porttitor.
440 Praesent in sapien. Lorem ipsum dolor sit amet, consectetuer adipiscing elit. Duis fringilla
441 tristique neque. Sed interdum libero ut metus. Pellentesque placerat. Nam rutrum augue
442 a leo. Morbi sed elit sit amet ante lobortis sollicitudin. Praesent blandit blandit mauris.
443 Praesent lectus tellus, aliquet aliquam, luctus a, egestas a, turpis. Mauris lacinia lorem sit
444 amet ipsum. Nunc quis urna dictum turpis accumsan semper.
455 Lorem ipsum dolor sit amet, consectetuer adipiscing elit. Etiam lobortis facilisis sem.
446 Nullam nec mi et neque pharetra sollicitudin. Praesent imperdiet mi nec ante. Donec
447 ullamcorper, felis non sodales commodo, lectus velit ultrices augue, a dignissim nibh lectus
448 placerat pede. Vivamus nunc nunc, molestie ut, ultricies vel, semper in, velit. Ut porttitor.
449 Praesent in sapien. Lorem ipsum dolor sit amet, consectetuer adipiscing elit. Duis fringilla
450 tristique neque. Sed interdum libero ut metus. Pellentesque placerat. Nam rutrum augue
451 a leo. Morbi sed elit sit amet ante lobortis sollicitudin. Praesent blandit blandit mauris.
452 Praesent lectus tellus, aliquet aliquam, luctus a, egestas a, turpis. Mauris lacinia lorem sit
453 amet ipsum. Nunc quis urna dictum turpis accumsan semper.
454 Lorem ipsum dolor sit amet, consectetuer adipiscing elit. Etiam lobortis facilisis sem.
455 Nullam nec mi et neque pharetra sollicitudin. Praesent imperdiet mi nec ante. Donec
456 ullamcorper, felis non sodales commodo, lectus velit ultrices augue, a dignissim nibh lectus
457 placerat pede. Vivamus nunc nunc, molestie ut, ultricies vel, semper in, velit. Ut porttitor.

458 Praesent in sapien. Lorem ipsum dolor sit amet, consectetuer adipiscing elit. Duis fringilla
459 tristique neque. Sed interdum libero ut metus. Pellentesque placerat. Nam rutrum augue
460 a leo. Morbi sed elit sit amet ante lobortis sollicitudin. Praesent blandit blandit mauris.
461 Praesent lectus tellus, aliquet aliquam, luctus a, egestas a, turpis. Mauris lacinia lorem sit
462 amet ipsum. Nunc quis urna dictum turpis accumsan semper.

Chapter 5

An in-plane hexagonal antiferromagnet in the Cu-Mn-As system, Cu_{0.82}Mn_{1.18}As

463 Copyright statement

464 5.1 Introduction

465 Recent demonstrations on electronic switching of domains in semimetallic tetragonal CuM-
466 nAs have attracted considerable interest in the field of antiferromagnetic (AF) spintron-
467 ics. [4, 13, 45, 46] Thin films of tetragonal CuMnAs grown on GaP (001) substrates have a
468 Néel temperature T_N of about 480 K. [19, 20] These studies are complicated by the variable
469 allowed stoichiometries of phases in the Cu–Mn–As system. Before any domain-switching
470 studies were demonstrated, bulk tetragonal CuMnAs was shown to be stabilized by the
471 addition of excess nominal Cu in solid-state reactions. [18] A large variation in the Néel tem-
472 perature T_N from 507 K to 320 K has been shown as Cu excess in Cu_{1+x}Mn_{1-x}As increases
473 from $x = 0.02$ to 1.4, [42] and a weak ferromagnetic transition around 300 K was reported
474 around $x = 0$. [15] On the Mn excess side, orthorhombic CuMn₃As₂ is formed as a stable
475 phase. [18]

476 When Cu, Mn, and As are mixed stoichiometrically, CuMnAs crystallizes in an orthorhom-
477 bic *Pnma* phase [16]. Orthorhombic CuMnAs is the first compound to have been proposed
478 as a magnetically-ordered Dirac semimetal [47] and has been discussed for the possibility of
479 voltage-induced switching [14]. Initial characterization by Máca *et al.* showed $T_N = 360$ K
480 as judged by resistivity and differential thermal analysis. [16] This commensurate magnetic
481 ordering and T_N in orthorhombic CuMnAs was confirmed by Emmanouilidou *et al.*, who
482 also found that a slightly cation deficient tetragonal sample Cu_{0.98}Mn_{0.96}As exhibits an incom-
483 mensurate AF ordering at 320 K, followed by another AF reorientation around 230 K. [48]

484 All known ternary phases in the Cu–Mn–As system have the transition metal (M) to As
485 ratio of 2:1 and are either tetragonal or orthorhombic as shown in Fig. 5.1. The metallic nature
486 of these compounds allows significant deviation from M₂As stoichiometry, as evidenced by
487 the binary compounds MnAs (a ferromagnet with a reentrant FeP-to-NiAs-type transition),
488 [49–51] Mn₃As₂ (which has at least three polymorphs), [52–54] the seemingly metastable
489 compounds Mn₄As₃ and Mn₅As₄, [53, 55] and Mn₃As. [56] Of these compounds, only MnAs
490 and Mn₂As have been investigated with neutron diffraction and transport measurements. [41,

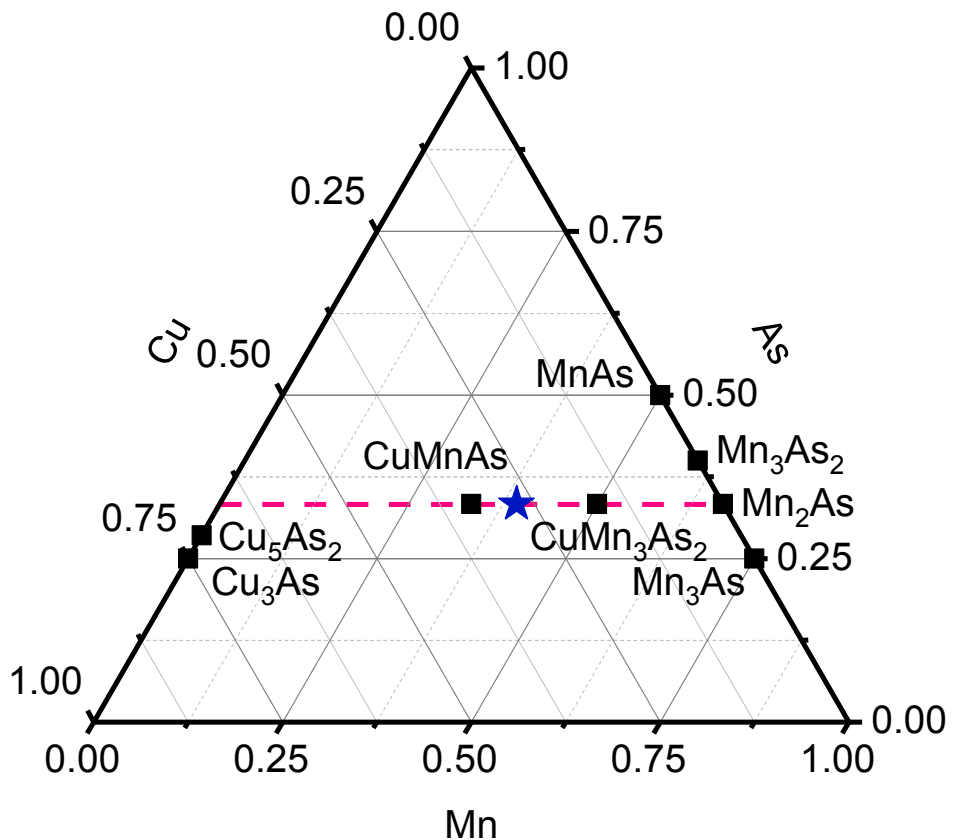


Figure 5.1: (Color online.) Hexagonal $\text{Cu}_{0.82}\text{Mn}_{1.18}\text{As}$ has been marked with a star among the previously-known phases in the Cu–Mn–As system. Compositions near CuMnAs are known to crystallize in both tetragonal and orthorhombic crystal systems.

491 57] Further elaboration of compounds in this space is necessary to understand the potential
492 for manipulating spins in these highly-correlated phases.

493 5.2 Methods

494 Millimeter-sized crystals of hexagonal Cu_{0.82}Mn_{1.18}As were synthesized by mixing elemental
495 powders Cu (99.9% metals basis), Mn (99.98% metals basis), and As (99.9999% metals basis)
496 in 0.82:1.18:1 molar ratio. The powders were vacuum sealed in quartz tubes and heated at
497 1°C/min to 600°C for 6 hours then ramped at 1°C/min to 975°C for 1 hour. The tube was
498 slow cooled at 1°C/min to 900°C and held for 1 hour before furnace-cooling down to room
499 temperature. The resulting product was a solid ingot. The ingot was crushed into smaller
500 pieces to conduct single crystal X-ray diffraction on a Bruker X8 Apex II diffractometer at
501 296 K and $\lambda = 0.71073 \text{ \AA}$.

502 Variable-temperature powder X-ray diffraction was performed using a nitrogen blower
503 at beamline 11-BM of the Advanced Photon Source in Argonne National Laboratory ($\lambda =$
504 0.4128 Å). [58] Variable-temperature neutron powder diffraction was conducted at the WAND²
505 instrument at the High-Flux Isotope Reactor (HFIR) at Oak Ridge National Laboratory. [59]

506 Magnetic structure determination was performed on a 2 mm crystal at the HB-3A four
507 circle diffractometer at HFIR. A total of 344 reflections were collected at 4 K and used for
508 structural refinement. Magnetic symmetry analysis was carried out using the tools available
509 at the Bilbao Crystallographic Server [60] and refined using the FullProf suite. [61]

510 Differential scanning calorimetry (DSC) measurements were performed on 5 mg of powder
511 in Al pans under N₂ atmosphere in a TA Instruments DSC 2500. A small fractured sample,
512 weighing about 12 mg, was polished and aligned using Laue diffraction. This sample was
513 mounted onto a quartz paddle sample holder for aligned magnetometry measurements in
514 a Quantum Design MPMS3. Aligned resistivity measurements were carried out using the
515 4-point probe method in a Quantum Design PPMS DynaCool.

516 First-principles density functional theory (DFT) simulations were performed using the
517 Vienna *Ab-Initio* Simulation Package (VASP) [62, 63]. The electron-ion interaction is de-
518 scribed using the projector-augmented wave (PAW) scheme. [64] Exchange and correlation
519 are described using the generalized-gradient approximation (GGA) by Perdew, Burke, and
520 Ernzerhof (PBE). [65] Single-particle Kohn-Sham states are expanded into a plane-wave basis
521 with a cutoff energy of 600 eV. Monkhorst-Pack [66] (MP) \mathbf{k} -point grids of $2 \times 2 \times 6$ and
522 $4 \times 4 \times 12$ are used to integrate the Brillouin zone for cell relaxation and electronic band
523 structure calculations, respectively. Non-collinear magnetism and spin-orbit coupling is taken
524 into account in all calculations [67]. Self-consistent total-energy convergence was achieved
525 to within 10^{-6} eV and atomic positions were relaxed until Hellman-Feynman forces were
526 smaller than 5 meV/Å.

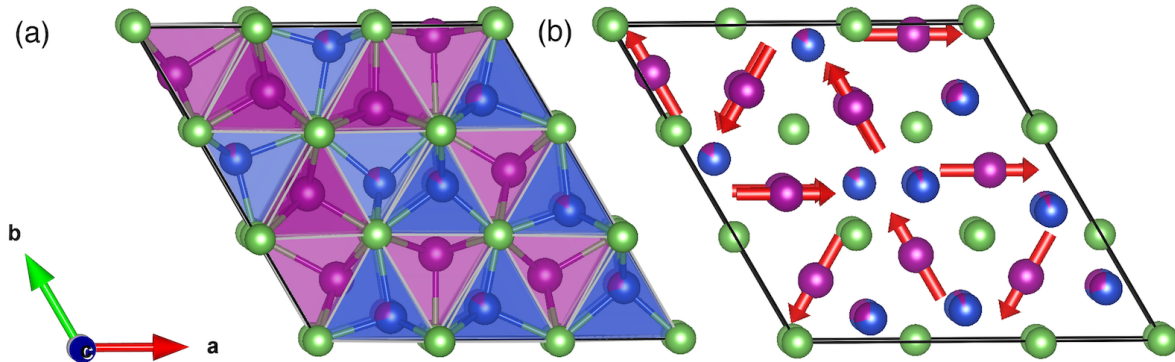


Figure 5.2: (Color online.) Unit cell of Cu_{0.82}Mn_{1.18}As (a) is shown with square pyramidal Mn in purple, tetrahedrally coordinated Cu in blue, and As in green. In (b), the refined magnetic structure is shown with moments on the Mn sites.

5.3 Results and Discussion

5.3.1 Structure refinement

The refined structure of Cu_{0.82}Mn_{1.18}As is shown in Fig. 5.2(a), with structural parameters from single-crystal X-ray diffraction (XRD) given in Table 5.1 and 5.2. Cu_{0.82}Mn_{1.18}As has a short lattice parameter $c \approx 3.8$ Å, indicating that the unit cell is flat and is the same width as the Cu and Mn coordination polyhedra. Fig. 5.2(a) shows the unit cell viewed down c , with all the atoms occupying either $z = 0$ or $z = 0.5$. The compound forms in a new structure type with space group $P\bar{6}$, and is comprised of three inequivalent square-pyramidal Mn and three inequivalent tetrahedral Cu, all coordinated by As. All metal sites have a multiplicity of 3 and have m point symmetry. The atomic positions are well-described by the single-crystal XRD data, but the occupancies are less reliable due to the similar electron densities at each site. High-resolution synchrotron powder X-ray diffraction is shown in Fig. 5.3(a), to confirm that these samples can be made highly pure with excellent crystallinity.

The occupancies are better constrained by neutron scattering, where Mn and Cu have more contrast in their scattering lengths (-3.73 and 7.718 fm, respectively). [68] Neutron powder diffraction data from WAND² were collected at 400 K, in the paramagnetic regime, with the refinement shown in Fig. 5.3(b). No evidence for site mixing or vacancies on the Mn or As sites was apparent. The best refinements were obtained by using the nominal Cu/Mn ratio and allowing Mn mixing on the Cu sites, with the final Cu occupancies of $0.709(2)$, $0.914(3)$, and $0.846(2)$ for Cu sites 1–3, respectively. The final structural refinement data presented in Table 5.2 is a single-crystal XRD refinement with the occupancies locked to values obtained by co-refinement to the 100 K synchrotron X-ray and 400 K neutron scattering data.

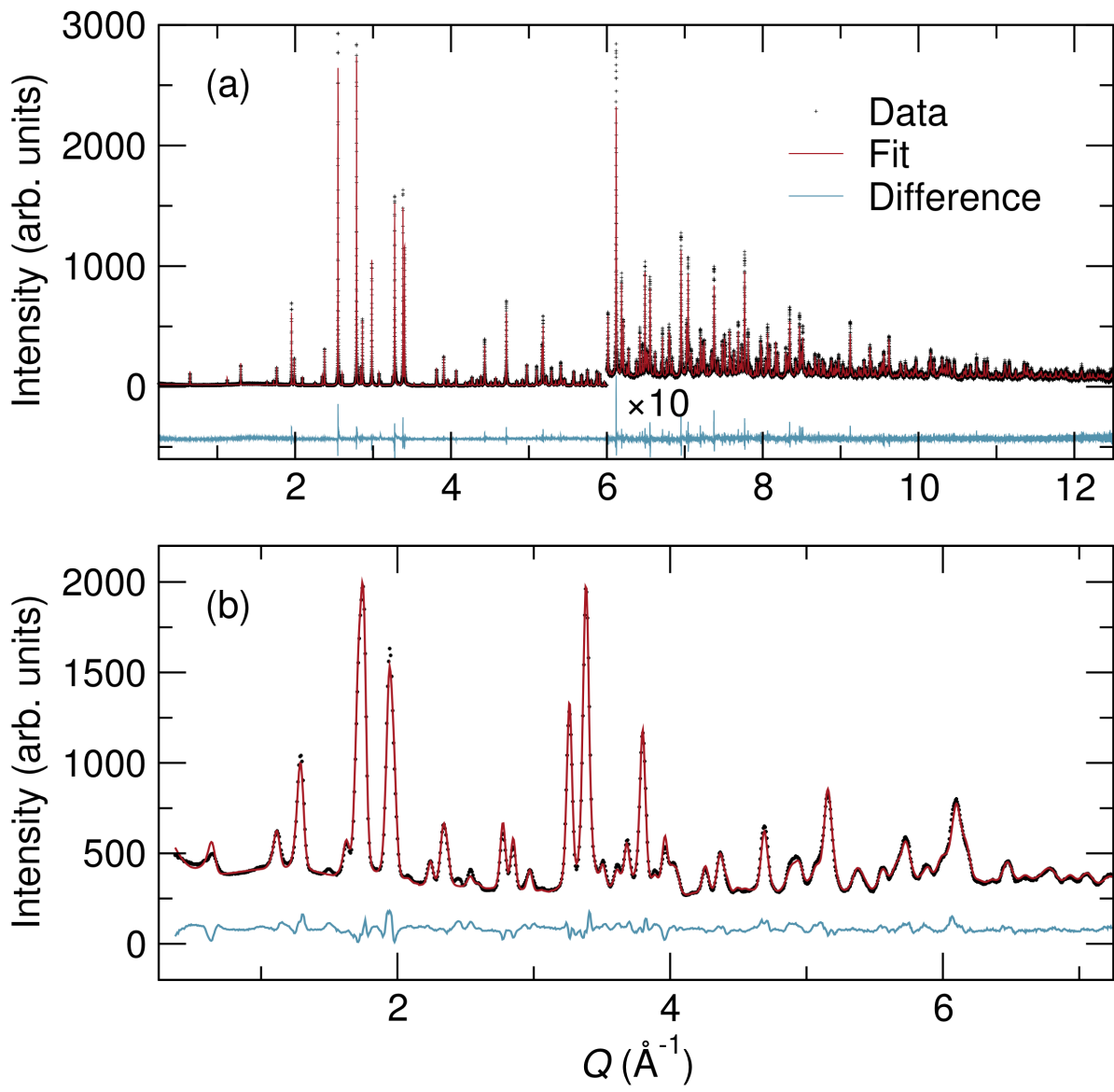


Figure 5.3: (Color online.) Refinements of Cu_{0.82}Mn_{1.18}As to (a) synchrotron X-ray powder diffraction at 100 K at APS 11-BM ($\lambda = 0.4128 \text{ \AA}$) and (b) neutron powder diffraction at 400 K on WAND² ($\lambda = 1.487 \text{ \AA}$).

Table 5.1: Structural parameters obtained from room-temperature Mo- $K\alpha$ X-ray single-crystal refinement (full-matrix least-squares on F^2) with occupancies fixed from synchrotron X-ray and neutron co-refinement.

Formula	$\text{Cu}_{0.82}\text{Mn}_{1.18}\text{As}$
Formula Weight	191.88 g/mol
Crystal system	Hexagonal
Space group	$P\bar{6}$
$a = b$	11.1418(3) Å
c	3.8311(2) Å
V, Z	411.87(3) Å ³ , 9
ρ	6.962 g/cm ³
Absorption coefficient	35.046 mm ⁻¹
$F(000)$	777
$(\sin \theta / \lambda)_{max}$	0.714
Reflections collected	6722
Observed $I > 2\sigma(I)$ reflections	953
R_{int}	0.0682
Number of parameters	56
Goodness-of-fit on F^2	1.445
$R[F^2 > 2\sigma(F^2)], wR(F^2)$	0.0344, 0.0849

Table 5.2: Atomic parameters obtained from room-temperature X-ray single-crystal refinement of $\text{Cu}_{0.82}\text{Mn}_{1.18}\text{As}$. Occupancy values for Cu/Mn sites are co-refined to 100 K synchrotron and 400 K neutron powder diffraction data (see Fig. 5.3). Atomic displacement parameters U_{ij} are given in units of \AA^2 .

Atom	Site	x	y	z	Occupancy	U_{11}	U_{22}	U_{33}	U_{44}
Cu1/Mn1	3j	0.2489(9)	0.0868(10)	0	0.709/0.291(2)	0.025(3)	0.023(4)	0.030(3)	0.011(2)
Cu2/Mn2	3j	0.5894(9)	0.5043(5)	0	0.914/0.086(3)	0.012(3)	0.011(2)	0.015(2)	0.011(2)
Cu3/Mn3	3k	0.4206(9)	0.5030(6)	0.5	0.846/0.154(2)	0.016(3)	0.012(3)	0.018(3)	0.011(2)
Mn4	3j	0.1966(10)	0.4682(10)	0	1	0.016(4)	0.017(4)	0.009(3)	0.011(2)
Mn5	3k	0.8051(10)	0.9422(7)	0.5	1	0.015(3)	0.017(2)	0.017(3)	0.011(2)
Mn6	3k	0.8056(10)	0.5310(10)	0.5	1	0.009(3)	0.013(3)	0.011(3)	0.011(2)
As1	3j	0.3310(6)	0.3354(6)	0	1	0.010(2)	0.008(3)	0.013(3)	0.011(2)
As2	3k	0.6754(6)	0.6721(6)	0.5	1	0.010(2)	0.013(3)	0.0073(14)	0.011(2)
As3	1a	0	0	0	1	0.011(2)	0.011(2)	0.007(4)	0.011(2)
As4	1d	1/3	2/3	0.5	1	0.007(2)	0.007(2)	0.012(4)	0.011(2)
As5	1e	2/3	1/3	0	1	0.009(3)	0.009(3)	0.002(4)	0.011(2)

549 5.3.2 Magnetic ordering

550 In light of the strong exchange coupling in transition-metal arsenides that leads to high Curie
 551 and Néel temperatures in MnAs and Mn_2As , it is surprising that few hexagonal arsenides
 552 have been shown to order magnetically near room temperature. The most well-known
 553 structure type is the $P6_3/mmc$ NiAs-type, of which MnAs is a member. NiAs itself is a Pauli
 554 paramagnet, [69] while hexagonal CrNiAs has a Curie temperature of 190 K. [70]

555 Powders of $\text{Cu}_{0.82}\text{Mn}_{1.18}\text{As}$ were examined by DSC, with the heating and cooling traces
 556 shown in Fig. 5.4(a). There is a clear change in slope around 267 K, with a hysteresis of about
 557 4 K. To determine the origin of this transition, aligned single crystals of $\text{Cu}_{0.82}\text{Mn}_{1.18}\text{As}$ were
 558 examined via SQUID magnetometry, and the moment versus temperature is shown in Fig.
 559 5.4(b). The maximum in the magnetometry data is around 275 K for zero-field-cooled (ZFC)
 560 and field-cooled (FC) data along the a and c axes for 10 kOe applied field. There are not
 561 sufficient data above T_N to provide a satisfactory Curie-Weiss fit. The data along the c axis
 562 display a typical decrease upon cooling past T_N , while the data measured along the a axis
 563 show a slight rise and plateau around 100 K. There were no features in measurements of
 564 magnetic moment versus field to indicate spin-flop transitions or any hysteresis. The small
 565 plateau could arise from decreasing itineracy and a leveling-off of the local moments on Mn
 566 sites, which would be consistent with the single-crystal neutron magnetic intensity remaining
 567 constant below 100 K. Fig. 5.4(b) shows that for temperatures beyond 150 K, the susceptibility

568 along c is larger than along a . This trend is consistent with in-plane moments in triangular
 569 antiferromagnets such as CsMnBr_3 , CsVCl_3 , Mn_3Sn etc. [71–74] Below 150 K, the difference
 570 in the susceptibility along a and c is unclear. However, the in-plane Mn spin ordering was
 571 confirmed using neutron diffraction as shown below.

572 The magnetic ordering was probed first by variable-temperature neutron powder diffrac-
 573 tion on the WAND² instrument, which showed changes in peak intensities across this bound-
 574 ary, but no new peaks, indicating likely $k = 0$ ordering. A full triple-axis data collection was
 575 performed on the HB-3A beamline at 4 K. The magnetic and nuclear structures were refined
 576 together in the $P\bar{6}'$ magnetic space group. The intensity of the (020) peak can serve as an
 577 order parameter, and its temperature dependence is shown in Fig. 5.5(a). The (020) peak
 578 is an allowed nuclear reflection, so the intensity does not go to zero above T_N . The three
 579 inequivalent Mn sites are constrained to have equal magnetic moments, which are refined to
 580 $3.02(8) \mu_B/\text{atom}$. No improvement in the fit was observed when the moments were allowed
 581 to freely vary. The observed and calculated structure factors F_{hkl}^2 are plotted in Fig. 5.5(b).
 582 The magnetic structure is shown in Fig. 5.2(b). No local Mn moment was stably refined on
 583 the Cu-majority sites, and Cu itself does not host local moments in arsenides [75–77]. It is
 584 possible that some local Mn moments exist on the minority Cu sites, but they do not appear
 585 to be ordered. The 120° spin structure differs from Mn_3Sn . In Mn_3Sn , the spin triangles
 586 are connected by their corners. We also do not observe the “inverse triangle” orthorhombic
 587 configuration seen in Mn_3Sn . [71] There are three different types of 120° spin structures ob-
 588 served in our compound, although the spin directions in the ab plane could not be uniquely
 589 determined by unpolarized neutron diffraction. This compound could be written as contain-
 590 ing Cu^+ and Mn^{2+} , but like other transition-metal arsenides the local moment is reduced
 591 due to metallicity. [49,78]

592 Four-point probe resistivity measurements along [001] show a mostly flat, weakly undulat-
 593 ing trend versus temperature as shown in Fig. 5.6(a). The broad hump between 50 K to 250 K
 594 could be attributed to competing mobilities and carrier concentrations of multiple excited
 595 states in a heavily doped semiconductor (as in P-doped Si), [79] or variations in the dominant
 596 carrier scatterers in a disordered metal (which we discuss subsequently to be more likely,
 597 given the computed band structure). The resistivity values are roughly 125 times higher at
 598 5 K in $\text{Cu}_{0.82}\text{Mn}_{1.18}\text{As}$ than Fe_2As and about 380 times higher than tetragonal CuMnAs , both
 599 of which are metallic [17,80]. Application of a magnetic field of 10 kOe along [100] resulted
 600 in negligible change in resistivity values, shown in Fig. 5.6(a). A slightly larger effect can
 601 be seen in the Hall effect measurements in Fig. 5.6(b). The Hall data magnifies the hump
 602 around 150 K, and crosses from negative (majority n -type) to positive (p -type) upon heating
 603 past 330 K. The material is n -type at low temperatures but as temperature is increased, more
 604 carriers are excited and the higher mobility of holes leads to compensation and switching
 605 to p -type conduction 330 K. The lack of an anomaly in the total resistivity around the Hall

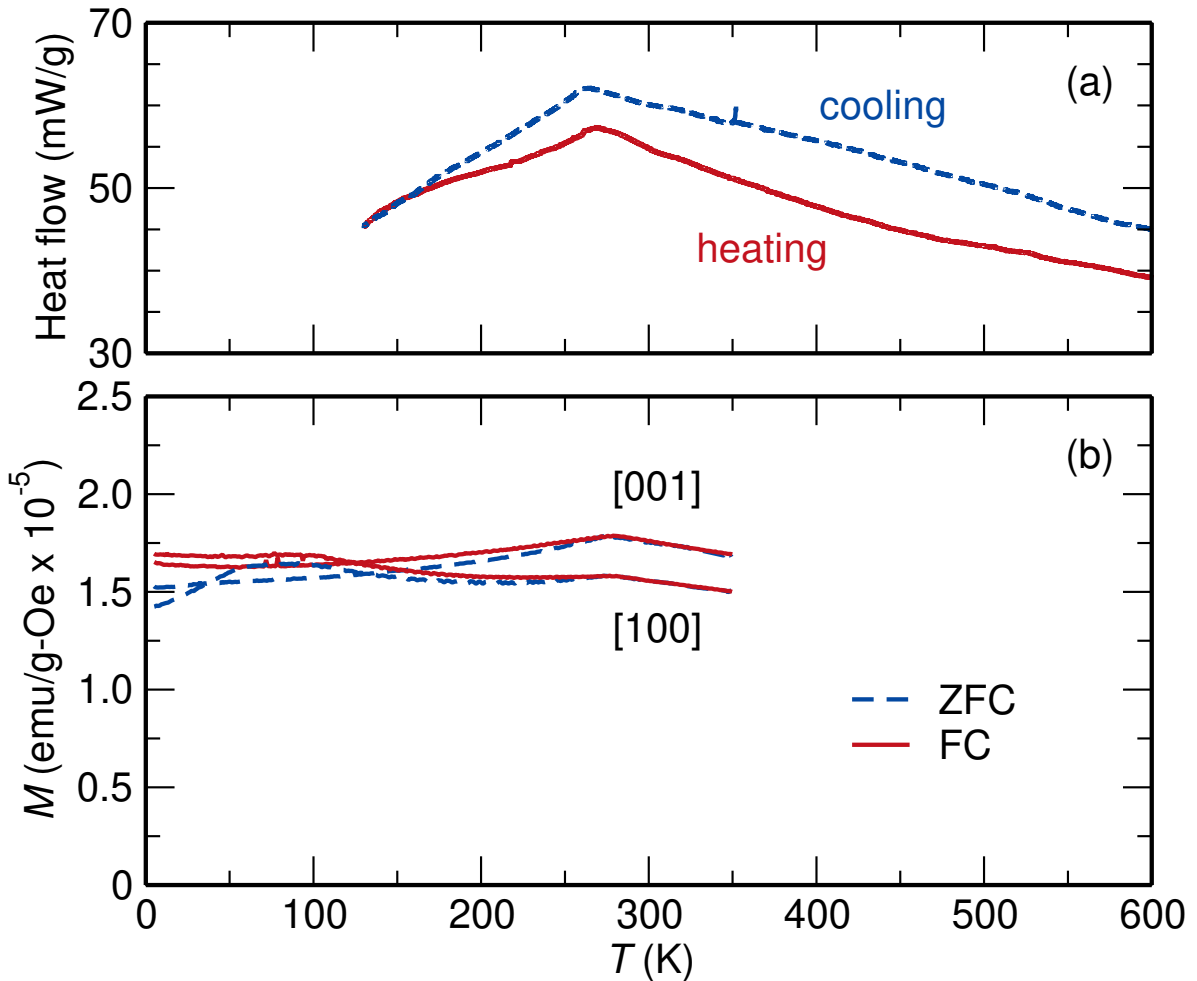


Figure 5.4: (Color online.) DSC data (a) show a clear kink in the heat flow at $T_N \approx 270$ K, indicating a discontinuous change in heat capacity of the sample. Data on heating are reflected about the x -axis. The same transition appears in magnetic susceptibility measurements (b) of an aligned single crystal, with the field axis along the [001] and [100] directions.

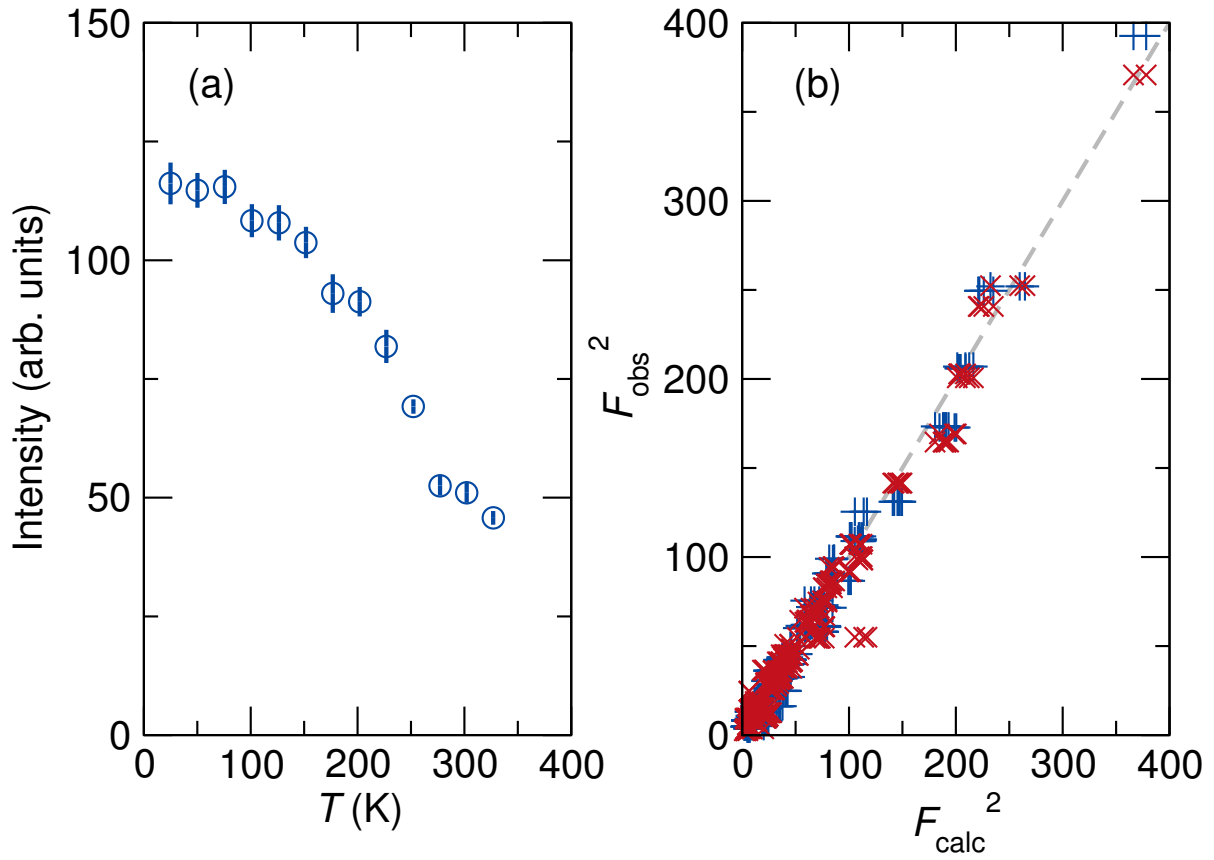


Figure 5.5: (Color online.) Measured single-crystal neutron diffraction intensity (a) of the (020) peak of $\text{Cu}_{0.82}\text{Mn}_{1.18}\text{As}$ shows a gradual increase upon cooling past T_N down to 4 K. The (020) peak is an allowed nuclear reflection and persists with constant intensity (~ 50) above T_N . The differences between observed and refined structure factors F_{hkl}^2 at $T = 4$ K are shown in (b). The triangular model obtained from neutron refinement are shown as (+) and the DFT-derived model as (x).

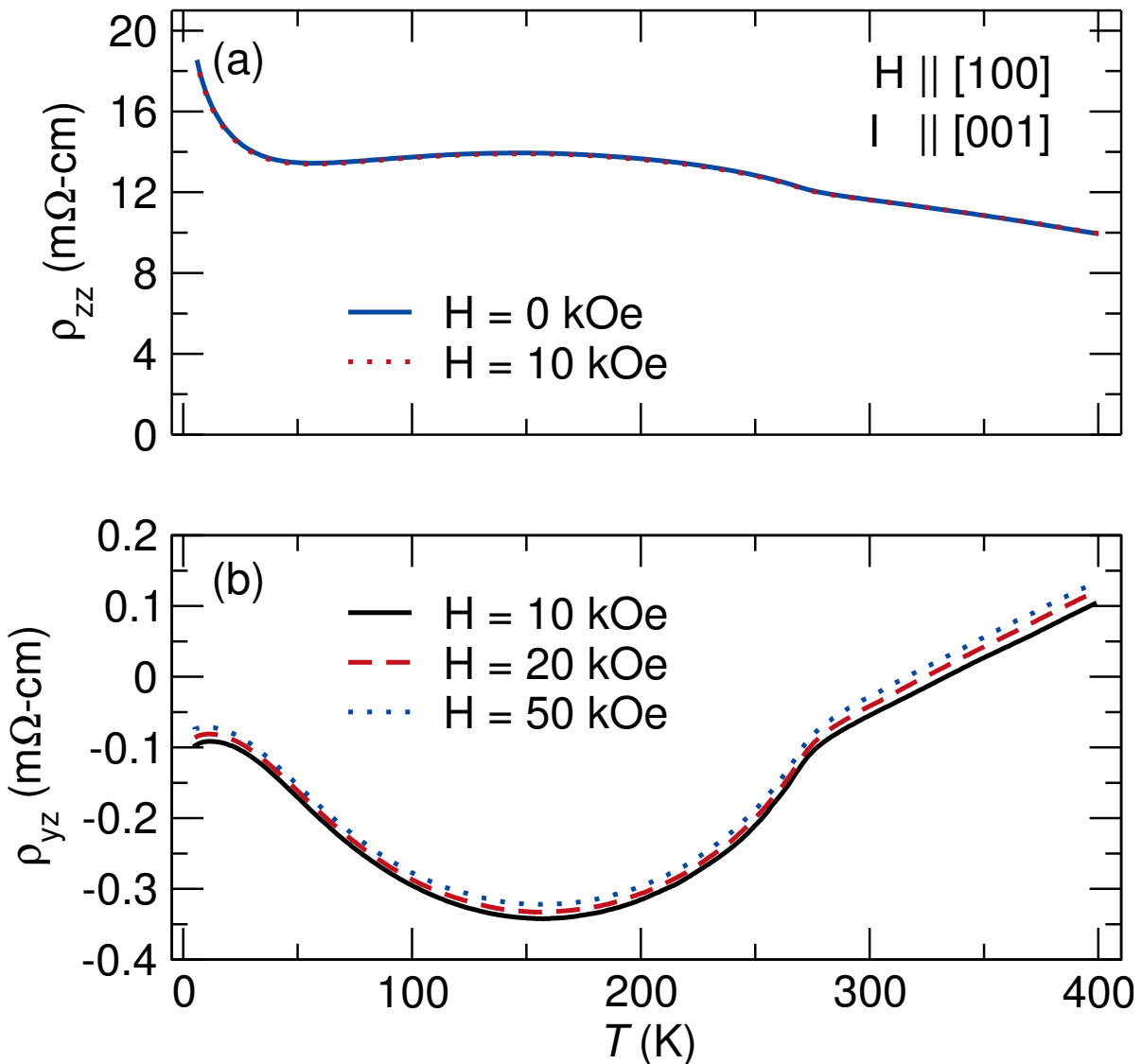


Figure 5.6: (Color online.) (a) Resistivity of Cu_{0.82}Mn_{1.18}As with applied field H along [100] and current I along [001]. The resistivity is relatively flat across the temperature range, with a small kink at $T_N = 270$ K. Hall measurements of the sample with H along [100] and current along [001] show a decreasing trend followed by an increase at higher temperatures.

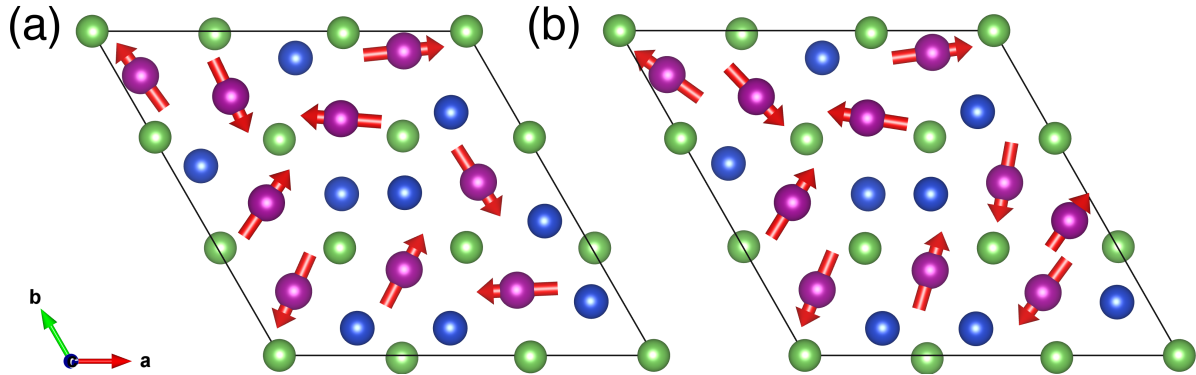


Figure 5.7: (Color online.) Structure and magnetic configuration from DFT for (a) stoichiometric hexagonal CuMnAs and (b) Cu_{0.89}Mn_{1.11}As. Mn is shown in purple, Cu in blue, and As in green.

606 crossover point indicates that the transport in Cu_{0.82}Mn_{1.18}As occurs via multiple bands, and
 607 is supported by the delicate (but not gapped) band structure around the Fermi energy that
 608 we discuss subsequently.

609 5.3.3 First-principles simulations

610 We performed first-principles density-functional theory (DFT) simulations to confirm the sta-
 611 bility, cell geometry, and magnetic ordering of a fully-occupied hexagonal model compound
 612 CuMnAs and off-stoichiometric Cu_{0.89}Mn_{1.11}As, with a single Mn on a Cu1 site (1 of the 9
 613 sites substituted per cell). We find that the relaxed atomic geometries of hexagonal CuM-
 614 nAs and Cu_{0.89}Mn_{1.11}As agree with neutron scattering results within 2 %. The DFT data for
 615 the magnetic structures arrive at different lowest-energy orderings than the neutron refine-
 616 ment. The DFT-derived lowest-energy magnetic configurations of stoichiometric CuMnAs
 617 and substituted Cu_{0.89}Mn_{1.11}As are shown in Figs. 5.7(a) and (b), respectively. The stoichio-
 618 metric result is antiferromagnetic, while the substituted site in Cu_{0.89}Mn_{1.11}As has a small
 619 uncompensated moment ($-0.102a - 0.010b \mu_B$). The calculated neutron diffraction structure
 620 factors for the stoichiometric case are compared to the single-crystal neutron-refined values
 621 in Fig. 5.5(b). The two fits are similar, apart from the trio of peaks with $F_{obs}^2 \approx 100$, which
 622 significantly degrade the fit versus the neutron result. The neutron refinement outperforms
 623 the DFT fit with $R_{F^2} = 7.77$ and $R_{F^2w} = 17.1$ versus $R_{F^2} = 7.98$ and $R_{F^2w} = 23.0$, respectively,
 624 where smaller numbers indicate a better fit. A small uncompensated moment observed in
 625 the Mn-substituted DFT model is an unavoidable artifact of the cell choice, which contains
 626 one “extra” Mn atom to reflect the off-stoichiometry of Cu_{0.82}Mn_{1.18}As.

627 Magnetic ground states in strongly-correlated *d*-electron systems are often challenging to
 628 predict using DFT, so it is instructive to quantitatively evaluate the proximity of the neutron-
 629 refined result to the DFT energy minimum, and likewise the predicted neutron intensities

Table 5.3: Energy differences (meV/atom) between different constraints in DFT (see text), and lattice parameters (Å, degree) from all-relaxed calculations of stoichiometric hexagonal CuMnAs and Cu_{0.89}Mn_{1.11}As. All phases have $\gamma = 120^\circ$.

System	$E_{\text{fix}} - E_{\text{mag}}$	$E_{\text{fix}} - E_{\text{all}}$	a	b	c
CuMnAs	9.92	15.30	11.050	11.050	3.802
Cu _{0.89} Mn _{1.11} As	6.45	14.93	11.053	11.043	3.776

of the DFT model. To better understand the energetics of this difference between theory and experiment, we compare total energies for three different situations: First, chemical and magnetic structures are constrained to the neutron scattering result (E_{fix} in Table 5.3). Second, the ground-state magnetic structure is computed from DFT while the atomic geometries are constrained to the neutron scattering data (E_{mag} in Table 5.3). Finally, these total energies are compared to the fully relaxed DFT result (E_{all} in Table 5.3). These small energy changes, 15.30 and 14.93 meV/atom for CuMnAs and Cu_{0.89}Mn_{1.11}As, respectively are typical of energy differences between various magnetic structures for similar systems. [81]

The electronic band structure and density of states of stoichiometric hexagonal CuMnAs and Cu_{0.89}Mn_{1.11}As in Fig. 5.8 show that both hexagonal models are metallic. Both electronic structures exhibit very small densities of states near the Fermi energy, similar to that described by DFT for tetragonal CuMnAs [82]. Tetragonal CuMnAs shows obvious metallic resistivity ($d\rho/dT > 0$). [17] The CuMnAs compounds are clearly on the cusp of semiconducting/metallic behavior, and share similarities to Fe₂As, which has a much greater density of states at the Fermi level and does show $d\rho/dT > 0$, but the reported values of resistivity values are much higher than that of tetragonal CuMnAs. [80,83]

Our DFT calculations suggest that Cu_{0.89}Mn_{1.11}As is metallic. However, transport measurements indicate that the resistivity is high, and $d\rho/dT < 0$ for most T . The negative slope that is observed at low and high temperatures is not exponential as is expected in highly-doped semiconductors. [79] The seeming discrepancy between resistivity and the computed band structure can be resolved by considering the high amount of substitutional disorder in these compounds. Metals often exhibit $d\rho/dT < 0$ behavior when a large amount of configurational disorder is present, [84] and the negative temperature dependence is in fact correlated with high absolute values of resistivity. [85] In our material, carriers must scatter due to pervasive disorder due to Mn site mixing, while magnon scattering may also contribute strongly, but the overall resistivity is hardly affected upon cooling past T_N .

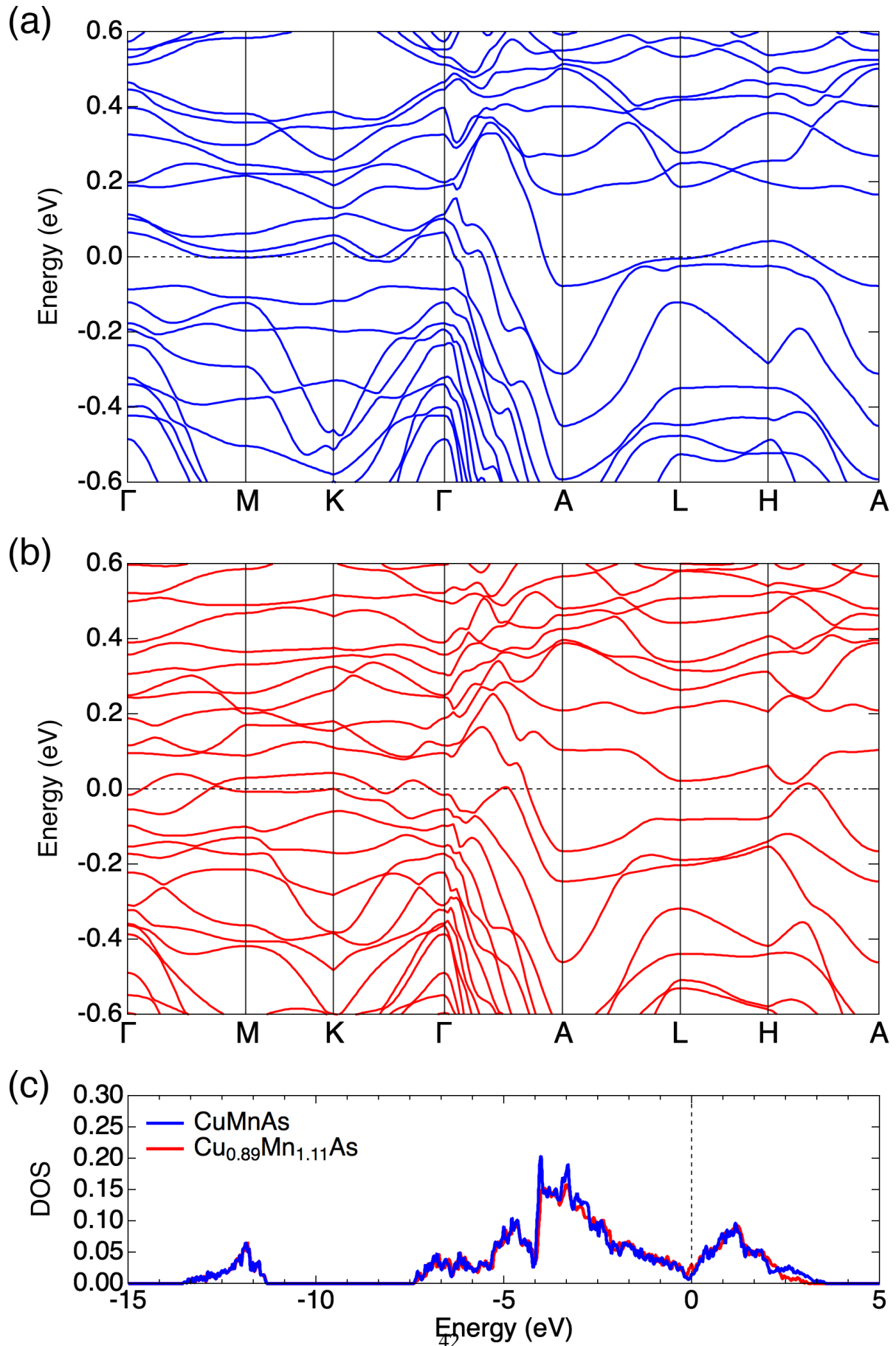


Figure 5.8: (Color online.) Electronic band structure of (a) stoichiometric hexagonal CuMnAs (blue) and (b) Cu_{0.89}Mn_{1.11}As (red). Both densities of states (DOS, in units of states per \AA^3 and per eV per spin), computed using DFT, are shown in (c). The highest-occupied energies are set as $E = 0$ eV.

656 **5.4 Conclusions**

657 We report the crystal structure of a non-centrosymmetric $P\bar{6}'$ phase in the Cu–Mn–As system,
658 with a new structure type. This compound can be made phase-pure in single crystal form.
659 Triangular antiferromagnetic ordering appears upon cooling below 270 K and is markedly
660 distinct from the orthorhombic and tetragonal CuMnAs phases, both of which are stabilized
661 by different Cu/Mn content and are centrosymmetric in their paramagnetic states. DFT
662 calculations confirm the stability of the magnetic structure refined by single-crystal neutron
663 diffraction. The triangular AF ordering is in-plane and does not break degeneracy of the
664 *a* and *b* axes. Like other copper manganese arsenides, hexagonal Cu_{0.82}Mn_{1.18}As is on the
665 cusp of semiconducting/metallic behavior and further investigation of the carrier scattering
666 mechanisms in this class of materials is warranted.

667 **5.5 Acknowledgments**

668 This work is supported by the National Science Foundation (NSF) under Grant No. DMR-
669 1720633. Characterization was carried out in part in the Materials Research Laboratory
670 Central Research Facilities, University of Illinois. Use of the Advanced Photon Source at
671 Argonne National Laboratory was supported by the U.S. Department of Energy, Office of
672 Science, Office of Basic Energy Sciences, under Contract No. DE-AC02-06CH11357. Neutron
673 scattering was performed at the High Flux Isotope Reactor, a Department of Energy Office
674 of Science User Facility operated by the Oak Ridge National Laboratory. This work made
675 use of the Illinois Campus Cluster, a computing resource that is operated by the Illinois
676 Campus Cluster Program (ICCP) in conjunction with the National Center for Supercomputing
677 Applications (NCSA) and which is supported by funds from the University of Illinois at
678 Urbana-Champaign. We thank Junseok Oh for assistance in making contacts for resistivity
679 measurements.

Chapter 6

Two step magnetic ordering in monoclinic Mn₃As₂

680 Lorem ipsum dolor sit amet, consectetuer adipiscing elit. Etiam lobortis facilisis sem. Nullam
681 nec mi et neque pharetra sollicitudin. Praesent imperdiet mi nec ante. Donec ullamcorper,
682 felis non sodales commodo, lectus velit ultrices augue, a dignissim nibh lectus placerat pede.
683 Vivamus nunc nunc, molestie ut, ultricies vel, semper in, velit. Ut porttitor. Praesent in sapien.
684 Lorem ipsum dolor sit amet, consectetuer adipiscing elit. Duis fringilla tristique neque. Sed
685 interdum libero ut metus. Pellentesque placerat. Nam rutrum augue a leo. Morbi sed elit sit
686 amet ante lobortis sollicitudin. Praesent blandit blandit mauris. Praesent lectus tellus, aliquet
687 aliquam, luctus a, egestas a, turpis. Mauris lacinia lorem sit amet ipsum. Nunc quis urna
688 dictum turpis accumsan semper.

689 Lorem ipsum dolor sit amet, consectetuer adipiscing elit. Etiam lobortis facilisis sem.
690 Nullam nec mi et neque pharetra sollicitudin. Praesent imperdiet mi nec ante. Donec
691 ullamcorper, felis non sodales commodo, lectus velit ultrices augue, a dignissim nibh lectus
692 placerat pede. Vivamus nunc nunc, molestie ut, ultricies vel, semper in, velit. Ut porttitor.
693 Praesent in sapien. Lorem ipsum dolor sit amet, consectetuer adipiscing elit. Duis fringilla
694 tristique neque. Sed interdum libero ut metus. Pellentesque placerat. Nam rutrum augue
695 a leo. Morbi sed elit sit amet ante lobortis sollicitudin. Praesent blandit blandit mauris.
696 Praesent lectus tellus, aliquet aliquam, luctus a, egestas a, turpis. Mauris lacinia lorem sit
697 amet ipsum. Nunc quis urna dictum turpis accumsan semper.

698 Lorem ipsum dolor sit amet, consectetuer adipiscing elit. Etiam lobortis facilisis sem.
699 Nullam nec mi et neque pharetra sollicitudin. Praesent imperdiet mi nec ante. Donec
700 ullamcorper, felis non sodales commodo, lectus velit ultrices augue, a dignissim nibh lectus
701 placerat pede. Vivamus nunc nunc, molestie ut, ultricies vel, semper in, velit. Ut porttitor.
702 Praesent in sapien. Lorem ipsum dolor sit amet, consectetuer adipiscing elit. Duis fringilla
703 tristique neque. Sed interdum libero ut metus. Pellentesque placerat. Nam rutrum augue
704 a leo. Morbi sed elit sit amet ante lobortis sollicitudin. Praesent blandit blandit mauris.
705 Praesent lectus tellus, aliquet aliquam, luctus a, egestas a, turpis. Mauris lacinia lorem sit
706 amet ipsum. Nunc quis urna dictum turpis accumsan semper.

707 Lorem ipsum dolor sit amet, consectetuer adipiscing elit. Etiam lobortis facilisis sem.
708 Nullam nec mi et neque pharetra sollicitudin. Praesent imperdiet mi nec ante. Donec
709 ullamcorper, felis non sodales commodo, lectus velit ultrices augue, a dignissim nibh lectus

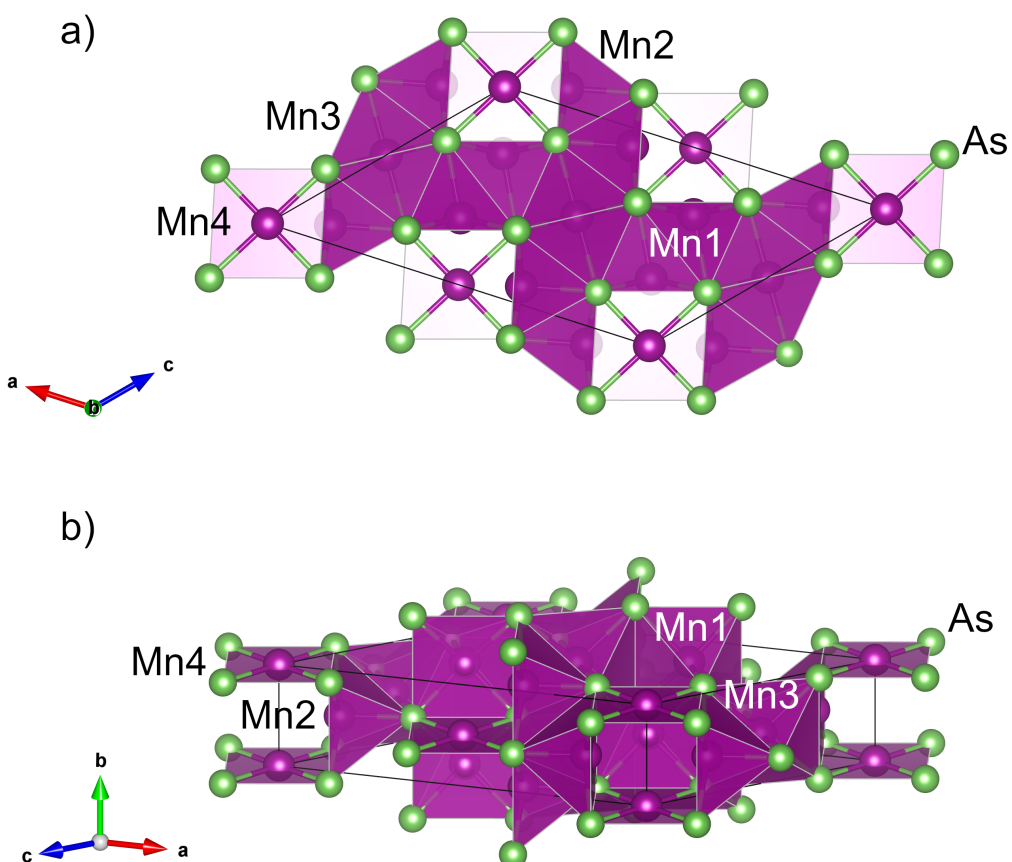


Figure 6.1: Electronic band structure

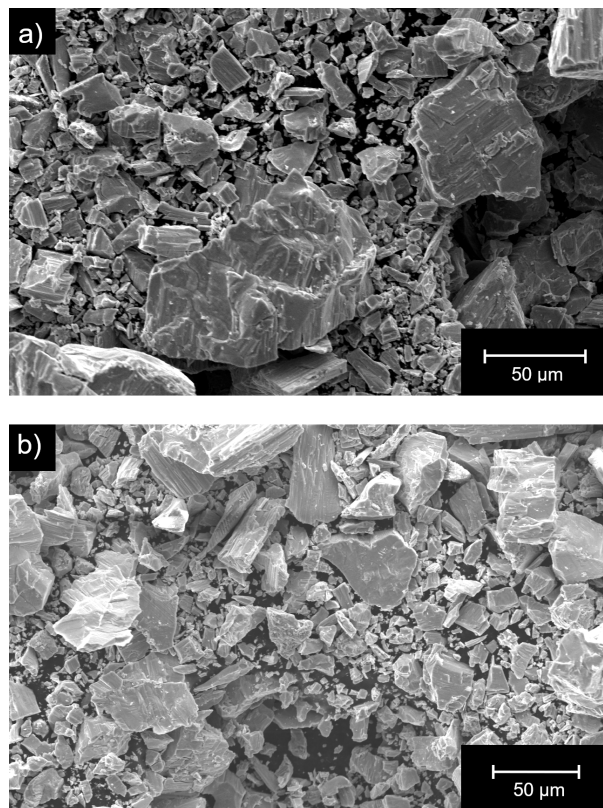


Figure 6.2: Electronic band structure

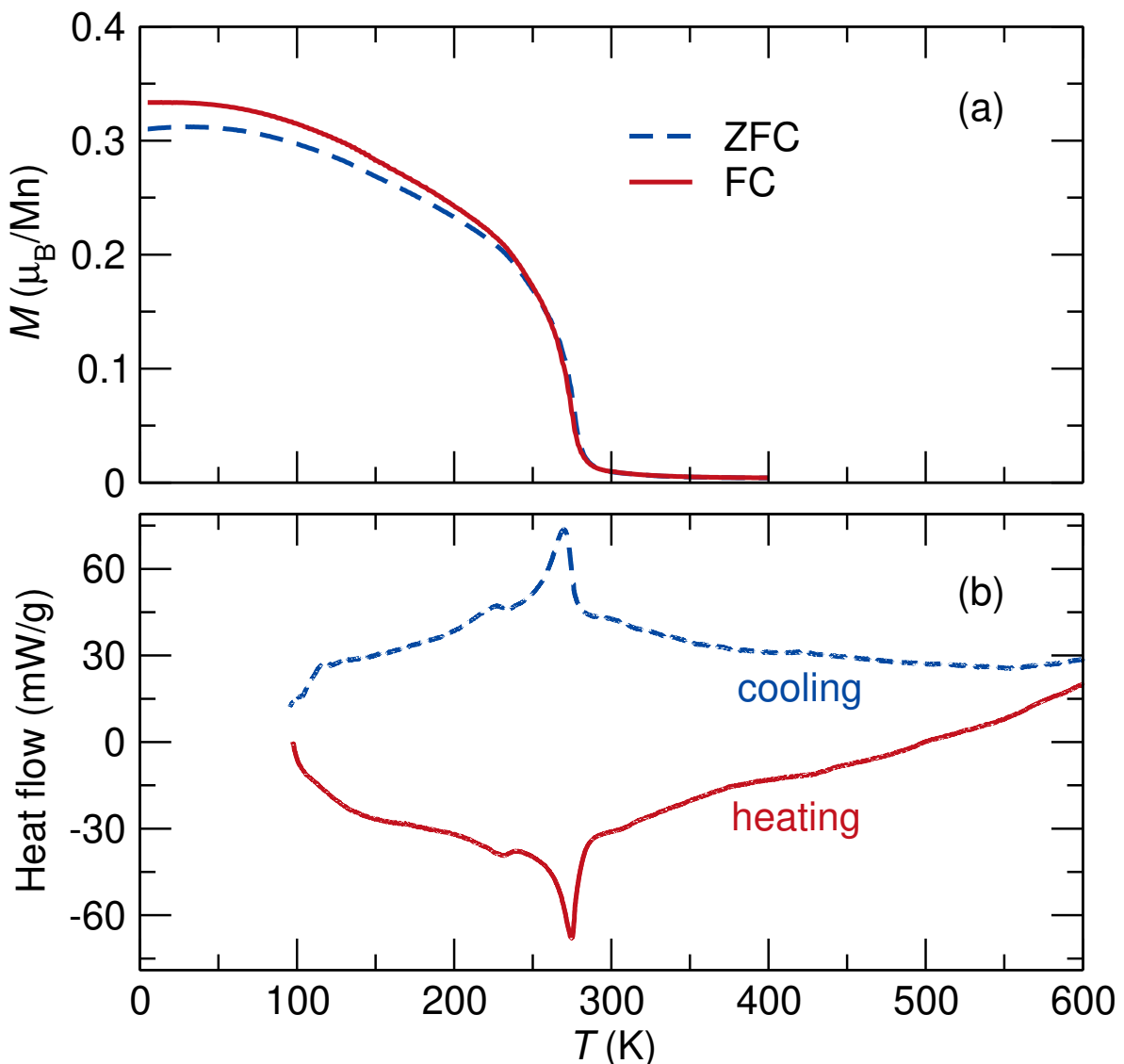


Figure 6.3: Electronic band structure

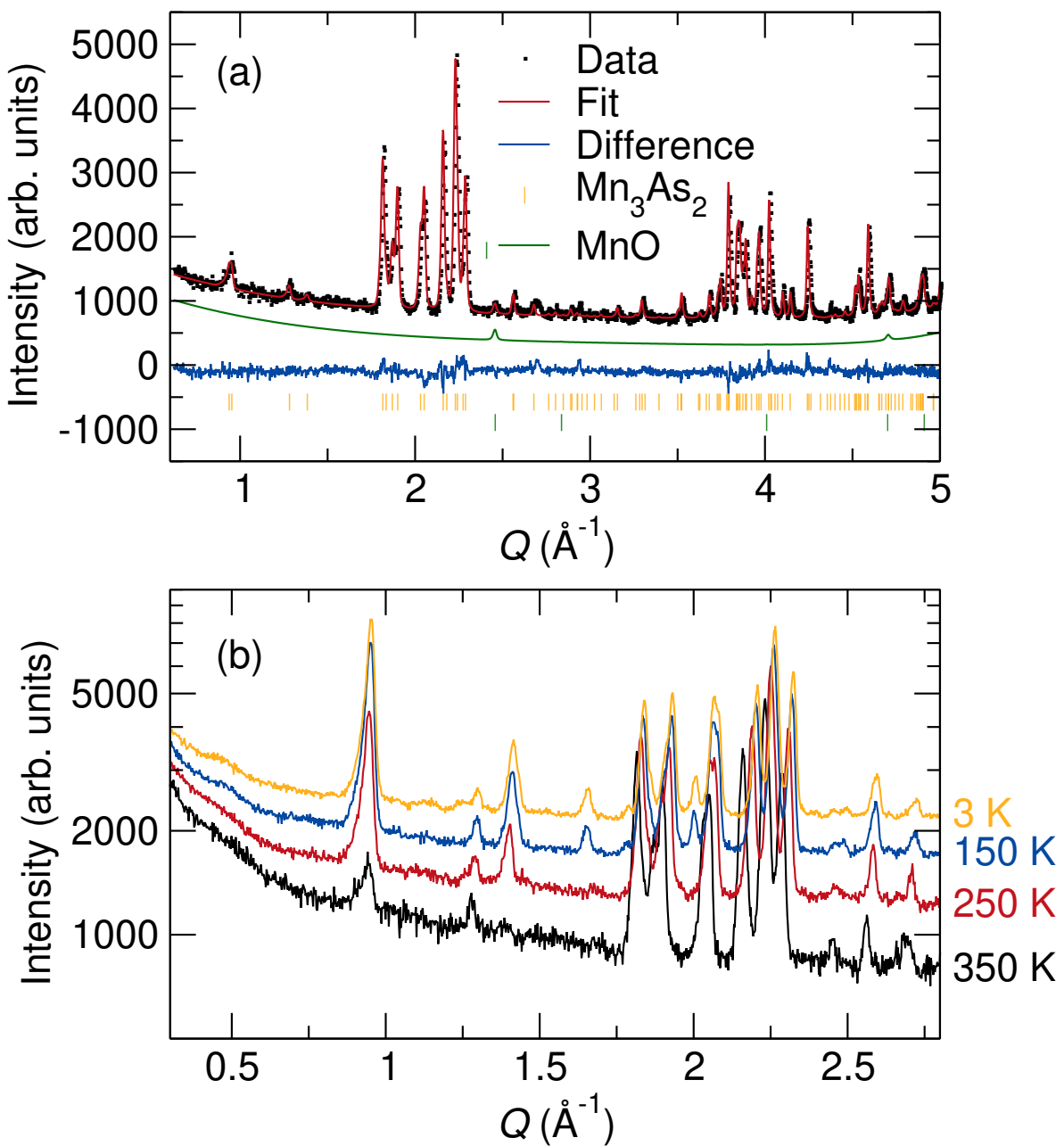


Figure 6.4: Electronic band structure

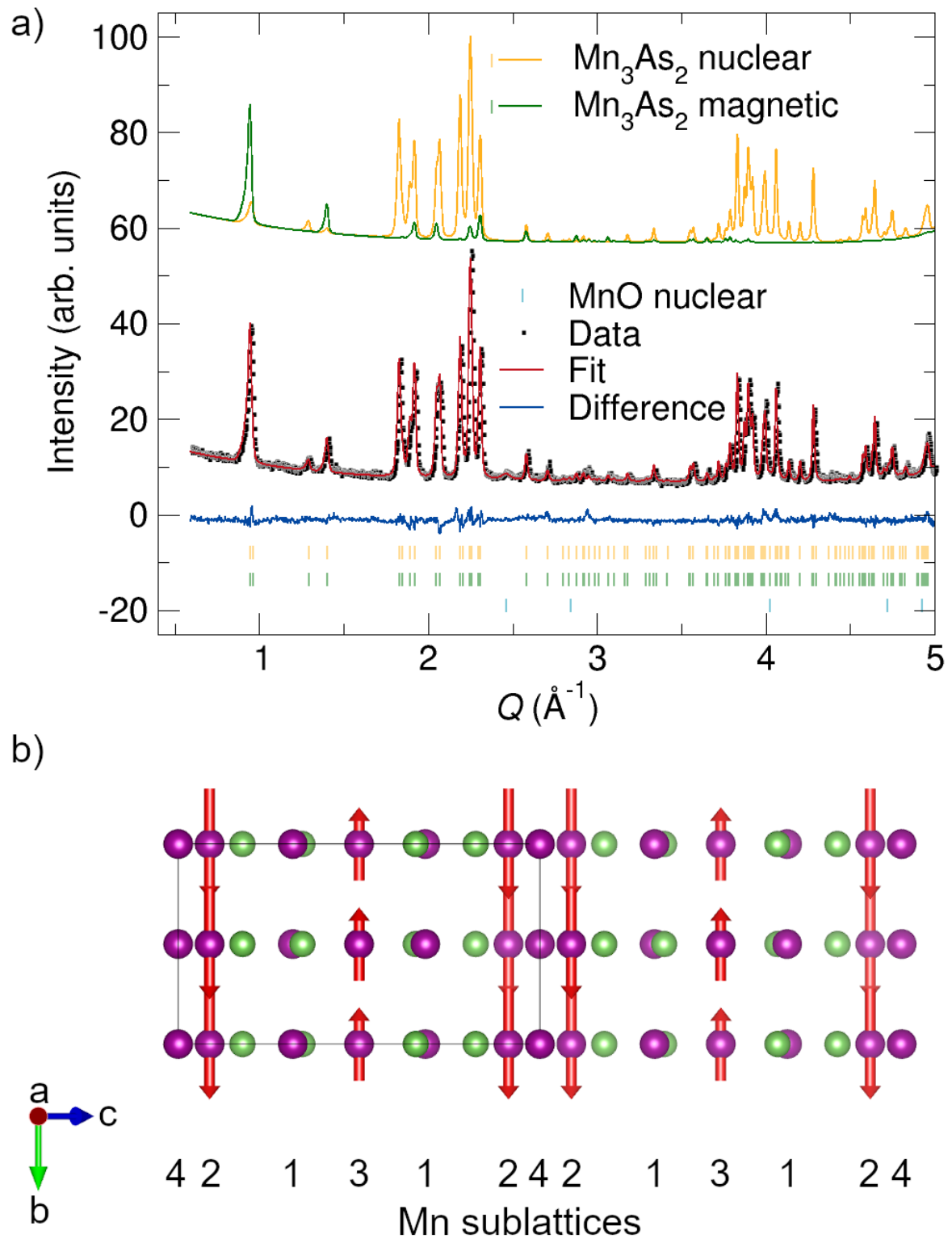


Figure 6.5: Electronic band structure

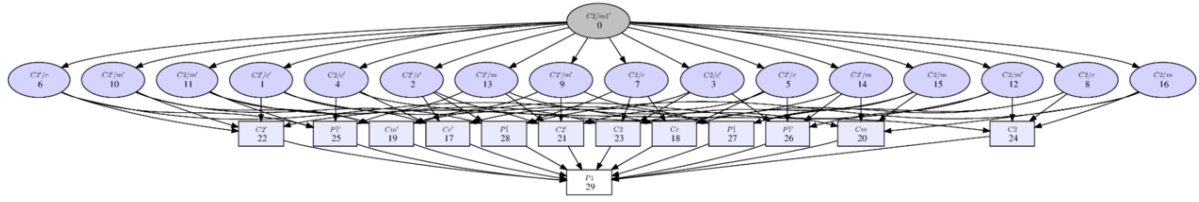


Figure 6.6: Electronic band structure

710 placerat pede. Vivamus nunc nunc, molestie ut, ultricies vel, semper in, velit. Ut porttitor.
 711 Praesent in sapien. Lorem ipsum dolor sit amet, consectetuer adipiscing elit. Duis fringilla
 712 tristique neque. Sed interdum libero ut metus. Pellentesque placerat. Nam rutrum augue
 713 a leo. Morbi sed elit sit amet ante lobortis sollicitudin. Praesent blandit blandit mauris.
 714 Praesent lectus tellus, aliquet aliquam, luctus a, egestas a, turpis. Mauris lacinia lorem sit
 715 amet ipsum. Nunc quis urna dictum turpis accumsan semper.
 716 Lorem ipsum dolor sit amet, consectetuer adipiscing elit. Etiam lobortis facilisis sem.
 717 Nullam nec mi et neque pharetra sollicitudin. Praesent imperdiet mi nec ante. Donec
 718 ullamcorper, felis non sodales commodo, lectus velit ultrices augue, a dignissim nibh lectus
 719 placerat pede. Vivamus nunc nunc, molestie ut, ultricies vel, semper in, velit. Ut porttitor.
 720 Praesent in sapien. Lorem ipsum dolor sit amet, consectetuer adipiscing elit. Duis fringilla
 721 tristique neque. Sed interdum libero ut metus. Pellentesque placerat. Nam rutrum augue
 722 a leo. Morbi sed elit sit amet ante lobortis sollicitudin. Praesent blandit blandit mauris.
 723 Praesent lectus tellus, aliquet aliquam, luctus a, egestas a, turpis. Mauris lacinia lorem sit
 724 amet ipsum. Nunc quis urna dictum turpis accumsan semper.
 725 Lorem ipsum dolor sit amet, consectetuer adipiscing elit. Etiam lobortis facilisis sem.
 726 Nullam nec mi et neque pharetra sollicitudin. Praesent imperdiet mi nec ante. Donec
 727 ullamcorper, felis non sodales commodo, lectus velit ultrices augue, a dignissim nibh lectus
 728 placerat pede. Vivamus nunc nunc, molestie ut, ultricies vel, semper in, velit. Ut porttitor.
 729 Praesent in sapien. Lorem ipsum dolor sit amet, consectetuer adipiscing elit. Duis fringilla
 730 tristique neque. Sed interdum libero ut metus. Pellentesque placerat. Nam rutrum augue
 731 a leo. Morbi sed elit sit amet ante lobortis sollicitudin. Praesent blandit blandit mauris.
 732 Praesent lectus tellus, aliquet aliquam, luctus a, egestas a, turpis. Mauris lacinia lorem sit
 733 amet ipsum. Nunc quis urna dictum turpis accumsan semper.

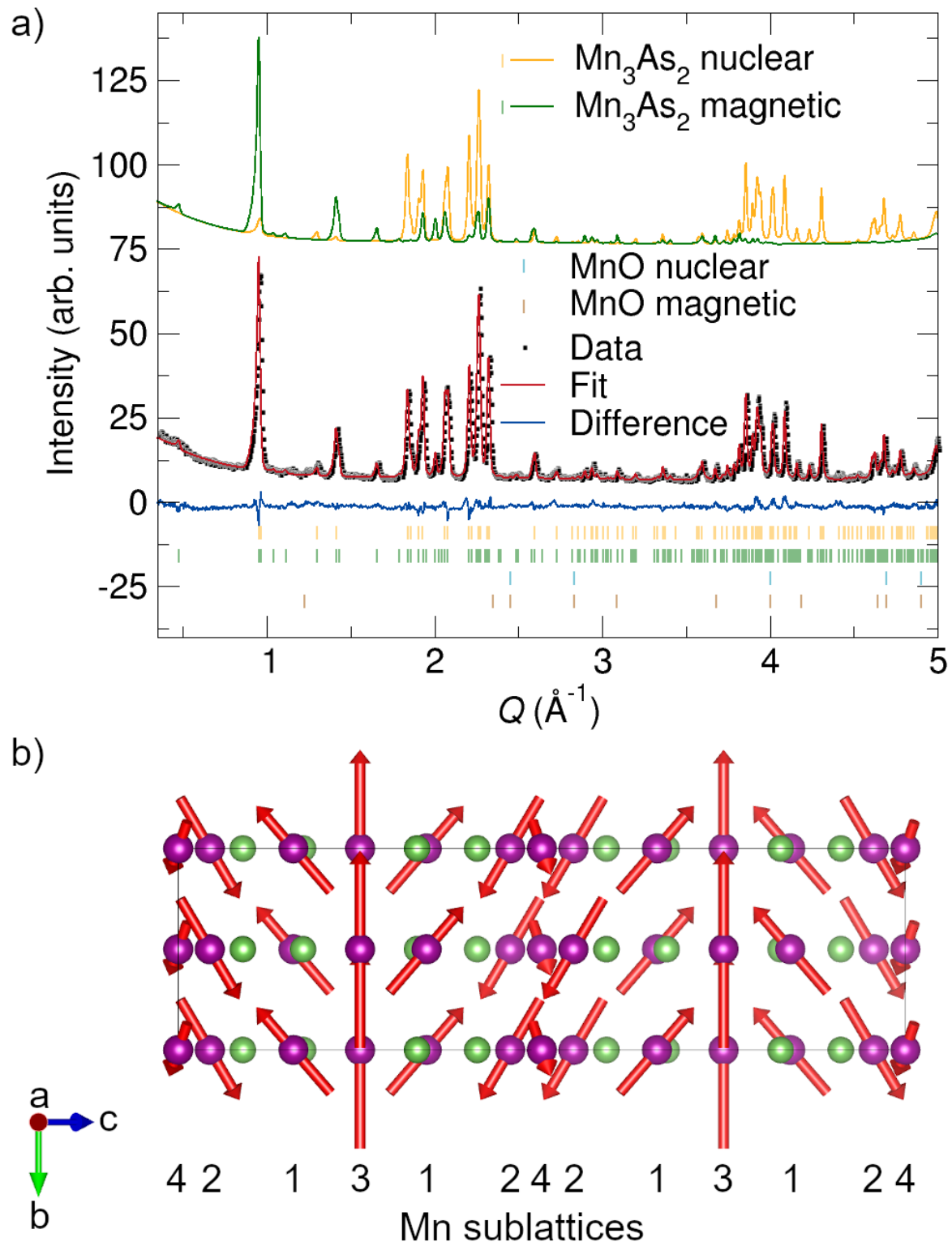


Figure 6.7: Electronic band structure

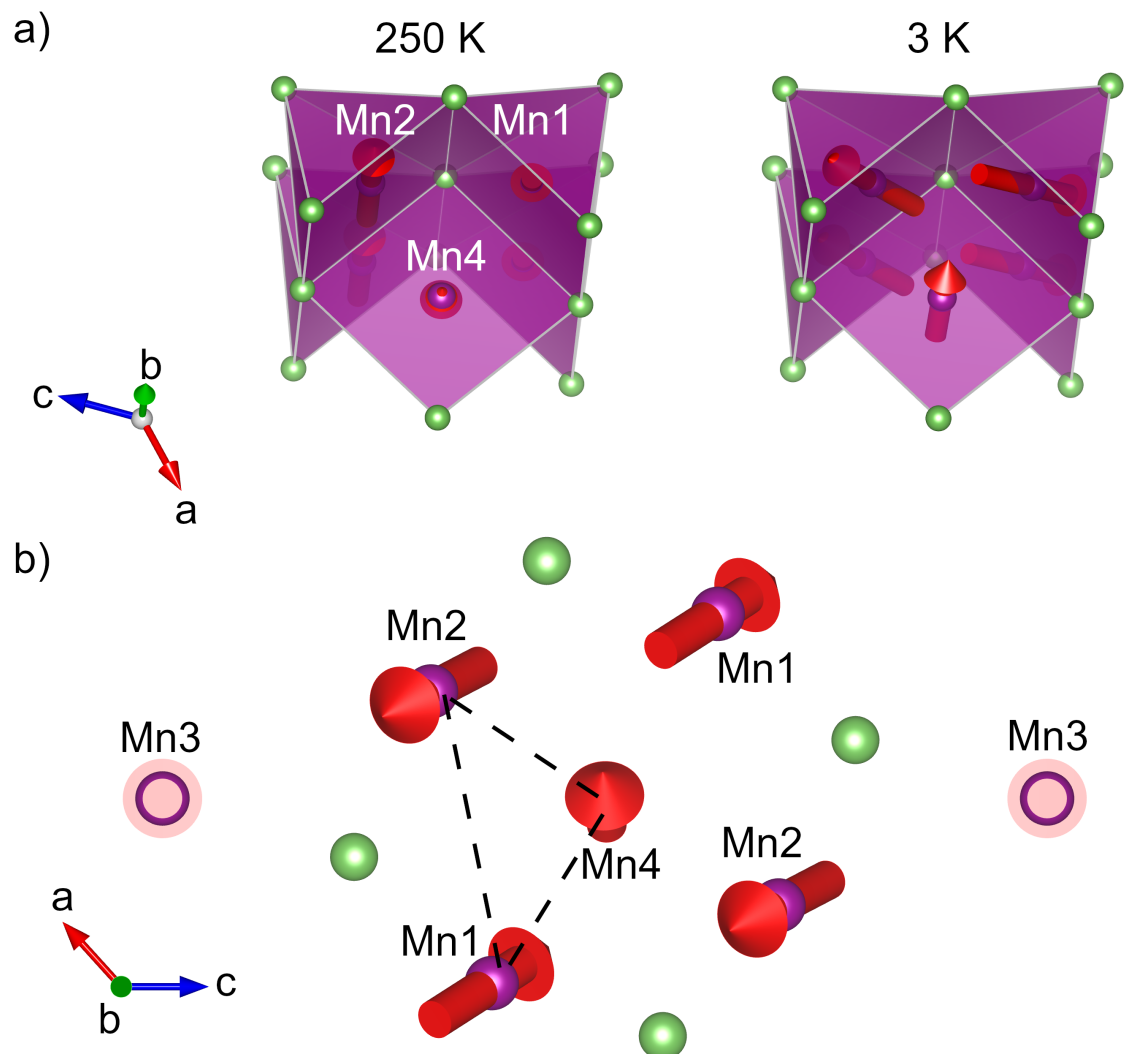


Figure 6.8: Electronic band structure

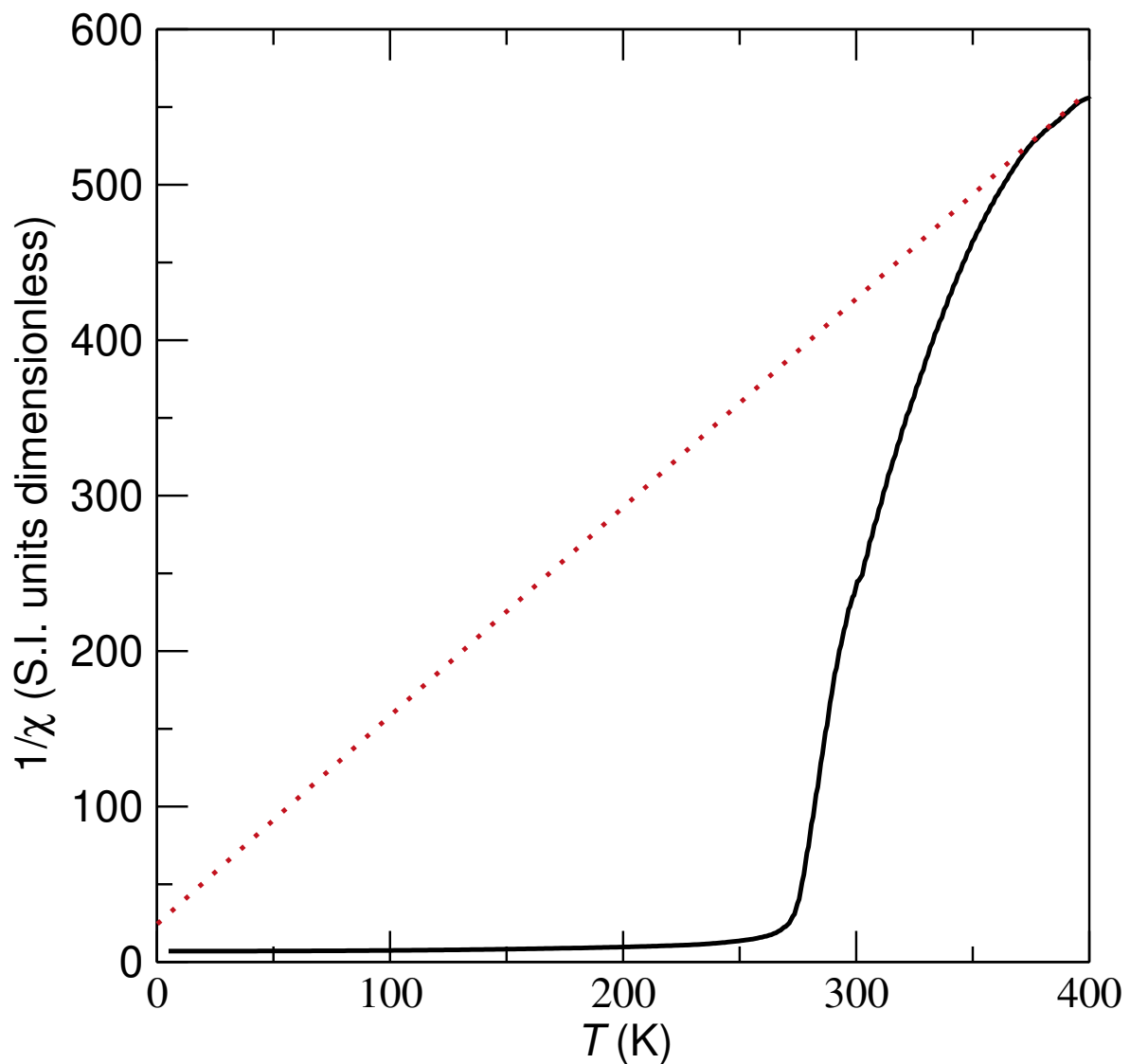


Figure 6.9: Electronic band structure

Chapter 7

Spin canting in tetragonal CuMnAs

734 Lorem ipsum dolor sit amet, consectetur adipiscing elit. Etiam lobortis facilisis sem. Nullam
735 nec mi et neque pharetra sollicitudin. Praesent imperdiet mi nec ante. Donec ullamcorper,
736 felis non sodales commodo, lectus velit ultrices augue, a dignissim nibh lectus placerat pede.

737 Vivamus nunc nunc, molestie ut, ultricies vel, semper in, velit. Ut porttitor. Praesent in sapien.
738 Lorem ipsum dolor sit amet, consectetur adipiscing elit. Duis fringilla tristique neque. Sed
739 interdum libero ut metus. Pellentesque placerat. Nam rutrum augue a leo. Morbi sed elit sit
740 amet ante lobortis sollicitudin. Praesent blandit blandit mauris. Praesent lectus tellus, aliquet
741 aliquam, luctus a, egestas a, turpis. Mauris lacinia lorem sit amet ipsum. Nunc quis urna
742 dictum turpis accumsan semper.

743 Lorem ipsum dolor sit amet, consectetur adipiscing elit. Etiam lobortis facilisis sem.
744 Nullam nec mi et neque pharetra sollicitudin. Praesent imperdiet mi nec ante. Donec
745 ullamcorper, felis non sodales commodo, lectus velit ultrices augue, a dignissim nibh lectus
746 placerat pede. Vivamus nunc nunc, molestie ut, ultricies vel, semper in, velit. Ut porttitor.
747 Praesent in sapien. Lorem ipsum dolor sit amet, consectetur adipiscing elit. Duis fringilla
748 tristique neque. Sed interdum libero ut metus. Pellentesque placerat. Nam rutrum augue
749 a leo. Morbi sed elit sit amet ante lobortis sollicitudin. Praesent blandit blandit mauris.
750 Praesent lectus tellus, aliquet aliquam, luctus a, egestas a, turpis. Mauris lacinia lorem sit
751 amet ipsum. Nunc quis urna dictum turpis accumsan semper.

752 Lorem ipsum dolor sit amet, consectetur adipiscing elit. Etiam lobortis facilisis sem.
753 Nullam nec mi et neque pharetra sollicitudin. Praesent imperdiet mi nec ante. Donec
754 ullamcorper, felis non sodales commodo, lectus velit ultrices augue, a dignissim nibh lectus
755 placerat pede. Vivamus nunc nunc, molestie ut, ultricies vel, semper in, velit. Ut porttitor.
756 Praesent in sapien. Lorem ipsum dolor sit amet, consectetur adipiscing elit. Duis fringilla
757 tristique neque. Sed interdum libero ut metus. Pellentesque placerat. Nam rutrum augue
758 a leo. Morbi sed elit sit amet ante lobortis sollicitudin. Praesent blandit blandit mauris.
759 Praesent lectus tellus, aliquet aliquam, luctus a, egestas a, turpis. Mauris lacinia lorem sit
760 amet ipsum. Nunc quis urna dictum turpis accumsan semper.

761 Lorem ipsum dolor sit amet, consectetur adipiscing elit. Etiam lobortis facilisis sem.
762 Nullam nec mi et neque pharetra sollicitudin. Praesent imperdiet mi nec ante. Donec
763 ullamcorper, felis non sodales commodo, lectus velit ultrices augue, a dignissim nibh lectus

764 placerat pede. Vivamus nunc nunc, molestie ut, ultricies vel, semper in, velit. Ut porttitor.
765 Praesent in sapien. Lorem ipsum dolor sit amet, consectetuer adipiscing elit. Duis fringilla
766 tristique neque. Sed interdum libero ut metus. Pellentesque placerat. Nam rutrum augue
767 a leo. Morbi sed elit sit amet ante lobortis sollicitudin. Praesent blandit blandit mauris.
768 Praesent lectus tellus, aliquet aliquam, luctus a, egestas a, turpis. Mauris lacinia lorem sit
769 amet ipsum. Nunc quis urna dictum turpis accumsan semper.

770 Lorem ipsum dolor sit amet, consectetuer adipiscing elit. Etiam lobortis facilisis sem.
771 Nullam nec mi et neque pharetra sollicitudin. Praesent imperdiet mi nec ante. Donec
772 ullamcorper, felis non sodales commodo, lectus velit ultrices augue, a dignissim nibh lectus
773 placerat pede. Vivamus nunc nunc, molestie ut, ultricies vel, semper in, velit. Ut porttitor.
774 Praesent in sapien. Lorem ipsum dolor sit amet, consectetuer adipiscing elit. Duis fringilla
775 tristique neque. Sed interdum libero ut metus. Pellentesque placerat. Nam rutrum augue
776 a leo. Morbi sed elit sit amet ante lobortis sollicitudin. Praesent blandit blandit mauris.
777 Praesent lectus tellus, aliquet aliquam, luctus a, egestas a, turpis. Mauris lacinia lorem sit
778 amet ipsum. Nunc quis urna dictum turpis accumsan semper.

779 Lorem ipsum dolor sit amet, consectetuer adipiscing elit. Etiam lobortis facilisis sem.
780 Nullam nec mi et neque pharetra sollicitudin. Praesent imperdiet mi nec ante. Donec
781 ullamcorper, felis non sodales commodo, lectus velit ultrices augue, a dignissim nibh lectus
782 placerat pede. Vivamus nunc nunc, molestie ut, ultricies vel, semper in, velit. Ut porttitor.
783 Praesent in sapien. Lorem ipsum dolor sit amet, consectetuer adipiscing elit. Duis fringilla
784 tristique neque. Sed interdum libero ut metus. Pellentesque placerat. Nam rutrum augue
785 a leo. Morbi sed elit sit amet ante lobortis sollicitudin. Praesent blandit blandit mauris.
786 Praesent lectus tellus, aliquet aliquam, luctus a, egestas a, turpis. Mauris lacinia lorem sit
787 amet ipsum. Nunc quis urna dictum turpis accumsan semper.

Chapter 8

Exchange interactions in Fe₂As probed by inelastic neutron scattering

788 Lorem ipsum dolor sit amet, consectetur adipiscing elit. Etiam lobortis facilisis sem. Nullam
789 nec mi et neque pharetra sollicitudin. Praesent imperdiet mi nec ante. Donec ullamcorper,
790 felis non sodales commodo, lectus velit ultrices augue, a dignissim nibh lectus placerat pede.
791 Vivamus nunc nunc, molestie ut, ultricies vel, semper in, velit. Ut porttitor. Praesent in sapien.
792 Lorem ipsum dolor sit amet, consectetur adipiscing elit. Duis fringilla tristique neque. Sed
793 interdum libero ut metus. Pellentesque placerat. Nam rutrum augue a leo. Morbi sed elit sit
794 amet ante lobortis sollicitudin. Praesent blandit blandit mauris. Praesent lectus tellus, aliquet
795 aliquam, luctus a, egestas a, turpis. Mauris lacinia lorem sit amet ipsum. Nunc quis urna
796 dictum turpis accumsan semper.

797 Lorem ipsum dolor sit amet, consectetur adipiscing elit. Etiam lobortis facilisis sem.
798 Nullam nec mi et neque pharetra sollicitudin. Praesent imperdiet mi nec ante. Donec
799 ullamcorper, felis non sodales commodo, lectus velit ultrices augue, a dignissim nibh lectus
800 placerat pede. Vivamus nunc nunc, molestie ut, ultricies vel, semper in, velit. Ut porttitor.
801 Praesent in sapien. Lorem ipsum dolor sit amet, consectetur adipiscing elit. Duis fringilla
802 tristique neque. Sed interdum libero ut metus. Pellentesque placerat. Nam rutrum augue
803 a leo. Morbi sed elit sit amet ante lobortis sollicitudin. Praesent blandit blandit mauris.
804 Praesent lectus tellus, aliquet aliquam, luctus a, egestas a, turpis. Mauris lacinia lorem sit
805 amet ipsum. Nunc quis urna dictum turpis accumsan semper.

806 Lorem ipsum dolor sit amet, consectetur adipiscing elit. Etiam lobortis facilisis sem.
807 Nullam nec mi et neque pharetra sollicitudin. Praesent imperdiet mi nec ante. Donec
808 ullamcorper, felis non sodales commodo, lectus velit ultrices augue, a dignissim nibh lectus
809 placerat pede. Vivamus nunc nunc, molestie ut, ultricies vel, semper in, velit. Ut porttitor.
810 Praesent in sapien. Lorem ipsum dolor sit amet, consectetur adipiscing elit. Duis fringilla
811 tristique neque. Sed interdum libero ut metus. Pellentesque placerat. Nam rutrum augue
812 a leo. Morbi sed elit sit amet ante lobortis sollicitudin. Praesent blandit blandit mauris.
813 Praesent lectus tellus, aliquet aliquam, luctus a, egestas a, turpis. Mauris lacinia lorem sit
814 amet ipsum. Nunc quis urna dictum turpis accumsan semper.

815 Lorem ipsum dolor sit amet, consectetur adipiscing elit. Etiam lobortis facilisis sem.
816 Nullam nec mi et neque pharetra sollicitudin. Praesent imperdiet mi nec ante. Donec
817 ullamcorper, felis non sodales commodo, lectus velit ultrices augue, a dignissim nibh lectus

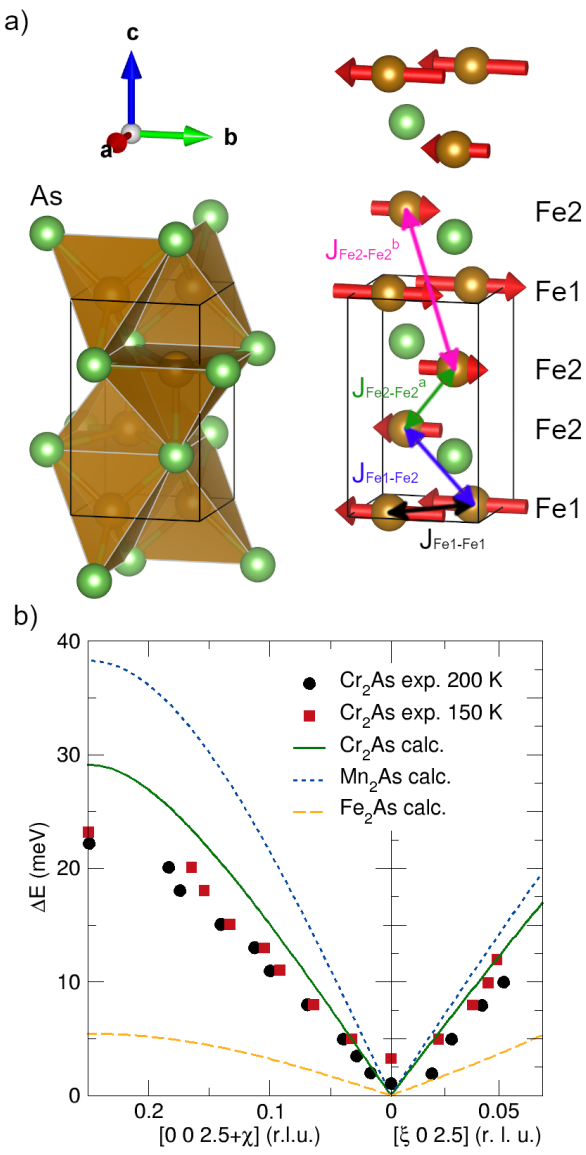


Figure 8.1: Electronic band structure



Figure 8.2: Electronic band structure

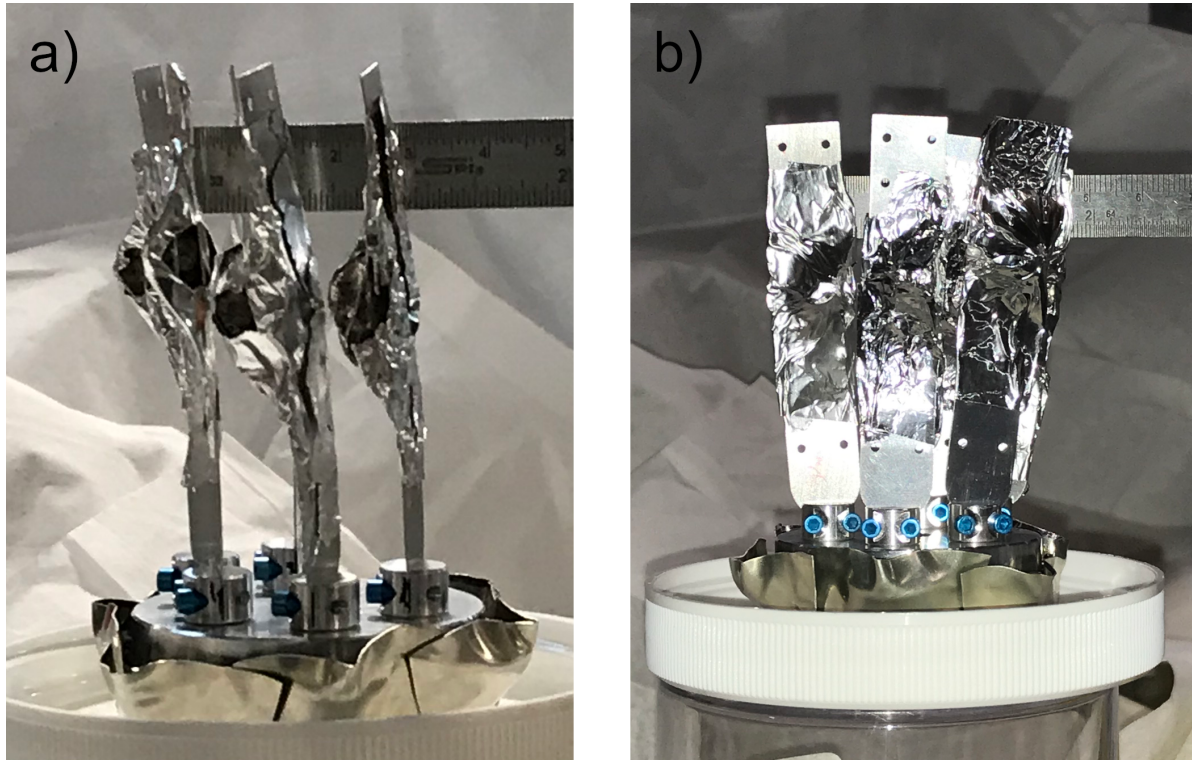


Figure 8.3: Electronic band structure

818 placerat pede. Vivamus nunc nunc, molestie ut, ultricies vel, semper in, velit. Ut porttitor.
819 Praesent in sapien. Lorem ipsum dolor sit amet, consectetuer adipiscing elit. Duis fringilla
820 tristique neque. Sed interdum libero ut metus. Pellentesque placerat. Nam rutrum augue
821 a leo. Morbi sed elit sit amet ante lobortis sollicitudin. Praesent blandit blandit mauris.
822 Praesent lectus tellus, aliquet aliquam, luctus a, egestas a, turpis. Mauris lacinia lorem sit
823 amet ipsum. Nunc quis urna dictum turpis accumsan semper.

824 Lorem ipsum dolor sit amet, consectetuer adipiscing elit. Etiam lobortis facilisis sem.
825 Nullam nec mi et neque pharetra sollicitudin. Praesent imperdiet mi nec ante. Donec
826 ullamcorper, felis non sodales commodo, lectus velit ultrices augue, a dignissim nibh lectus
827 placerat pede. Vivamus nunc nunc, molestie ut, ultricies vel, semper in, velit. Ut porttitor.
828 Praesent in sapien. Lorem ipsum dolor sit amet, consectetuer adipiscing elit. Duis fringilla
829 tristique neque. Sed interdum libero ut metus. Pellentesque placerat. Nam rutrum augue
830 a leo. Morbi sed elit sit amet ante lobortis sollicitudin. Praesent blandit blandit mauris.
831 Praesent lectus tellus, aliquet aliquam, luctus a, egestas a, turpis. Mauris lacinia lorem sit
832 amet ipsum. Nunc quis urna dictum turpis accumsan semper.

833 Lorem ipsum dolor sit amet, consectetuer adipiscing elit. Etiam lobortis facilisis sem.
834 Nullam nec mi et neque pharetra sollicitudin. Praesent imperdiet mi nec ante. Donec
835 ullamcorper, felis non sodales commodo, lectus velit ultrices augue, a dignissim nibh lectus

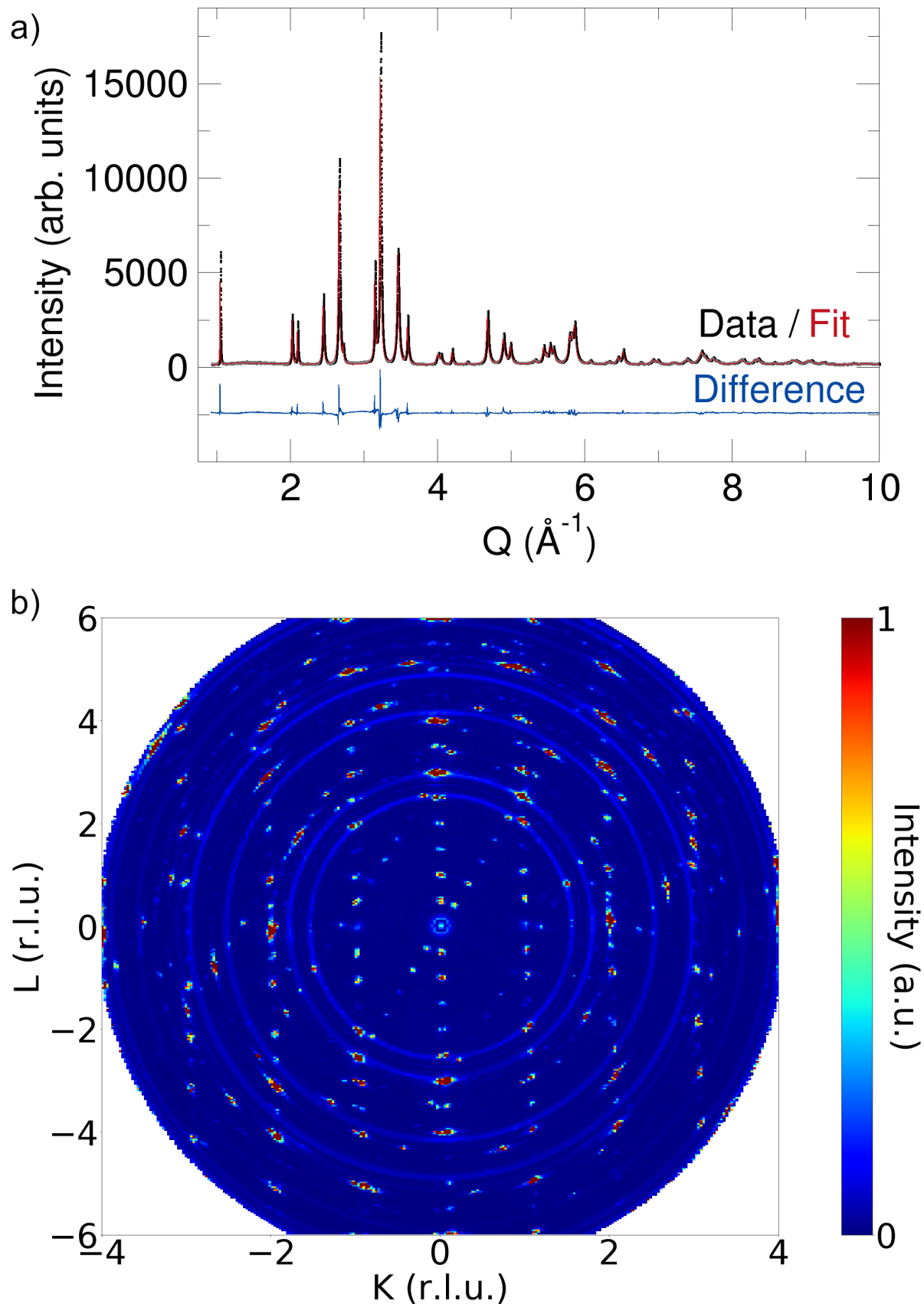


Figure 8.4: Electronic band structure

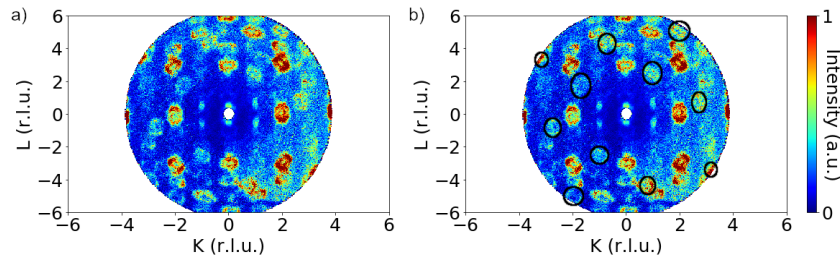


Figure 8.5: Electronic band structure

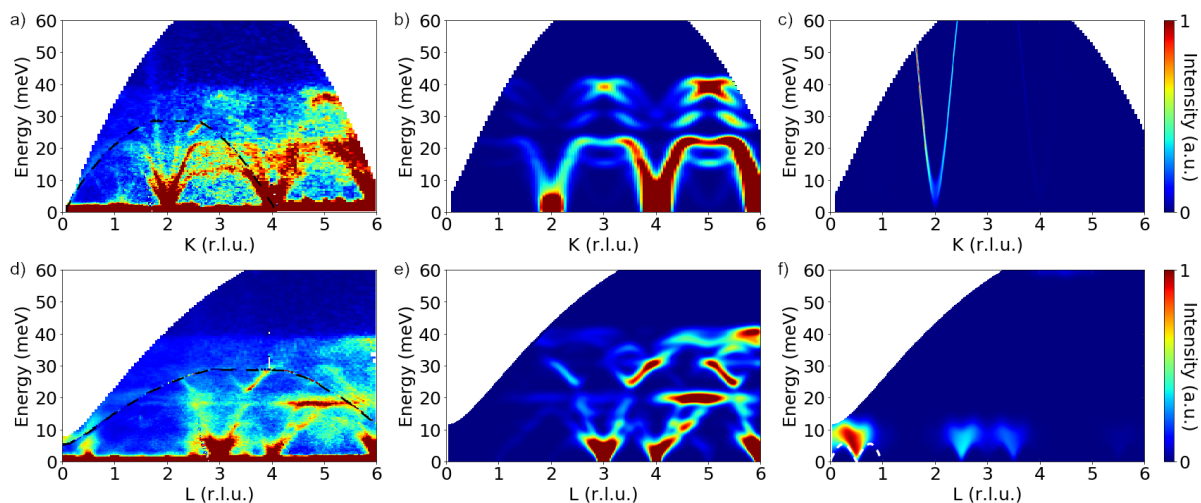


Figure 8.6: Electronic band structure

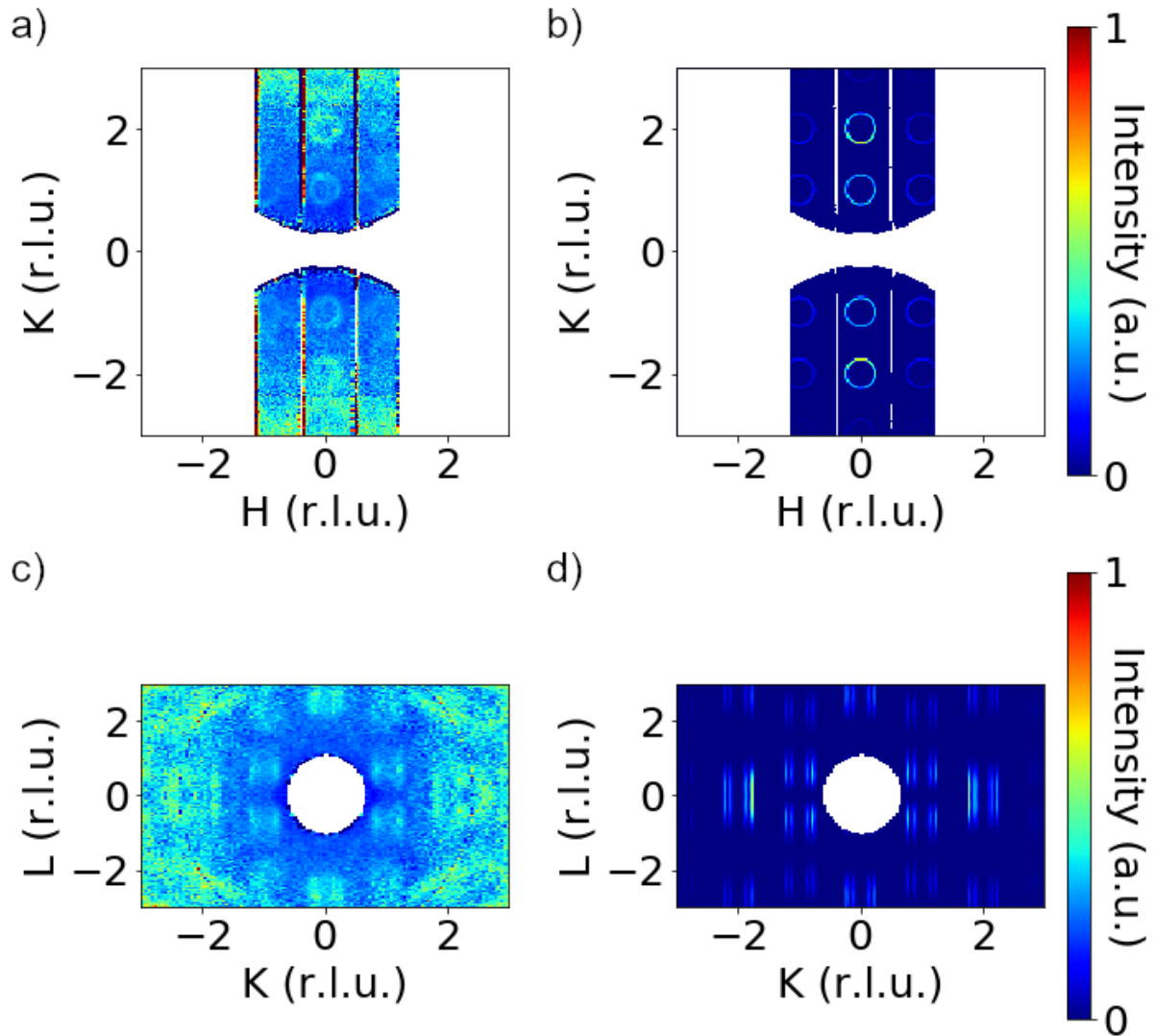


Figure 8.7: Electronic band structure

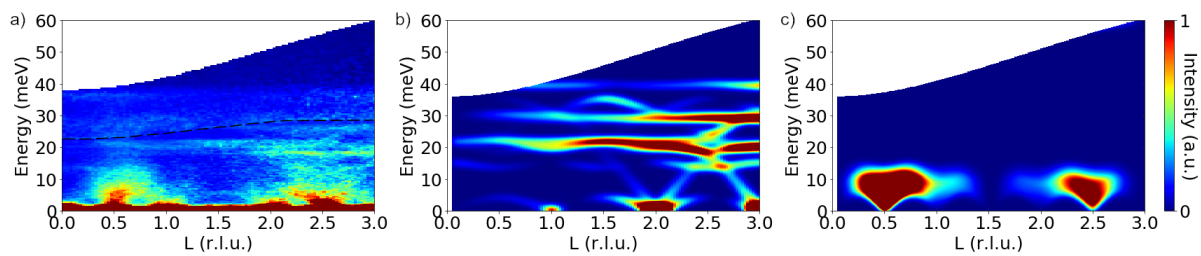


Figure 8.8: Electronic band structure

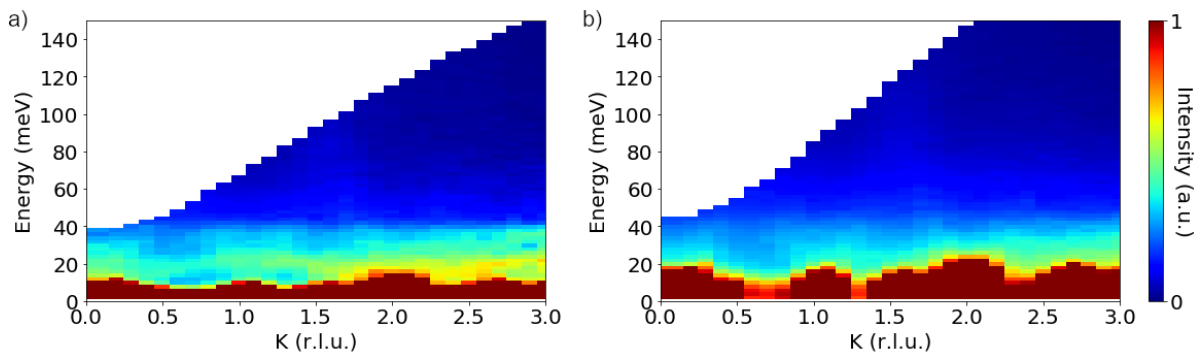


Figure 8.9: Electronic band structure

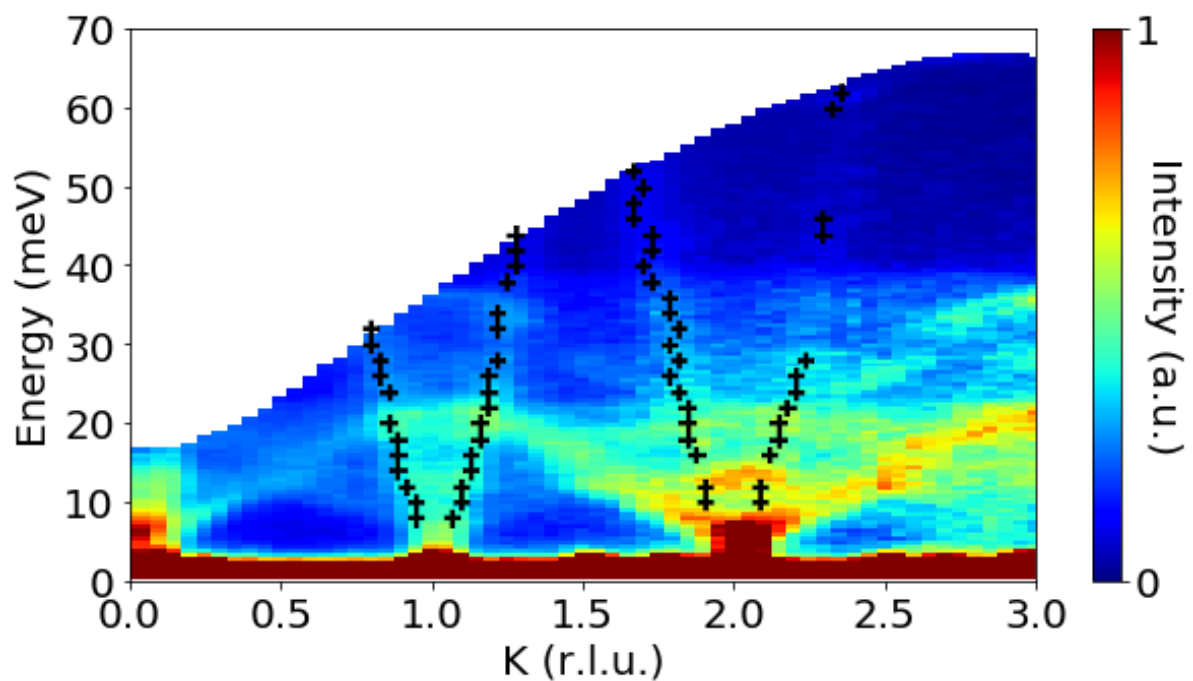


Figure 8.10: Electronic band structure

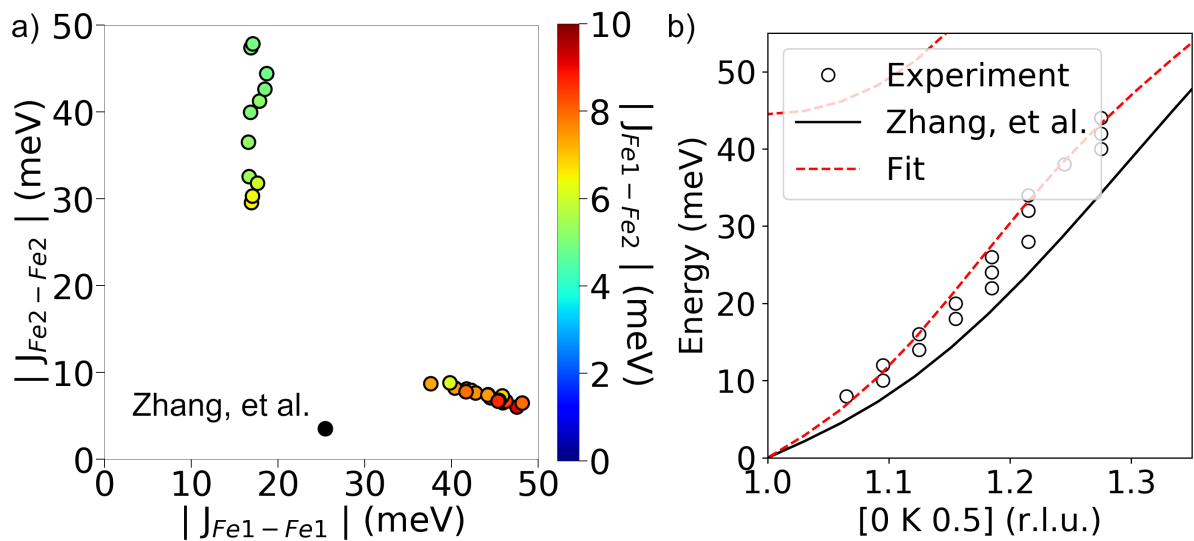


Figure 8.11: Electronic band structure

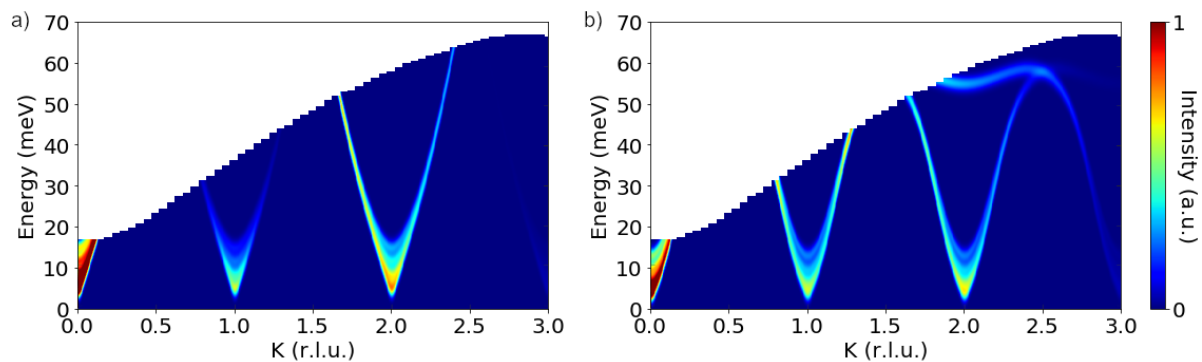


Figure 8.12: Electronic band structure

836 placerat pede. Vivamus nunc nunc, molestie ut, ultricies vel, semper in, velit. Ut porttitor.
837 Praesent in sapien. Lorem ipsum dolor sit amet, consectetuer adipiscing elit. Duis fringilla
838 tristique neque. Sed interdum libero ut metus. Pellentesque placerat. Nam rutrum augue
839 a leo. Morbi sed elit sit amet ante lobortis sollicitudin. Praesent blandit blandit mauris.
840 Praesent lectus tellus, aliquet aliquam, luctus a, egestas a, turpis. Mauris lacinia lorem sit
841 amet ipsum. Nunc quis urna dictum turpis accumsan semper.

Chapter 9

Conclusions

842 Lorem ipsum dolor sit amet, consectetur adipiscing elit. Etiam lobortis facilisis sem. Nullam
843 nec mi et neque pharetra sollicitudin. Praesent imperdiet mi nec ante. Donec ullamcorper,
844 felis non sodales commodo, lectus velit ultrices augue, a dignissim nibh lectus placerat pede.
845 Vivamus nunc nunc, molestie ut, ultricies vel, semper in, velit. Ut porttitor. Praesent in sapien.

846 Lorem ipsum dolor sit amet, consectetur adipiscing elit. Duis fringilla tristique neque. Sed
847 interdum libero ut metus. Pellentesque placerat. Nam rutrum augue a leo. Morbi sed elit sit
848 amet ante lobortis sollicitudin. Praesent blandit blandit mauris. Praesent lectus tellus, aliquet
849 aliquam, luctus a, egestas a, turpis. Mauris lacinia lorem sit amet ipsum. Nunc quis urna
850 dictum turpis accumsan semper.

851 Lorem ipsum dolor sit amet, consectetur adipiscing elit. Etiam lobortis facilisis sem.
852 Nullam nec mi et neque pharetra sollicitudin. Praesent imperdiet mi nec ante. Donec
853 ullamcorper, felis non sodales commodo, lectus velit ultrices augue, a dignissim nibh lectus
854 placerat pede. Vivamus nunc nunc, molestie ut, ultricies vel, semper in, velit. Ut porttitor.
855 Praesent in sapien. Lorem ipsum dolor sit amet, consectetur adipiscing elit. Duis fringilla
856 tristique neque. Sed interdum libero ut metus. Pellentesque placerat. Nam rutrum augue
857 a leo. Morbi sed elit sit amet ante lobortis sollicitudin. Praesent blandit blandit mauris.
858 Praesent lectus tellus, aliquet aliquam, luctus a, egestas a, turpis. Mauris lacinia lorem sit
859 amet ipsum. Nunc quis urna dictum turpis accumsan semper.

860 Lorem ipsum dolor sit amet, consectetur adipiscing elit. Etiam lobortis facilisis sem.
861 Nullam nec mi et neque pharetra sollicitudin. Praesent imperdiet mi nec ante. Donec
862 ullamcorper, felis non sodales commodo, lectus velit ultrices augue, a dignissim nibh lectus
863 placerat pede. Vivamus nunc nunc, molestie ut, ultricies vel, semper in, velit. Ut porttitor.
864 Praesent in sapien. Lorem ipsum dolor sit amet, consectetur adipiscing elit. Duis fringilla
865 tristique neque. Sed interdum libero ut metus. Pellentesque placerat. Nam rutrum augue
866 a leo. Morbi sed elit sit amet ante lobortis sollicitudin. Praesent blandit blandit mauris.
867 Praesent lectus tellus, aliquet aliquam, luctus a, egestas a, turpis. Mauris lacinia lorem sit
868 amet ipsum. Nunc quis urna dictum turpis accumsan semper.

869 Lorem ipsum dolor sit amet, consectetur adipiscing elit. Etiam lobortis facilisis sem.
870 Nullam nec mi et neque pharetra sollicitudin. Praesent imperdiet mi nec ante. Donec
871 ullamcorper, felis non sodales commodo, lectus velit ultrices augue, a dignissim nibh lectus

872 placerat pede. Vivamus nunc nunc, molestie ut, ultricies vel, semper in, velit. Ut porttitor.
873 Praesent in sapien. Lorem ipsum dolor sit amet, consectetuer adipiscing elit. Duis fringilla
874 tristique neque. Sed interdum libero ut metus. Pellentesque placerat. Nam rutrum augue
875 a leo. Morbi sed elit sit amet ante lobortis sollicitudin. Praesent blandit blandit mauris.
876 Praesent lectus tellus, aliquet aliquam, luctus a, egestas a, turpis. Mauris lacinia lorem sit
877 amet ipsum. Nunc quis urna dictum turpis accumsan semper.

878 Lorem ipsum dolor sit amet, consectetuer adipiscing elit. Etiam lobortis facilisis sem.
879 Nullam nec mi et neque pharetra sollicitudin. Praesent imperdiet mi nec ante. Donec
880 ullamcorper, felis non sodales commodo, lectus velit ultrices augue, a dignissim nibh lectus
881 placerat pede. Vivamus nunc nunc, molestie ut, ultricies vel, semper in, velit. Ut porttitor.
882 Praesent in sapien. Lorem ipsum dolor sit amet, consectetuer adipiscing elit. Duis fringilla
883 tristique neque. Sed interdum libero ut metus. Pellentesque placerat. Nam rutrum augue
884 a leo. Morbi sed elit sit amet ante lobortis sollicitudin. Praesent blandit blandit mauris.
885 Praesent lectus tellus, aliquet aliquam, luctus a, egestas a, turpis. Mauris lacinia lorem sit
886 amet ipsum. Nunc quis urna dictum turpis accumsan semper.

887 Lorem ipsum dolor sit amet, consectetuer adipiscing elit. Etiam lobortis facilisis sem.
888 Nullam nec mi et neque pharetra sollicitudin. Praesent imperdiet mi nec ante. Donec
889 ullamcorper, felis non sodales commodo, lectus velit ultrices augue, a dignissim nibh lectus
890 placerat pede. Vivamus nunc nunc, molestie ut, ultricies vel, semper in, velit. Ut porttitor.
891 Praesent in sapien. Lorem ipsum dolor sit amet, consectetuer adipiscing elit. Duis fringilla
892 tristique neque. Sed interdum libero ut metus. Pellentesque placerat. Nam rutrum augue
893 a leo. Morbi sed elit sit amet ante lobortis sollicitudin. Praesent blandit blandit mauris.
894 Praesent lectus tellus, aliquet aliquam, luctus a, egestas a, turpis. Mauris lacinia lorem sit
895 amet ipsum. Nunc quis urna dictum turpis accumsan semper.

References

- [1] X. Zhang, Q. Liu, J.-W. Luo, A. J. Freeman, and A. Zunger, "Hidden spin polarization in inversion-symmetric bulk crystals," *Nature Physics*, vol. 10, pp. 387–393, 2014.
- [2] W. Toy and B. Zee, *Computer Hardware/Software Architecture*, vol. First Edit. 1986.
- [3] J. S. Meena, S. M. Sze, U. Chand, and T. Y. Tseng, "Overview of emerging nonvolatile memory technologies," *Nanoscale Research Letters*, vol. 9, pp. 1–33, 2014.
- [4] K. M. Krishnan, *Fundamentals and Applications of Magnetic Materials*, vol. First Edit. 2016.
- [5] P. Wadley, B. Howells, J. Zelezny, C. Andrews, V. Hills, R. P. Campion, V. Novak, K. Olejnik, F. Maccherozzi, S. S. Dhesi, S. Y. Martin, T. Wagner, J. Wunderlich, F. Freimuth, Y. Mokrousov, J. Kunes, J. S. Chauhan, M. J. Grzybowski, A. W. Rushforth, K. W. Edmonds, B. L. Gallagher, and T. Jungwirth, "Electrical switching of an antiferromagnet," *Science*, vol. 351, pp. 587–591, 2016.
- [6] C. Chappert, A. Fert, and F. N. Van Dau, "The emergence of spin electronics in data storage," *Nature Materials*, vol. 6, pp. 813–823, 2007.
- [7] S. Bhatti, R. Sbiaa, A. Hirohata, H. Ohno, S. Fukami, and S. N. Piramanayagam, "Spintronics based random access memory: a review," *Materials Today*, vol. 20, pp. 530–548, 2017.
- [8] H. V. Gomonay and V. M. Loktev, "Spin transfer and current-induced switching in antiferromagnets," *Physical Review B - Condensed Matter and Materials Physics*, vol. 81, p. 144427, 2010.
- [9] S. A. Siddiqui, J. Sklenar, K. Kang, M. J. Gilbert, A. Schleife, N. Mason, and A. Hoffmann, "Metallic antiferromagnets," *Journal of Applied Physics*, vol. 128, p. 040904, 2020.
- [10] A. Manchon and S. Zhang, "Theory of nonequilibrium intrinsic spin torque in a single nanomagnet," *Physical Review B - Condensed Matter and Materials Physics*, vol. 78, p. 212405, 2008.
- [11] J. Železný, H. Gao, K. Výborný, J. Zemen, J. Mašek, A. Manchon, J. Wunderlich, J. Sinova, and T. Jungwirth, "Relativistic néel-order fields induced by electrical current in antiferromagnets," *Physical Review Letters*, vol. 113, no. 15, pp. 1–5, 2014.
- [12] J. Železný, H. Gao, A. Manchon, F. Freimuth, Y. Mokrousov, J. Zemen, J. Mašek, J. Sinova, and T. Jungwirth, "Spin-orbit torques in locally and globally noncentrosymmetric crystals: Antiferromagnets and ferromagnets," *Physical Review B*, vol. 95, p. 014403, 2017.

- [13] M. Meinert, D. Graulich, and T. Matalla-wagner, "Electrical Switching of Antiferromagnetic Mn₂Au and the Role of Thermal Activation," *Physical Review Applied*, vol. 9, p. 64040, 2018.
- [14] T. Matalla-Wagner, M. F. Rath, D. Graulich, J. M. Schmalhorst, G. Reiss, and M. Meinert, "Electrical Neél-Order Switching in Magnetron-Sputtered CuMnAs Thin Films," *Physical Review Applied*, vol. 12, p. 064003, 2019.
- [15] Y. Kim, K. Kang, A. Schleife, and M. J. Gilbert, "Voltage-induced switching of an antiferromagnetically ordered topological Dirac semimetal," *Physical Review B*, vol. 97, p. 134415, 2018.
- [16] A. N. Nateprov, V. C. Kravtsov, V. Fritsch, and H. von Löhneysen, "Structure and properties of the tetragonal phase of MnCuAs," *Surface Engineering and Applied Electrochemistry*, vol. 47, pp. 540–543, 2011.
- [17] F. MáčA, J. Mašek, O. Stelmakhovych, X. Martí, H. Reichlová, K. Uhlířová, P. Beran, P. Wadley, V. Novák, and T. Jungwirth, "Room-temperature antiferromagnetism in CuMnAs," *Journal of Magnetism and Magnetic Materials*, vol. 324, pp. 1606–1612, 2012.
- [18] P. Wadley, V. Novák, R. P. Campion, C. Rinaldi, X. Martí, H. Reichlová, J. Zelezný, J. Gazquez, M. A. Roldan, M. Varela, D. Khalyavin, S. Langridge, D. Kriegner, F. Máca, J. Masek, R. Bertacco, V. Holy, A. W. Rushforth, K. W. Edmonds, B. L. Gallagher, C. T. Foxon, J. Wunderlich, and T. Jungwirth, "Tetragonal phase of epitaxial room-temperature antiferromagnet CuMnAs," *Nature Communications*, vol. 4, p. 2322, 2013.
- [19] K. Uhlirova, R. Tarasenko, F. J. Martinez-Casado, B. Vondrackova, and Z. Matej, "Synthesis and single crystal study of CuMn₃As₂ and Cu₂Mn₄As₃," *Journal of Alloys and Compounds*, vol. 650, pp. 224–227, 2015.
- [20] V. Hills, P. Wadley, R. P. Campion, V. Novak, R. Beardsley, K. W. Edmonds, B. L. Gallagher, B. Ouladdiaf, and T. Jungwirth, "Paramagnetic to antiferromagnetic transition in epitaxial tetragonal CuMnAs (invited)," *Journal of Applied Physics*, vol. 117, p. 172608, 2015.
- [21] P. Wadley, V. Hills, M. R. Shahedkhah, K. W. Edmonds, R. P. Campion, V. Novák, B. Ouladdiaf, D. Khalyavin, S. Langridge, V. Saidl, P. Nemec, A. W. Rushforth, B. L. Gallagher, S. S. Dhesi, F. MacCherozzi, J. Železný, and T. Jungwirth, "Antiferromagnetic structure in tetragonal CuMnAs thin films," *Scientific Reports*, vol. 5, p. 17079, 2015.
- [22] A. E. Austin, E. Adelson, and W. H. Cloud, "Magnetic Structures of Mn₂As and Mn₂Sb_{0.7}As_{0.3}," *Journal of Applied Physics*, vol. 33, pp. 1356–1357, 1962.
- [23] G. E. Bacon and R. Street, "Magnetic Structure of Manganse Arsenide," *Nature*, vol. 175, p. 518, 1955.
- [24] "Magnetic ordering and metal-atom site preference in tetragonal CrMnAs: Electronic correlation effects," *Journal of Computational Chemistry*, vol. 39, pp. 1585–1593, 2018.
- [25] Y. Zhang, J. Brgoch, and G. J. Miller, "Magnetic ordering in tetragonal 3d metal arsenides M₂As (M = Cr, Mn, Fe): An ab initio investigation," *Inorganic Chemistry*, vol. 52, pp. 3013–3021, 2013.

- [26] Y. Zhang and G. J. Miller, "Competition between direct and indirect exchange couplings in MnFeAs: A first-principles investigation," *Journal of Physical Chemistry C*, vol. 119, pp. 580–589, 2015.
- [27] S. Y. Bodnar, M. Filianina, S. P. Bommanaboyena, T. Forrest, F. Maccherozzi, A. A. Sapozhnik, Y. Skourski, M. Kläui, and M. Jourdan, "Imaging of current induced Néel vector switching in antiferromagnetic Mn₂Au," *Physical Review B*, vol. 99, pp. 8–12, 2019.
- [28] M. A. Susner, D. S. Parker, and A. S. Sefat, "Importance of doping and frustration in itinerant Fe-doped Cr₂Al," *Journal of Magnetism and Magnetic Materials*, vol. 392, pp. 68–73, 2015.
- [29] M. Atoji, "Antiferromagnetic structure of AlCr₂," *The Journal of Chemical Physics*, vol. 43, pp. 222–225, 1965.
- [30] A. Kallel and F. D. Bergevin, "ANTIFERROMAGNETISME DE LA SOLUTION SOLIDE DE L'ALUMINTUM DANS LE CHROME," *Solid State Communications*, vol. 5, pp. 955–958, 1967.
- [31] G. Venturini, R. Welter, and B. Malaman, "Crystallographic data and magnetic properties of RT₆Ge₆ compounds (R Sc, Y, Nd, Sm, GdLu; TMn, Fe)," *Journal of Alloys and Compounds*, vol. 185, pp. 99–107, 1992.
- [32] T. Mazet, O. Isnard, and B. Malaman, "Neutron diffraction and ⁵⁷Fe Mössbauer study of the HfFe₆Ge₆-type RFe₆Ge₆ compounds (R = Sc , Ti , Zr , Hf , Nb)," *Solid State Communications*, vol. 114, pp. 91–96, 2000.
- [33] S. Nakatsuji, N. Kiyohara, and T. Higo, "Large anomalous Hall effect in a non-collinear antiferromagnet at room temperature," *Nature*, vol. 527, pp. 212–215, 2015.
- [34] J. Kübler and C. Felser, "Non-collinear antiferromagnets and the anomalous Hall effect," *Epl*, vol. 108, p. 67001, 2014.
- [35] M. Kimata, H. Chen, K. Kondou, S. Sugimoto, P. K. Muduli, M. Ikhlas, Y. Omori, T. Tomita, A. H. MacDonald, S. Nakatsuji, and Y. Otani, "Magnetic and magnetic inverse spin Hall effects in a non-collinear antiferromagnet," *Nature*, vol. 565, pp. 627–630, 2019.
- [36] U. Häussermann, M. Boström, P. Viklund, R. Ö, and T. Björnängen, "FeGa₃ and RuGa₃: Semiconducting intermetallic compounds," *Journal of Solid State Chemistry*, vol. 165, pp. 94–99, 2002.
- [37] P. Viklund, S. Lidin, P. Berastegui, and U. Häussermann, "Variations of the FeGa₃ structure type in the systems CoIn_{3-x}Zn_x and CoGa_{3-x}ZN_x," *Journal of Solid State Chemistry*, vol. 165, pp. 100–110, 2002.
- [38] Y. Zhang, C. Michioka, M. Imai, H. Ueda, and K. Yoshimura, "Effect of Co substitution on the magnetic properties in Fe_{1-x}CoxGa₃," *Journal of Physics: Conference Series*, vol. 868, p. 012025, 2017.
- [39] D. Harker, "The crystal structure of Ni₄Mo," *The Journal of Chemical Physics*, vol. 12, pp. 315–317, 1944.

- [40] A. Taylor and N. J. Doyle, "Further studies on the nickel–aluminium system. I. β -NiAl and δ -Ni₂Al₃ phase fields," *Journal of Applied Crystallography*, vol. 5, pp. 201–209, 1972.
- [41] M. Yuzuri and M. Yamada, "On the Magnetic Properties of the Compound Mn₂As," *Journal of the Physical Society of Japan*, vol. 15, pp. 1845–1850, 1960.
- [42] K. Uhlirova, E. Duverger-Nedellec, R. H. Colman, J. Volny, B. Vondrackova, and K. Carva, "The stability and physical properties of the tetragonal phase of bulk CuMnAs antiferromagnet," *Journal of Alloys and Compounds*, vol. 771, pp. 680–685, 2019.
- [43] A. A. Coelho, "TOPAS and TOPAS-Academic: an optimization program integrating computer algebra and crystallographic objects written in C++," *Journal of Applied Crystallography*, vol. 51, pp. 210–218, 2018.
- [44] B. H. Toby and R. B. Von Dreele, "GSAS-II: the genesis of a modern open-source all purpose crystallography software package," *Journal of Applied Crystallography*, vol. 46, pp. 544–549, 2013.
- [45] M. J. Grzybowski, P. Wadley, K. W. Edmonds, R. Beardsley, V. Hills, R. P. Campion, B. L. Gallagher, J. S. Chauhan, V. Novak, T. Jungwirth, F. Maccherozzi, and S. S. Dhesi, "Imaging Current-Induced Switching of Antiferromagnetic Domains in CuMnAs," *Physical Review Letters*, vol. 118, p. 057701, 2017.
- [46] P. Wadley, S. Reimers, M. J. Grzybowski, C. Andrews, M. Wang, J. S. Chauhan, B. L. Gallagher, R. P. Campion, K. W. Edmonds, S. S. Dhesi, F. Maccherozzi, V. Novak, J. Wunderlich, and T. Jungwirth, "Current polarity-dependent manipulation of antiferromagnetic domains," *Nature Nanotechnology*, vol. 13, pp. 362–365, 2018.
- [47] P. Tang, Q. Zhou, G. Xu, and S. C. Zhang, "Dirac fermions in an antiferromagnetic semimetal," *Nature Physics*, vol. 12, pp. 1100–1104, 2016.
- [48] E. Emmanouilidou, H. Cao, P. Tang, X. Gui, C. Hu, B. Shen, J. Wu, S.-C. Zhang, W. Xie, and N. Ni, "Magnetic order induces symmetry breaking in the single-crystalline orthorhombic CuMnAs semimetal," *Phys. Rev. B*, vol. 96, p. 224405, Dec. 2017.
- [49] L. Pytlak and A. Zięba, "Magnetic phase diagram of MnAs," *J. Magn. Magn. Mater.*, vol. 51, pp. 199–210, Aug. 1985.
- [50] L. H. Schwartz, E. L. Hall, and G. P. Felcher, "Magnetic Structure of MnAs and MnAs_{0.92}P_{0.08}," *J. Appl. Phys.*, vol. 42, pp. 1621–1622, Mar. 1971.
- [51] V. P. Glazkov, D. P. Kozlenko, K. M. Podurets, B. N. Savenko, and V. A. Somenkov, "Neutron diffraction investigation of the atomic and magnetic structures of MnAs at high pressures," *Crystallogr. Rep.*, vol. 48, no. 1, pp. 59–62, 2003.
- [52] L. H. Dietrich, W. Jeitschko, and M. H. Möller, "The crystal structure of Mn₃As₂(I)," *Z. Kristallogr. Cryst. Mater.*, vol. 190, p. 259, Jan. 1990.
- [53] M. H. Möller and W. Jeitschko, "The crystal structures of Mn₃As₂(II) and Mn₅As₄ determined from intergrown crystals," *Z. Kristallogr. Cryst. Mater.*, vol. 204, p. 1, Jan. 1993.

- [54] M. F. Hagedorn and W. Jeitschko, "The Crystal Structure of Mn₃As₂(III)," *J. Solid State Chem.*, vol. 113, pp. 257–260, Dec. 1994.
- [55] M. F. Hagedorn and W. Jeitschko, "Synthesis and crystal structure of Mn₄As₃ and its relation to other manganese arsenides," *J. Solid State Chem.*, vol. 119, pp. 344–348, Nov. 1995.
- [56] H. Nowotny, R. Funk, and J. Pesl, "Kristallchemische Untersuchungen in den Systemen Mn?As, V?Sb, Ti?Sb," *Monatsh. Chem.*, vol. 82, no. 3, pp. 513–525, 1951.
- [57] A. E. Austin, E. Adelson, and W. H. Cloud, "Magnetic Structures of Mn₂As and Mn₂Sb_{0.7}As_{0.3}," *J. Appl. Phys.*, vol. 33, pp. 1356–1357, Mar. 1962.
- [58] J. Wang, B. H. Toby, P. L. Lee, L. Ribaud, S. M. Antao, C. Kurtz, M. Ramanathan, R. B. Von Dreele, and M. A. Beno, "A dedicated powder diffraction beamline at the Advanced Photon Source: Commissioning and early operational results," *Rev. Sci. Instrum.*, vol. 79, p. 085105, Aug. 2008.
- [59] M. D. Frontzek, R. Whitfield, K. M. Andrews, A. B. Jones, M. Bobrek, K. Vodopivec, B. C. Chakoumakos, and J. A. Fernandez-Baca *Rev. Sci. Instrum.*, vol. 89, p. 0928011, 2018.
- [60] J. Perez-Mato, S. Gallego, E. Tasçi, L. Elcoro, G. de la Flor, and M. Aroyo, "Symmetry-Based Computational Tools for Magnetic Crystallography," *Ann. Rev. Mater. Res.*, vol. 45, no. 1, pp. 217–248, 2015.
- [61] J. Rodríguez-Carvajal, "Recent advances in magnetic structure determination by neutron powder diffraction," *Physica B*, vol. 192, pp. 55–69, Oct. 1993.
- [62] G. Kresse and J. Furthmüller, "Efficient iterative schemes for ab initio total-energy calculations using a plane-wave basis set," *Phys. Rev. B*, vol. 54, no. 16, p. 11169, 1996.
- [63] G. Kresse and D. Joubert, "From ultrasoft pseudopotentials to the projector augmented-wave method," *Phys. Rev. B*, vol. 59, pp. 1758–1775, 1999.
- [64] P. E. Blöchl, "Projector augmented-wave method," *Phys. Rev. B*, vol. 50, p. 17953, 1994.
- [65] J. P. Perdew, K. Burke, and M. Ernzerhof, "Generalized gradient approximation made simple," *Phys. Rev. Lett.*, vol. 77, p. 3865, 1996.
- [66] H. J. Monkhorst and J. D. Pack, "Special points for brillouin-zone integrations," *Phys. Rev. B*, vol. 13, p. 5188, 1976.
- [67] S. Steiner, S. Khmelevskyi, M. Marsmann, and G. Kresse, "Calculation of the magnetic anisotropy with projected-augmented-wave methodology and the case study of disordered fe_{1-x}co_x alloys," *Phys. Rev. B*, vol. 93, p. 224425, 2016.
- [68] V. F. Sears, "Neutron scattering lengths and cross sections," *Neutron News*, vol. 3, pp. 26–37, Jan. 1992.
- [69] T. Nozue, H. Kobayashi, M. Sato, A. Uesawa, T. Suzuki, and T. Kamimura, "Specific heat and de Haas-van Alphen effect in NiAs," *Physica B*, vol. 237-238, pp. 174–176, July 1997.

- [70] Z. M. Stadnik, P. Wang, N. Jansen, D. Walcher, P. Gütlich, and T. Kanomata, "Magnetization and ^{61}Ni Mössbauer effect study of the ternary arsenide CrNiAs," *J. Phys. Cond. Mat.*, vol. 20, p. 325230, Aug. 2008.
- [71] P. J. Brown, V. Nunez, F. Tasset, J. B. Forsyth, and P. Radhakrishna, "Determination of the magnetic structure of Mn₃Sn using generalized neutron polarization analysis," *J. Phys.: Condens. Matter*, vol. 2, pp. 9409–9422, 1990.
- [72] B. Y. Kotyuzhanskii and D. V. Nikiforov, "Static magnetic properties of the quasi-one-dimensional hexagonal antiferromagnet CsMnBr₃," *J. Phys.: Condens. matter*, vol. 3, no. 385, 1991.
- [73] K. Hirakawa, H. Ikeda, H. Kadokami, and K. Ubukoshi, "Magnetic susceptibilities of the Frustrated Triangular Lattice Antiferromagnets CsVCl₃ and VX₂ (X=Cl, Br and I): Appearance of Magnetic Liquid in the Ordered State," *J. Phys. Soc. Jpn.*, vol. 52, no. 8, pp. 2882–2887, 1983.
- [74] T. F. Duan, W. J. Ren, W. L. Liu, S. J. Li, W. Liu, and Z. D. Zhang, "Magnetic anisotropy of single-crystalline Mn₃Sn in triangular and helix-phase states," *Appl. Phys. Lett.*, vol. 107, no. 082403, 2015.
- [75] L. J. Pauwels, G. Maervoet, and R. Vervaeke, "Electrical Resistivity and Magnetic Susceptibility Measurements on Copper Arsenides," *Z. Anorg. Allg. Chem.*, vol. 397, pp. 307–313, Apr. 1973.
- [76] E. V. Sampathkumaran, K. Sengupta, S. Rayaprol, K. K. Iyer, T. Doert, and J. P. F. Jemetio, "Enhanced Electrical Resistivity before Néel Order in the Metals R Cu As 2 (R = S m , Gd, Tb, and Dy)," *Phys. Rev. Lett.*, vol. 91, p. 036603, July 2003.
- [77] K. Sengupta, P. L. Paulose, E. V. Sampathkumaran, T. Doert, and J. P. F. Jemetio, "Magnetic behavior of Eu Cu 2 As 2 : A delicate balance between antiferromagnetic and ferromagnetic order," *Phys. Rev. B*, vol. 72, p. 184424, Nov. 2005.
- [78] H. Katsuraki and N. Achiwa, "The Magnetic Structure of Fe₂as," *J. Phys. Soc. Japan*, vol. 21, pp. 2238–2243, Nov. 1966.
- [79] P. W. Chapman, O. N. Tufte, J. D. Zook, and D. Long, "Electrical properties of heavily doped silicon," *J. Appl. Phys.*, vol. 34, no. 11, pp. 3291–3295, 1963.
- [80] N. Takeshita, I. Akira, S. Ishida, H. Eisaki, and Y. Yoshida, "Electrical resistivity of FeAs , FeAs 2 and Fe 2 As at homogeneous high pressures," *J. Phys.: Conf. Ser.*, vol. 950, no. 042024, p. 042024, 2017.
- [81] L. C. Lutz, *Electronic structure, magnetic structure, and metal-atom site preferences in CrMnAs*. Graduate theses and dissertations, Iowa State University, 2013.
- [82] F. Máca, J. Kudrnovský, V. Drchal, K. Carva, P. Baláž, and I. Turek, "Physical properties of the tetragonal CuMnAs: A first-principles study," *Phys. Rev. B*, vol. 96, p. 094406, Sept. 2017.

- [83] K. Yang, K. Kang, Z. Diao, A. Ramanathan, M. H. Karigerasi, D. P. Shoemaker, A. Schleife, and D. G. Cahill, "Magneto-optic Response of the Metallic Antiferromagnet Fe₂As to Ultrafast Temperature Excursions," *arXiv*, pp. 1–30, 2019.
- [84] K. Elk, J. Richter, and V. Christoph, "Density of states and electrical conductivity of disordered alloys with strong electron correlation," *J. Phys. F*, vol. 9, no. 2, pp. 307–316, 1979.
- [85] J. H. Mooij, "Electrical conduction in concentrated disordered transition metal alloys," *Phys. Status Solidi A*, vol. 17, no. 2, pp. 521–530, 1973.